Transformation of the pair correlation function of galaxies near a caustic

Yu. N. Eroshenko and M. I. Zel'nikov

P. M. Lebedev Physics Institute, Russian Academy of Sciences, 117924 Moscow, Russia

The effect of large-scale caustics in nondissipative dark matter on the pair correlation function of galaxies is investigated. It is shown that if the initial correlation function of the galaxies is of a power-law form, then the presence of caustics in the observation region does not change the form of the function but only decreases its amplitude. © *1997 American Institute of Physics.* [S0021-3640(97)00108-4]

PACS numbers: 98.65.−r

Together with a large number of works concerning linear and weakly nonlinear[1–5] effects in the formation of the large-scale structure of the universe, there are some recent papers devoted to a theoretical investigation of the formation of objects in the strongly nonlinear region.[6] A characteristic feature of this region is the appearance of multistream flows (in the Lagrangian terminology — crossings of the trajectories of individual particles). In Ref. 6 a method of adiabatic capture was developed to investigate strong nonlinearities in the limit of an infinite number of streams. The asymptotic correlation functions in the limit of large correlations were obtained using this method. It was found that the initial correlations are unimportant for correlations in a region with a sufficiently large number of streams. This letter studies the fate of the initial correlations in a region with a small number of streams.

In a hierarchical picture, the short-wavelength fluctuations, which lead to the formation of galaxies, are the first to arrive at the nonlinear stage, while large-scale fluctuations (clusters and superclusters of galaxies) reach the nonlinear stage only at later times. The correlations of the galaxies correspond to the correlations of the high density peaks from which the galaxies formed,[7] and they are determined mainly by the spectrum of galactic-scale perturbations. According to observations, the total mass of the dark matter in clusters and superclusters of galaxies is several times (up to an order of magnitude) greater than the mass of the dark matter in galaxies.[8] Therefore, the dynamics of the development of inhomogeneities is determined not only by the distribution of the galaxies themselves but also, and predominantly, by the distribution of the intergalactic dark matter. For this reason, galaxies can be treated as test particles following the general motion of the matter. After a definite period of time has passed following the formation of the galaxies, large-scale fluctuations reach the nonlinear stage, and multistream flows arise in them as well. On account of a redistribution of the galaxies in space the development of large-scale inhomogeneities leads to a change in the correlations of the galaxies. Therefore, the final correlation properties of the distribution of the galaxies are affected by perturbations not only on the galactic scale but also on large scales.

The density distribution near a caustic separating a region with different numbers of streams has the following characteristic form (on one side of the caustic):

$$\rho = C(\Delta x)^{-1/2}, \tag{1}$$

where Δx is the distance from the caustic in a direction along the normal and $C =$ const. From the observational standpoint, it is easiest to observe the caustic which formed first and which separates the one- and three-stream regions. We shall term such caustics primary. Thus, this letter examines the transformation of the correlation function of galaxies in the regions near caustics where three-stream flows have formed but before flows with a large number of streams have formed there.

For a sufficiently large region of observation the correlation function can be approximated, to a good degree of accuracy, by an average over an ensemble of galaxies. At the same time, large-scale inhomogeneities which are comparable in size to the regions of observation cannot be regarded as a random function but must be treated as a specified external field.

TRANSFORMATION OF THE CORRELATION FUNCTION

Let $\bar{q}$ represent comoving coordinates of some specific galaxy in the epoch of galaxy formation t_1 and let $\bar{x}$ be the coordinates of this galaxy at the time of observation $t_2 > t_1$. We denote the transformation function as $\bar{f}(\bar{q})$: $\bar{x} = \bar{f}(\bar{q})$. This function, which depends on the specific form of the large-scale inhomogeneity in the observation region, specifies the character of the redistribution of the galaxies in the multistream region. The multistream nature is manifested in multivaluedness of the inverse function to $\bar{f}(\bar{q})$. The density $n'(\bar{x})$ of galaxies at time t_2 is related with the density $n(\bar{q})$ of galaxies at time t_1 by the relation

$$n'(\bar{x}) = \int d^3 q\, n(\bar{q})\, \delta^{(3)}(\bar{x} - \bar{f}(\bar{q})),$$

where $\delta^{(3)}$ is the Dirac delta function. We shall examine at the time t_2 a region of space Ω with volume V. To calculate the observed correlation function $\xi'(r)$ we shall perform three averagings:

a) spatial averaging over the region Ω neglecting boundary effects;

b) average with respect to the directions of the vector $\bar{k} = \bar{r}/r$; and,

c) averaging over an ensemble of galaxies at time t_1.

After performing the averages a)–c) we obtain

$$n'^2[1 + \xi'(r)] = \frac{1}{4\pi V} \int_{|\bar{k}|=1} d^2 k \int_\Omega d^3 x \langle n'(\bar{x}) n'(\bar{x} + \bar{r}) \rangle$$

$$= \frac{1}{4\pi V} \int d^3 q \int d^3 \gamma\, n^2 [1 + \xi(r|\bar{\gamma})] \delta(|\bar{f}(\bar{q}) - \bar{f}(\bar{q} + r\bar{\gamma})|/r - 1), \tag{2}$$

where n' is the average density of galaxies in the region Ω, n is the average density of galaxies in the image of the region Ω under the transformation $\bar{f}(\bar{q})$, and the first
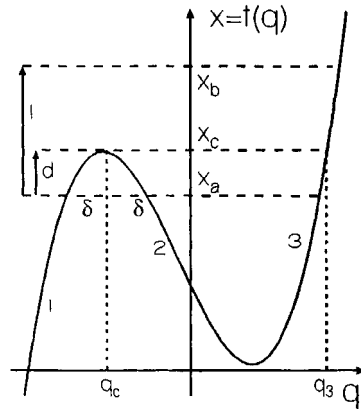
FIG. 1.

integration extends over values of $\bar{q}$ such that $\bar{f}(\bar{q}) \in \Omega$. Here $\xi(r)$ and $\xi'(r)$ are the correlation functions of the galaxies at times t_1 and t_2, respectively, $\langle n(\bar{q})n(\bar{q}')\rangle = n^2[1+\xi(|\bar{q}-\bar{q}'|)]$.

Let us consider the particular case when the transformation $\bar{f}(\bar{q})$ is nearly one-dimensional in the region Ω, i.e., $\bar{f}(\bar{q})$ changes very little in two of three directions. This happens if the observation region is much smaller than the radius of curvature of the caustic. In this case the caustic can be regarded as being approximately flat. Let the distinguished direction of the normal to the caustic coincide with the direction q_1 and let the transformation in this direction be given by the function $f(q_1)$. Then

$$\bar{f}(\bar{q}) = (f(q_1); q_2; q_3).$$

Next, let Ω be a curvilinear cylinder whose generatrix is directed along the x_1 axis and is of length l. Let $q \equiv q_1$ and $\gamma \equiv \gamma_1$, and let $[l]$ be the segment on the x_1 axis that represents the projection of Ω on the x_1 axis. Under these assumptions, formula (2) assumes the form

$$1 + \xi'(r) = \frac{n^2}{2ln'^2} \int_{f(q)\in[l]} dq \int_{|f(q)-f(q+r\gamma)|<r} d\gamma$$
$$\times [1+\xi(r\sqrt{\gamma^2+1-[f(q)-f(q+r\gamma)]^2/r^2})]. \tag{3}$$

The regions of integration are indicated under the integrals. Let us call the integral of 1 in Eq. (3) the ''induced correlations'' and the integral of ξ the ''transformed correlations'' of the galaxies.

Let the region Ω lie near the caustic, as shown in Fig. 1. The segment $[l]=[x_a; x_b]$, x_c is the coordinate of the caustic, and $x_a < x_c < x_b$. The point x_c corresponds to the point q_c in the merging streams 1 and 2 and the point q_3 in the stream 3: $x_c = f(q_c) = f(q_3)$. We expand the function $f(q)$ in a series about the point q_c (we mark the quantities evaluated at the point q_c with a subscript c):

$$f(q) = x_c + \frac{1}{2} f''_c (q - q_c)^2 + \frac{1}{6} f'''_c (q - q_c)^3 + \cdots . \tag{4}$$

Here we have taken into account the fact that $f'_c = 0$. Let x_a be chosen such that expansion (4) to quadratic terms is valid in the region from x_a to x_c. This assumption is valid if

$$\left| \frac{f'''_c \delta}{3 f''_c} \right| \ll 1, \tag{5}$$

where δ is found from the condition $d = \frac{1}{2} f''_c \delta^2$ and $d \equiv x_c - x_a$. For $f''_c \neq 0$ there always exist values of d which are so small that the condition (5) holds. Let $L \equiv -2/f''_c$ and $L > 0$. In the region $[x_a; x_b]$ there also exists a third stream flowing toward the streams forming the caustic. In contrast to the streams 1 and 2, the characteristics of the stream 3 on the segment $[x_a; x_b]$ change very little if l is sufficiently small. We approximate the transformation in the third stream by a linear function $f(q) = x_c + \psi(q - q_3)$, where $\psi = \text{const}$. We shall now calculate the induced correlations on the basis of our formalism. We shall have in mind values of r which are small enough that

$$4rL \ll \delta^2, \text{ that is, } r \ll d.$$

We also make the natural assumption that

$$\frac{\delta}{L} \ll \psi \lesssim 1. \tag{6}$$

Physically, the condition (6) means that the matter in the caustic is compressed much more strongly than in the third stream and also that the matter in the entire observation region Ω has been compressed in comparison with the state at the time t_1.

A calculation of the induced correlations gives a logarithmic dependence, similar to that obtained previously in Ref. 9.

We shall now calculate the transformed correlations under the assumption that the initial correlations of the galaxies have a power-law form $\xi(r) = \alpha r^{-\beta}$, where β is close to the observed value of 1.8. The transformed correlations give the following contribution in Eq. (3):

$$\frac{\alpha}{r^\beta} \frac{n^2}{2 l n'^2} \int_{f(q) \in [l]} dq \int_{|f(q) - f(q + r\gamma)| < r} d\gamma \left[\gamma^2 + 1 - \frac{[f(q) - f(q + r\gamma)]^2}{r^2} \right]^{-\beta/2}.$$

Performing the calculations on the basis of the assumptions made, we obtain

$$\frac{\alpha}{r^\beta} \frac{n^2}{n'^2} \left\{ \frac{\sqrt{\pi} \delta}{l} \frac{\Gamma\left(\frac{\beta - 1}{2}\right)}{\Gamma(\beta/2)} + \frac{1}{\psi^2} F\left(\frac{\beta}{2}; \frac{1}{2}; \frac{3}{2}; 1 - \psi^{-2}\right) \right\},$$

where Γ is the gamma function and F is the Gauss hypergeometric function, with the asymptotic forms

$$\psi^{-2}F\left(\frac{\beta}{2};\frac{1}{2};\frac{3}{2};1-\psi^{-2}\right)=\begin{cases}1 & \text{for } 1-\psi\ll1;\\[2ex]\dfrac{1}{\psi}\dfrac{\sqrt{\pi}}{2}\dfrac{\Gamma\left(\dfrac{\beta-1}{2}\right)}{\Gamma(\beta/2)} & \text{for } \psi\ll1.\end{cases}$$

The ratio n^2/n'^2 can be expressed in terms of the ratio of the volumes of the observation region and its image. The final expression for the new correlation function can be written as

$$1+\xi'(r)=\left(\frac{2\delta}{l}+\frac{1}{\psi}\right)^{-2}\Bigg\{4Ll^{-1}\ln(d/r)$$
$$+\psi^{-2}+\alpha r^{-\beta}\left(\sqrt{\pi}\delta l^{-1}\frac{\Gamma\left(\dfrac{\beta-1}{2}\right)}{\Gamma(\beta/2)}+\psi^{-2}F\left(\frac{\beta}{2};\frac{1}{2};\frac{3}{2};1-\psi^{-2}\right)\right)\Bigg\}.$$
(7)

In the calculations it was found that the terms corresponding to the correlations of galaxies from the caustic and from the stream *3* can be neglected in comparison with the correlations written out above.

It is important to note that under the assumptions made, the power-law form of the correlations holds for arbitrary $\beta>1$, and a change in β results only in a change in their amplitudes. If there are no caustics in the observation region, then Eq. (7) assumes the form

$$1+\xi'(r)=1+\xi(r)F\left(\frac{\beta}{2};\frac{1}{2};\frac{3}{2};1-\psi^{-2}\right).$$

Therefore, a uniform one-dimensional compression only decreases the amplitude of the power-law correlation function.

All quantities appearing in Eq. (7) can be expressed in terms of observable characteristics. For example, the quantities l and d are specified parameters of the observation region. To within ''basing'' effects, the quantity ψ is the ratio of the density n_3 of galaxies in the third stream in front of the caustic to the density of galaxies in the field, and $\alpha r^{-\beta}$ is the correlation function of the galaxies in the field. If the law (1) is observed in the distribution of the galaxies, then the quantity L can be expressed in terms of C according to the formula $L=4C^2/\rho_0^2$, where ρ_0 is the present-day cosmological density and $\delta=\sqrt{Ld}$ by definition. Therefore the result (7) contains no model parameters and it can be compared directly with observations.

The combinations of the parameters appearing in Eq. (7) can also be expressed in terms of n, n', and $n_3=\psi n$ as follows: $4L/l=(l/d)((n'-n_3)^2/n^2)$, $2\delta/l=(n'-n_3)/n$.

According to several observations, a plateau or even a local minimum is indeed observed in the radial profile of the density at distances of 1.2–2 Mpc from the centers of

many galactic clusters.[10,11] These features, however, cannot be attributed to primary caustics, since distances of 1.2–2 Mpc correspond to dense virialized regions. To observe a primary caustic it would be desirable to perform a similar investigation of the density distribution at large distances from the centers of clusters. Since the primary caustic is gravitationally coupled with the cluster, there exists a maximum cluster–caustic distance, and this distance does not exceed the initial size R of the inhomogeneity from which the cluster formed. The quantity R can be estimated as follows: $R \lesssim (M/\rho_0)^{1/3} \sim 10$ Mpc, where $M \sim 10^{14} M_\odot$ is the typical mass of a galactic cluster.

Another method for observing caustics, besides looking for behavior (1), is to investigate the correlation functions. In Ref. 9 it was pointed out that induced correlations have a logarithmic singularity, and the character of the singularity in the behavior of a three-point correlation function was found. According to expression (7), not only the induced but also the transformed correlations contribute to $\xi(r)$, and in the limit $r \to 0$ the power-law divergence in the latter correlations is stronger than the divergence of $\ln(d/r)$. This raises the question: Under what conditions can a logarithmic contribution be observed against the background of power-law correlations? Let us examine the most favorable case when $l \sim d$. Then, in view of Eq. (6), the contribution of the third stream in the function (7) can be neglected. The relative magnitude of the logarithmic term at some r and for $\beta \approx 1.8$ is

$$\frac{4L}{\pi\delta} \frac{\ln(d/r)}{\xi(r)}. \tag{8}$$

The quantity L/δ characterizes the clumping of galaxies at distances d from caustics as compared with the density of the galaxies in the field (if ''basing'' effects are neglected). In a review of APM galaxies[12] it was found that $\xi(r) \lesssim 100$ for $r \gtrsim 500$ Mpc. Therefore, even for $L/\delta \sim 10$ the relative contribution of the logarithmic term (8) is greater than 0.1. The value $L/\delta \sim 10$ corresponds to the distant periphery of a cluster, since the average clumping of galaxies in a cluster is ~ 200, while at the centers of clusters this quantity reaches 10^4–10^5 (Ref. 13).

Further support for the existence of caustics would be the discovery of a relative motion of streams of galaxies of different morphological types. The point is that the streams of galaxies forming a caustic have first passed through the dense central regions of a cluster. Since the galaxies are subjected to tidal forces in a rapidly varying gravitational potential, their morphological type could have changed (for example, a galaxy can be converted from a spiral into an irregular or even elliptical galaxy) or the character of their activity could have changed. At the same time, the third stream moving toward the caustic should consist of unperturbed, predominantly spiral galaxies.

[1] R. Juszkiewicz and F. R. Bouchet, in *Proceedings of the 30th Moriond Meeting ''Clustering in the Universe''*, Les Arcs, 1995; e-print: astro-ph/9602134.
[2] C. Porciani, e-print: astro-ph/9609029.
[3] A. N. Taylor and A. J. S. Hamilton, MNRAS **282**, 767 (1996).
[4] C. S. Frenk *et al.*, Astrophys. J. **327**, 507 (1988).
[5] B. Jain, H. Mo, and S. D. M. White, MNRAS **276**, L25 (1995).

[6] A. V. Gurevich and K. P. Zybin, Usp. Fiz. Nauk **165**, 723 (1995).

[7] J. M. Bardeen *et al.*, Astrophys. J. **304**, 15 (1986).

[8] A. V. Dolgov, *Invisible Matter* (to be published in Surveys of High Energy Physics); e-print: astro-ph/9509057.

[9] A. V. Gurevich, M. I. Zelnikov, and K. P. Zybin, in *Proceedings of the 2nd International Sakharov Conference on Physics*, May 20–24, 1996, World Scientific (in press).

[10] A. Oemler, Jr., Astrophys. J. **194**, 1 (1974).

[11] A. S. Sharaov, Astron. Zh. **36**, 807 (1959).

[12] Neta A. Bahcall, e-print: astro-ph/9611148.

[13] C. M. Baugh, e-print: astro-ph/9512011.

Translated by M. E. Alferieff

Exact renormalization group and running Newtonian coupling in higher-derivative gravity

A. A. Bytsenko[a)]
State Technical University, 195252 St. Petersburg, Russia

L. N. Granda[b)]
Departamento de Fisica, Universidad del Valle, A.A. 25360, Cali, Colombia

S. D. Odintsov[c)]
Departamento de Fisica, Universidad del Valle, A.A. 25360, Cali, Colombia; Tomsk Pedagogical University, 634041 Tomsk, Russia

We discuss exact renormalization group (RG) in R^2 gravity using the effective average action formalism. The truncated evolution equation for such a theory against the de Sitter background leads to a system of nonperturbative RG equations for cosmological and gravitational coupling constants. An approximate solution of these RG equations shows that antiscreening or screening behavior of the Newtonian coupling arises, depending on the higher-derivative coupling constants. © *1997 American Institute of Physics.* [S0021-3640(97)00208-9]

PACS numbers: 04.20.−q

In the absence of a consistent theory of quantum gravity it may be that consideration of effective models for quantum gravity (QG) is the only possibility for taking gravitational phenomena into account in high-energy physics. One may start from a particular model of QG (see Ref. 1 for a review) and formulate an effective model which describes the theory in some region. In such a way, an effective theory of the conformal factor for describing QG in the far infrared (at large distances) has been formulated.[2] That theory, which is based on a higher-derivative scalar, provides a way of estimating the behavior of the Newtonian coupling.[3]

One may consider Einstein gravity as an effective theory and estimate the quantum corrections to the Newtonian coupling[4] using the effective-field-theory technique. Moreover, as non-renormalizability is not a problem in such an approach, one can apply the exact RG,[5] say, in the form of an effective average action, in order to formulate the nonperturbative RG equations for the coupling constants in Eistein gravity.[6,7] In the same way it is very interesting to consider R^2 gravity as an effective model. Such models attract a lot of attention (see Ref. 1 for a review and list of references), being multiplicatively renormalizable (but eventually non-unitary in a perturbative approach). Note that the perturbative RG equations for higher-derivative gravity were first considered in Ref. 8 (see Ref. 1 for an introduction). A kind of effective R^2 gravity leads to a more or less successful inflationary Universe.[9]

In the present letter we formulate the evolution equation and nonperturbative RG equations for the coupling constants in R^2 gravity.[1] The action initially is given by the following (in Euclidean notation):

$$S = \int d^4 x \sqrt{g} \left\{ \epsilon R^* R^* + \frac{1}{2f^2} C_{\mu\nu\alpha\beta} C^{\mu\nu\alpha\beta} - \frac{1}{6\nu^2} R^2 - 2\kappa^2 R + 4\kappa^2 \Lambda \right\} , \qquad (1)$$

where $R^* R^* = 1/4 \epsilon^{\mu\nu\alpha\beta} \epsilon_{\lambda\rho\gamma\delta} R^{\lambda\rho}_{\mu\nu} R^{\gamma\delta}_{\alpha\beta}$, $C_{\mu\nu\alpha\beta}$ is the Weyl tensor, $\kappa^{-2} = 32\pi\overline{G}$ is the Newton constant, and ϵ, f^2, ν^2 are gravitational coupling constants. It is well known that the theory with action (1) is multiplicatively renormalizable and asymptotically free. Note that a perturbative running of the Newtonian coupling constant in a theory (1) with matter has been discussed in Ref. 10.

Following the approach of Ref. 6, we will write the evolution equation for the effective average action $\Gamma_k[g,\overline{g}]$ defined at a nonzero momentum ultraviolet scale k below some cutoff Λ_{cutoff}. The truncated form of this evolution equation is

$$\partial_t \Gamma_k[g,\overline{g}] = \frac{1}{2} \text{Tr} \left[(\Gamma_k^{(2)}[g,\overline{g}] + R_k^{\text{grav}}[\overline{g}])^{-1} \partial_t R_k^{\text{grav}}[\overline{g}] \right]$$

$$- \sum_i c_i \text{Tr} \left[(-M_i[g,\overline{g}] + R_{ki}^{gh}[\overline{g}]) \partial_t R_{ki}^{gh}[\overline{g}] \right], \qquad (2)$$

here $t = \ln k$, R_k are cutoffs in the gravitational and ghosts sectors, c_i are the weights for ghosts (we have a Fadeev–Popov ghost with $c_{FP} = 1$ and a so-called third ghost with weight $c_{TG} = 1/2$), $g_{\mu\nu} = \overline{g}_{\mu\nu} + h_{\mu\nu}$, where $h_{\mu\nu}$ is the quantum gravitational field, $\Gamma_k^{(2)}$ is the Hessian of $\Gamma_k[g,\overline{g}]$ with respect to $g_{\mu\nu}$ at fixed $\overline{g}_{\mu\nu}$, and M_i are ghost operators. Note that the right-hand side of Eq. (2) is very similar to the one-loop effective action.

At the next step we have to specify the truncated evolution equation for the theory (1). Starting from the UV scale Λ_{cutoff} and evolving the theory down to smaller scales $k \ll \Lambda_{\text{cutoff}}$, we may use a truncation of the form

$$\kappa^2 \to Z_{Nk}^{-1} \kappa^2, \quad \frac{1}{f^2} \to Z_{Nk} \frac{1}{f^2}, \quad \frac{1}{\nu^2} \to Z_{Nk} \frac{1}{\nu^2}, \quad \Lambda \to \lambda_k , \qquad (3)$$

where k dependence is denoted by a subscript k. We will restrict consideration here to only the lower-derivative terms in the reduction of Γ_k, i.e., the higher-derivative coupling constants may be regarded as free parameters.

Choosing $\overline{g}_{\mu\nu} = g_{\mu\nu}$ (in which case the ghost term disappears) and projecting the evolution equation on the space with low-derivative terms, one gets the left-hand side of the evolution equation (2) as follows:

$$\partial_t \Gamma_k[g,g] = 2\kappa^2 \int d^4 x \sqrt{g} [-R(g) \partial_t Z_{Nk} + 2 \partial_t (Z_{Nk} \lambda_k)] . \qquad (4)$$

The initial conditions for Z_{Nk}, λ_k are chosen as in Ref. 6.

The right-hand sides of the evolution equations may be found after very tedious calculations (choosing the de Sitter background $R_{\mu\nu} = 1/4 g_{\mu\nu} R$, calculating the path in-

tegral, and making an expansion on R). We drop the details of these calculations. The final system of nonperturbative renormalization group (RG) equations for the Newtonian and cosmological constants is obtained as follows:

$$\partial_t g_k = [2 + \eta_N(k)] g_k \,, \tag{5}$$

where g_k is the dimensionless renormalized Newtonian constant,

$$g_k = k^2 G_k = k^2 Z_{Nk}^{-1} \overline{G} \,.$$

The anomalous dimension $\eta_N(k)$ is given by

$$\eta_N(k) = g_k B_1(\alpha_{2k}, \beta_{2k}, \gamma_{2k}, \delta_{2k}) + \eta_N(k) g_k B_2(\alpha_{2k}, \beta_{2k}, \gamma_{2k}, \delta_{2k}) \,, \tag{6}$$

where

$$
\begin{aligned}
B_1(\alpha_{2k}, \beta_{2k}, \gamma_{2k}, \delta_{2k}) = \frac{1}{12\pi} \Bigg\{ & 10\Phi_1^1(\alpha_{2k}) + 10\Phi_1^1(\beta_{2k}) - 10\Phi_1^1(0) + 2\Phi_1^1(\gamma_{2k}) \\
& + 2\Phi_1^1(\delta_{2k}) - (60\alpha_1 + 5)\Phi_2^2(\alpha_{2k}) - (60\beta_1 + 5)\Phi_2^2(\beta_{2k}) \\
& + \left(\frac{24}{K-3} - 6 \right) \Phi_2^2(0) - 12\gamma_1 \Phi_2^2(\gamma_{2k}) - 12\delta_1 \Phi_2^2(\delta_{2k}) \Bigg\} \,,
\end{aligned}
\tag{7}
$$

$$
\begin{aligned}
B_2(\alpha_{2k}, \beta_{2k}, \gamma_{2k}, \delta_{2k}) = -\frac{1}{12\pi} \Bigg\{ & 5\widetilde{\Phi}_1^1(\alpha_{2k}) + 5\widetilde{\Phi}_1^1(\beta_{2k}) + 7\widetilde{\Phi}_1^1(0) + \widetilde{\Phi}_1^1(\gamma_{2k}) \\
& + \widetilde{\Phi}_1^1(\delta_{2k}) - 30\left(\alpha_1 + \frac{1}{12} \right)\widetilde{\Phi}_2^2(\alpha_{2k}) - 30\left(\beta_1 + \frac{1}{12} \right)\widetilde{\Phi}_2^2(\beta_{2k}) \\
& - 3\widetilde{\Phi}_2^2(0) - 6\gamma_1\widetilde{\Phi}_2^2(\gamma_{2k}) - 6\delta_1\widetilde{\Phi}_2^2(\delta_{2k}) \Bigg\} \,.
\end{aligned}
$$

Here

$$\alpha_1, \beta_1 = \frac{1}{12} + \frac{f^2 + \nu^2}{6\nu^2} \pm \frac{1}{2}\left(\frac{f^2 + \nu^2}{3\nu^2} - \frac{K+6}{6K} \right)\left[1 + \frac{4\lambda_k}{\kappa^2 f^2 K} \right]^{-1/2} \,, \tag{8}$$

$$\gamma_1, \delta_1 = \frac{1}{2(K-3)} \pm \frac{1}{2(K-3)}\left(1 - \frac{8\lambda_k}{\kappa^2 \nu^2 K} \right)^{-1/2} \,,$$

$$\alpha_{2k}, \beta_{2k} = \frac{\kappa^2 f^2}{k^2}\left\{ 1 \pm \left[1 + \frac{4\lambda_k}{\kappa^2 f^2 K} \right]^{1/2} \right\} \,, \tag{9}$$

$$\gamma_{2k}, \delta_{2k} = \frac{\kappa^2 \nu^2}{k^2}\left\{ 1 \pm \left[1 - \frac{8\lambda_k}{\kappa^2 \nu^2 (K-3)} \right]^{1/2} \right\} \,.$$

Note that $K = 3f^2/(f^2 + 2\nu^2)$, which corresponds to the choice of the so-called gauge-fixing independent effective action (for a review see Refs. 1 and 11). By this choice, we solve the gauge-dependence problem (for a related discussion in case of Einstein gravity, see Ref. 7). The functions $\Phi_n^p(w)$ and $\widetilde{\Phi}_n^p$ are given by the integrals

$$\Phi_n^p(w) = \frac{1}{\Gamma(n)} \int_0^\infty dz\, z^{n-1} \frac{R^{(0)}(z) - z R^{(0)'}(z)}{[z + R^{(0)}(z) + w]^p} , \tag{10}$$

$$\widetilde{\Phi}_n^p(w) = \frac{1}{\Gamma(n)} \int_0^\infty dz\, z^{n-1} \frac{R^{(0)}(z)}{[z + R^{(0)}(z) + w]^p} .$$

Solving (6),

$$\eta_N(k) = \frac{g_k B_1(\bar{\lambda}_k, \kappa_k)}{1 - g_k B_2(\bar{\lambda}_k, \kappa_k)} , \tag{11}$$

where $\kappa_k^2 = \kappa^2/k^2$, $\bar{\lambda}_k = \lambda_k/k^2$, we see that the anomalous dimension η_N is a non perturbative quantity. The evolution equation for the cosmological constant is obtained as follows:

$$\partial_t(\bar{\lambda}_k) = -[2 - \eta_N(k)]\bar{\lambda}_k + \frac{g_k}{4\pi}\{10\Phi_2^1(\alpha_{2k}) + 10\Phi_2^1(\beta_{2k}) - 10\Phi_2^1(0)$$

$$+ 2\Phi_2^1(\gamma_{2k}) + 2\Phi_2^1(\delta_{2k}) - \eta_N(k)[5\widetilde{\Phi}_2^1(\alpha_{2k}) + 5\widetilde{\Phi}_2^1(\beta_{2k}) + 7\widetilde{\Phi}_2^1(0)$$

$$+ \widetilde{\Phi}_2^1(\gamma_{2k}) + \widetilde{\Phi}_2^1(\delta_{2k})]\} . \tag{12}$$

Equations (5) and (12) with (11) determine the value of the running Newtonian constant and cosmological constant at the scale $k \ll \Lambda_{\text{cutoff}}$. The above evolution equations include nonperturbative effects which go beyond a simple one-loop calculation.

Next we estimate the qualitative behavior of the running Newtonian constant, as the above system of RG equations is too complicated and cannot be solved analytically. To this end we assume that the cosmological constant is much smaller than the IR cutoff scale, $\lambda_k \ll k^2$, so we can put $\lambda_k = 0$ to simplify Eqs. (8) and (9). After that, we make an expansion in powers of $(\bar{G}k^2)^{-1}$, keeping only the first term (i.e., we evaluate the functions $\Phi_n^p(0)$ and $\widetilde{\Phi}_n^p(0)$) and finally obtain (with $g_k \sim k^2 \bar{G}$)

$$G_k = G_0[1 - w\bar{G}k^2 + \dots] , \tag{13}$$

where

$$w = -\frac{1}{2}B_1(0,0) = \frac{1}{24\pi}\left[\left(50 + 22\frac{f^2}{\nu^2}\right) - \frac{7\pi^2}{3}\right].$$

In case of Einstein gravity, a similar solution has been obtained in Refs. 6 and 7. In getting (13) we use the same cutoff function as in Ref. 6.

We see that sign of w depends on higher-derivative coupling constants:

$$w > 0, \quad \text{if } 50 - \frac{7\pi^2}{3} + \frac{22f^2}{\nu^2} > 0 . \tag{14}$$

The coupling constant ν^2 may be chosen to be negative (see Ref. 1). For example, for $f^2 = 1$, $\nu^2 = \pm 1$ we get $w > 0$, and the Newtonian coupling decreases as k^2 increases; i.e., we find that the gravitational coupling is antiscreening. On the contrary, for $f^2 = 1$,

$\nu^2 = -1/2$ we get $w < 0$, and thus screening behavior of the Newtonian coupling. It means that in such a phase the gravitational charge (mass) is screened by quantum fluctuations, or, in other words, that the Newtonian coupling is smaller at smaller distances. The sign of the quantum correction to the Newtonian potential will be different as well.

Note that the above quantum correction to the Newtonian coupling constant has been calculated in Ref. 10 using the one-loop approach and perturbative RG equations. It is clear that the result of such a calculation is different from the one presented above, as we have used a nonperturbative RG method. Moreover, as we noted at the beginning, the theory under discussion is multiplicatively renormalizable in the perturbative approach, but most likely it is not unitary in that approach. Hence, the perturbative results cannot be trusted in many situations. On the contrary, within the nonperturbative approach the theory is considered as an effective theory, and problems with non-unitarity are therefore not important. The possibility of getting some nonperturbative results in models of QG in four dimensions looks very attractive and may aid in the construction of new QG models.

Thus we have found that Newtonian coupling may show screening or antiscreening behavior in R^2 gravity, depending on the higher-derivative couplings. That shows explicitly that R^2 quantum gravity may lead to different physical consequences than Einstein gravity even at low energies.

[a] e-mail: abyts@spin.hop.stu.neva.ru
[b] e-mail: granda@quantum.univalle.edu.co
[c] e-mail: odintsov@quantum.univalle.edu.co

[1] I. L. Buchbinder, S. D. Odintsov, and I. L. Shapiro, *Effective Action in Quantum Gravity*, IOP Publishing, Bristol, 1992.
[2] I. Antoniadis and E. Mottola, Phys. Rev. D **45**, 2013 (1992); S. D. Odintsov, Z. Phys. C **54**, 531 (1992).
[3] I. Antoniadis and S. D. Odintsov, Phys. Lett. B **343**, 76 (1995); E. Elizalde, S. D. Odintsov, and I. L. Shapiro, Class. Quantum Grav. **11**, 1607 (1994).
[4] H. W. Hamber and S. Liu, Phys. Lett. B **357**, 51 (1995).
[5] K. G. Wilson and J. Kogut, Phys. Rep. **12**, 75 (1974); J. Polchinski Nucl. Phys. B **231**, 269 (1984).
[6] M. Reuter, hep-th/9605030, 1996.
[7] S. Falkenberg and S. D. Odintsov, hep-th/9612019, 1996.
[8] J. Julve and M. Tonin, Nuovo Cimento B **46**, 137 (1978).
[9] A. Starobinsky, Phys. Lett. B **91**, 99 (1980).
[10] E. Elizalde, C. Lousto, S. D. Odintsov, and A. Romeo, Phys. Rev. D **52**, 2202 (1995).
[11] S. D. Odintsov, Fortschr. Phys. **38**, 371 (1990).

Search for the invisible axion emitted in the M1 transition in ^{125m}Te

A. V. Derbin,[a] A. I. Egorov, I. A. Mitropol'skiĭ, V. N. Muratova, S. V. Bakhlanov, and L. M. Tukhkonen

St. Petersburg Institute of Nuclear Physics, Russian Academy of Sciences, 188350 Gatchina, Leningrad District, Russia

A method of searching for the invisible axion emitted in M transitions of isomeric nuclei is proposed. It is determined experimentally that the probability of emission of an axion in the M1 transition in ^{125m}Te is $\leq 1.3 \cdot 10^{-5}$ (90% confidence level). © *1997 American Institute of Physics.* [S0021-3640(97)00308-3]

PACS numbers: 14.80.Mz, 23.20.Js, 23.20.Lv

Theoretical invisible-axion models in which the scale of symmetry breaking is arbitrary and can extend down to the Planck mass serve as a basis for the experimental search for a pseudoscalar particle which interacts weakly with matter and whose mass ranges from 10^{-12} eV up to tens of keV.[1–5] Although the limits on the axion mass obtained from astrophysical estimates[6,7] span almost the entire scale of possible masses, direct laboratory experiments give an upper limit of 6 keV for the axion mass.[8]

The ''missing γ ray'' method for nuclear magnetic transitions opens up new possibilities for axion searches.[9] If an ideal detector, which detects all particles arising from the decay of a nucleus, is developed, then the emission of the invisible axion which leaves the detector without any interactions will be accompanied by a shift of the spectrum by an amount equal to the M transition energy. Such events can be detected. In our view, it is preferable to study M transitions in isomeric nuclei primarily because there is no uncertainty associated with the emission of a neutrino, characteristic for nuclei undergoing β and EC decay.

EXPERIMENTAL SETUP

In the present work, the energy spectrum of photons and electrons which arises with the decay of a ^{125m}Te nucleus ($T_{1/2}$= 57 days) was analyzed in order to observe an axion. This isomeric nucleus undergoes two successive γ transitions with energies of 109.3 keV (M4 transition) and 35.5 keV (M1 transition, E2/M1 =0.029).[10] The decay scheme is shown in Fig. 1, together with the decay modes and the types of particles produced and their energy and probability of appearance per decay. Since the excited tellurium nucleus interacts with an atomic shell, each decay of a nucleus is accompanied by a cascade of γ rays, conversion electrons, x rays, and Auger electrons.

Two cylindrical planar HPGe detectors butted together at their end surfaces were used to measure the energy spectrum. A small recess, 0.5 mm deep and 3 mm in diam-
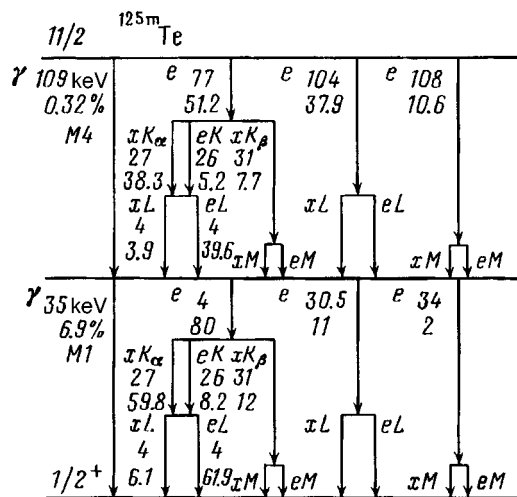
FIG. 1. Main modes of decay ^{125m}Te $\rightarrow$ ^{125}Te.

eter, was ground out at the center of the end face of one of the detectors to hold the ^{125m}Te source.

A preparation of tellurium of ''special radiation purity'' grade was specially prepared for this experiment. A strip of tin foil (0.1 g) was irradiated in a VVR-M reactor for one month in a flux of 10^{13} neutrons/cm$^2 \cdot$ s. After 60 days the tin was dissolved in hydrochloric acid and 5 mg of selenium was added to the solution obtained. The mixture of Se and ^{125m}Te was precipitated from the solution with tin dichloride, and the precipitate was washed and dissolved in 5.5 M HCl plus one drop of HNO$_3$. Radioactive tellurium was collected at the top of the chromatographic column with anionite. The column was first flushed with a 5.5 M solution of HCl, and then the ^{125m}Te zone was washed out, first with a 3 M solution and finally with a 1 M solution. The anionite purification operation was repeated three times, after which the solution of radiotellurium was evaporated in the presence of HNO$_3$ and 0.005 M H$_2$SO$_4$. A drop of the sulfuric acid solution was placed in a depression on the gold coating of the HPGe detector and the tellurium was deposited by electrolysis, forming an invisible spot 3 mm in diameter.

The working region of each detector was 40 mm in diameter and 7 mm thick. The configuration of the working volume of the two detectors ensured absorption of the 35-keV γ ray to a level of 10^{-14}. The absorption of the 109-keV photon was 97%, which increased the background near 100 keV somewhat on account of the backscattering of γ rays by the detector holder.

Before deposition of ^{125m}Te, the germanium detectors were placed in turn into a separate cryostat. The upper limit of the electron energy losses in the gold coating (30 μg/cm^2) and in the insensitive layer of the detector was determined with a ^{210}Bi source. For a 481.7-keV electron incident along the normal these losses did not exceed 0.2 keV, indicating that the detector could detect the L-series x rays of tellurium, which have an average energy of 4 keV, with an efficiency of 95%. If it is assumed that the coefficient

of out-diffusion of electrons from the detector surface equals 0.3 for the configuration employed, then it can be expected that the loss of 30-keV electrons as a result of multiple reflections will not exceed 10^{-5}. Like the Auger L electrons, the 4-keV conversion electrons are absorbed in the dead layer of the detector and do not contribute to the total energy released.

After the tellurium was deposited on one of the detectors, the detector was placed on the beryllium window of a spectrometer with a Si(Li) detector. The x-ray spectrum obtained in the decay of ^{125m}Te was measured with a resolution of 160 eV, and the probability of Auger L-electron emission was determined (0.91). This figure is of fundamental importance, since the proposed method permits distinguishing the emission of an axion from the absorption of a photon or electron in the insensitive layer of the detector. The probability of absorption in it is higher for a 27-keV x ray (or 30-keV electron) than for a 35-keV x ray (or 34-keV electron). At the same time, the L x rays accompanying such transitions are detected with nearly 100% efficiency, which will give rise to an additional intensity in the line, shifted to higher energies by 4 keV. According to the decay scheme in Fig. 1, when an axion is emitted in an M1 transition, two peaks with energies 104.5 and 108.3 keV and an intensity ratio of 2.9 should be observed in the total spectrum. If the energy shortfall is due to absorption of particles in the insensitive layer of the detector, the ratio of the intensities of the indicated peaks will decrease to 2.2. This difference can be a criterion of a positive result of an observation.

After the indicated measurements were performed, the HPGe detectors were placed up against each other in a cryostat and cooled to liquid-nitrogen temperature. The detectors had individual bias voltages of 1200 and 900 V, which were applied to the n^{+} contact; the potential of their common p contact was zero. Both detectors had similar spectrometric channels: a preamplifier with resistive feedback and a uncooled field-effect transistor and an amplifier with a formation time constant of 2 μs and a 12-digit ADC graduated to 60 eV/channel. The resolution measured with respect to the 122-keV γ line of ^{57}Co was 1.7 keV. The two channels were fed into an adder, the signal from which was fed into a separate ADC. The total energy spectrum from both detectors, the total spectra from each detector, and four spectra corresponding to coincidences and anticoincidences between detectors were stored in the computer memory. The two-dimensional energy spectrum was also stored in order to search for the optimal background/effect ratio.

RESULTS

A total of $1.4 \cdot 10^{8}$ decays of ^{125m}Te were detected over 62 h of measurements. A typical spectrum from one detector for one series of measurements is shown in Fig. 2. The spectrum contains 29 peaks, corresponding to different decay modes of ^{125m}Te and satellites associated with the emission of germanium x rays from the detector. The numbers *1* and *2* label the two main peaks, with intensities of about $1.5 \cdot 10^{5}$ keV^{-1} and energies of 27.4 ($K_{\alpha 1, \alpha 2}$) and 104.5 keV (e104, e77 + K_{α}). Peak *3* corresponds to the monochromatic 77-keV electron line. The resolution of the HPGe detector measured according to this line was 1.8 keV. The shift in the position of the peak, as determined according to the x-ray lines of tellurium and germanium, was 320 eV. This means that the average energy losses during passage through the insensitive layer of the detector were
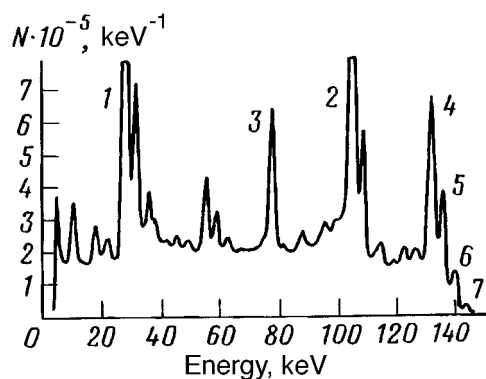
FIG. 2. Emission spectrum in ^{125m}Te decay, measured by one of the detectors. The maximum of peaks *1* and *2* equals $1.5 \cdot 10^6$ keV^{-1}.

equal to about 700 eV for 30-keV electrons. The lines *4*, *5*, and *6* are shifted by 4 keV to the left of the total-absorption peak (144.8 keV) — this is due to the loss of an x ray, conversion electron, or Auger electron.

The total spectrum from the two detectors is displayed in Fig. 3. As expected, the maximum of the peak corresponding to the total detected energy lies at 132 keV and not 144.8 keV. The energy shortfall is due to the loss of one or two Auger *L* electrons or one 4-keV conversion electron. Since the resolution for the total spectrum is 1.5 times worse, the right-hand edge of the peak possesses a profiled shape corresponding to unresolved peaks with energies of 136, 140, and 144 keV. The background level near 104 keV was equal to $1.4 \cdot 10^5$ keV^{-1} and was determined by the tails of the electron lines associated with multiple reflections of electrons from the surface of the detectors.

The maximum likelihood method was used to find the intensities of the 104.5-keV and 108.3-keV lines. The likelihood function was found from the assumption that the number of counts in each channel has a normal distribution and is a sum of an exponential function, chosen to describe the background, and the response function for the elec-
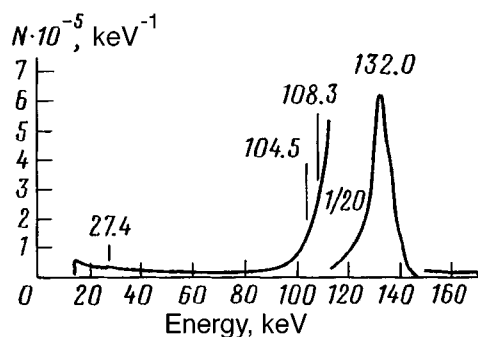

FIG. 3. Spectrum of the total detected energy. The intensity of the main peak is decreased by a factor of 20. The vertical lines indicate the positions of the expected axionic lines.

trons, which is determined from the total spectrum. The response function was represented as a Gaussian peak, whose variance was determined by the resolution of the composite detector, and an exponential tail with an area of 40%.

The value obtained for the ratio of the intensity of the axion radiation to the total intensity was $I_a/I_\gamma = (6 \pm 4) \cdot 10^{-6}$, which corresponds to a limit $I_a/I_\gamma \leqslant 1.3 \cdot 10^{-5}$ at the 90% confidence level.

Let us compare the above result with the theoretical estimates. As a result of the residual neutron–proton interaction in nuclei with two particles of one kind above a magic core and a half-filled shell of particles of the other kind, the spectra of such nuclei contain low-lying ''intruder'' states, corresponding to the deformed mean field, in addition to the single-particle states of a spherical nucleus. According to data from stripping and capture nuclear reactions, the lowest levels $1/2^+$, $3/2^+$, and $11/2^-$ in ^{125}Te are largely single-particle levels.[11] Their energetics can be explained by the presence of a negative deformation, $\epsilon \approx -0.1$.

In the energy region studied, the standard long-wavelength approximation for point nucleons can be used to determine the probabilities ω_γ and ω_a of nuclear electromagnetic and axionic transitions, respectively. In the single-particle approximation, when the nuclear transition is determined by the change in the state of a single nucleon and this nucleon is a neutron ($\mu_l(n) = 0$), the axion transition operator can be related with the magnetic transition operator having the same multipolarity:

$$\hat{T}(AL) = 2\frac{g_a^0 - g_a^1}{e\mu_s(n)}\hat{T}(ML), \tag{1}$$

where g_a^0 and g_a^1 are the isoscalar and isovector parameters of the axion–nucleon interaction, $\mu_s(n) = -3.827$ is the spin gyromagnetic ratio of the neutron. Taking account of the ratio (1) and the possibility of an admixture of an E2 transition, we obtain for the ratio of the axion and magnetic transition probabilities

$$\frac{\omega_a}{\omega_\gamma} = \frac{2(g_a^0 - g_a^1)^2 E_a^3}{(1 + \delta^2)e^2\mu_s^2(n)E_\gamma^3}, \tag{2}$$

where $E_a^2 = E_\gamma^2 - m_a^2$. For the axion–nucleon coupling constants we employ the values obtained in Refs. 12–14: $g_a^0 = -1.77 \cdot 10^{-5}$ $(m_a/1\ \text{keV})(1 + 2.94S)$, $g_a^1 = -2.75 \cdot 10^{-5}$ $(m_a/1\ \text{keV})$, and $S = 0.68$. The dependence of ω_a/ω_γ on m_a is bell-shaped, reaching a maximum value of $2.8 \cdot 10^{-6}$ at $m_a = 22$ keV. Therefore, our theoretical estimate is 4.6 times lower than our experimental estimate; this makes it impossible to establish a limit on the axion mass in the range 0–35 keV.

The sensitivity of the ''missing γ ray'' method can be increased. First, the background near 104 keV must be decreased; it is determined by the tails of the electron lines produced by multiple reflections of electrons from the surface of the detectors. For this, the thickness of the insensitive layer of the detector and the thickness and atomic number of the conducting coating must be decreased. The contribution of the natural radioactivity to the background is almost an order of magnitude smaller, but it also can be decreased by passive shielding. Increasing the measurement time and improving the resolution by

using cooled head cascades in the preamplifiers open up additional possibilities. Apparently, all of these measures will make it possible to reach a sensitivity to axion mass at a level of 1 keV.

[a]e-mail: derbin@lnpi.spb.su

[1] A. R. Zhitnitskiĭ, Yad. Fiz. **31**, 497 (1980) [Sov. J. Nucl. Phys. **31**, 497 (1980)].
[2] M. Dine, F. Fishler, and M. Sredniki, Phys. Lett. B **104**, 199 (1981).
[3] M. B. Wise, H. Georgi, and S. Glashow, Phys. Rev. Lett. **47**, 402 (1981).
[4] J. E. Kim, Phys. Rev. Lett. **43**, 103 (1979).
[5] M. A. Shifman, A. I. Vainstein, and V. I. Zakharov, Nucl. Phys. B **166**, 493 (1980).
[6] M. S. Turner, Phys. Rep. **197**, 67 (1990).
[7] G. G. Ruffelt, Phys. Rep. **198**, 1 (1990).
[8] R. M. Barnett, Y. Inoue, T. Asanuma, and M. Imamura, Phys. Rev. D **54**, 238 (1996).
[9] M. Miniwa, Y. Inoue, T. Asanuma, and M. Imamura, Phys. Rev. Lett. **71**, 4120 (1993).
[10] C. M. Lederer and V. S. Shirley, *Table of Isotopes*, Wiley, New York, 1978, Vol. 7.
[11] J. Katakura *et al.*, Nucl. Data Sheets **70**, 217 (1993).
[12] D. B. Kaplan, Nucl. Phys. B **260**, 215 (1985).
[13] M. Srednicki, Nucl. Phys. B **260**, 689 (1985).
[14] W. C. Haxton and K. Y. Lee, Phys. Rev. Lett. **66**, 2557 (1991).

Translated by M. E. Alferieff

Concerning experiments on coherent transition radiation by relativistic electrons

N. F. Shul'ga and S. N. Dobrovol'skiĭ

National Science Center, Kharkov Physicotechnical Institute,[a) 310108 Kharkov, Ukraine

It is shown that the macroscopic transverse dimensions of the target can strongly influence the spectrum of transition radiation emitted by relativistic electrons in thin layers of matter and that the effect is extremely important in experiments on coherent transition radiation in the infrared. © *1997 American Institute of Physics.* [S0021-3640(97)00408-8]

PACS numbers: 41.60.−m, 41.75.Ht

1. A series of experiments[1–3] was recently conducted in order to study the coherent transition radiation emitted by relativistic electrons in thin layers of matter. The measurements were performed on electron beams with an energy of the order of 100 MeV. The coherent transition radiation emitted by short bunches of an electron beam was investigated in the infrared region, where the thickness of the target is small compared with the wavelength of the emitted wave. The experimental results were analyzed using formulas from the theory of transition radiation for targets of infinite transverse size.[4–6]

This letter calls attention to the fact that for ultrarelativistic electrons the transverse distances responsible for the transition radiation process can be macroscopic, exceeding not only the transverse size of the target but also the size of the channel in which the beam moves. This situation occurs, specifically, in the experiments of Refs. 1–3. We shall show that when the finite macroscopic dimensions of the target are taken into account, the transition radiation spectrum becomes strongly distorted and the intensity of the radiation in the infrared range becomes much lower than in the case of a target of infinite transverse size. This circumstance is extremely important, because the intensity of the radiation that would be expected for a target of unbounded transverse size can be reduced by several orders of magnitude when the transverse dimensions of the target are taken into account. This effect occurs even for transition radiation of a single particle in a thin layer of matter. For this reason we shall analyze this very simple case here.

2. Let us consider the transition radiation of a relativistic electron passing through a thin layer of matter. To this end, we introduce the vector potential $\mathbf{A}(\mathbf{r},t)$ of the field of a particle moving in a medium with relative permittivity $\epsilon(\mathbf{r}) = 1 + \epsilon_1(\mathbf{r})$, where $\epsilon_1(\mathbf{r})$ is the correction to the vacuum value of the permittivity ($\epsilon_1(\mathbf{r}) =$ const inside and $\epsilon_1(\mathbf{r}) = 0$ outside the plate, respectively). Then the equation for the Fourier component $\mathbf{A}_\omega(\mathbf{r})$ of the field can be written in the form[7,8]

$$\left(\nabla^2 + \frac{\omega^2}{c^2}\right)\mathbf{A}_\omega(r) = -\frac{4\pi}{c}\mathbf{j}_\omega(\mathbf{r}) + \frac{\epsilon_1\omega^2}{c^2}\mathbf{A}_\omega(\mathbf{r}) + \epsilon\left(\vec{\nabla}\frac{1}{\epsilon}\right)\text{div }\mathbf{A}_\omega(r), \tag{1}$$

where $\mathbf{j}_\omega(\mathbf{r})$ is the Fourier component of the current density of the charge.

At large distances from the target ($R \to \infty$) the asymptotic solution of Eq. (1) is

$$\mathbf{A}_\omega|_{R \to \infty} = \frac{e^{ikR}}{cR} \int d^3 r e^{-i\mathbf{k} \cdot \mathbf{r}} \left\{ \mathbf{j}_\omega(\mathbf{r}) + \frac{c}{4\pi} \left(\epsilon_1(\mathbf{r}) \frac{\omega^2}{c^2} \mathbf{A}_\omega + \epsilon \left(\vec{\nabla} \frac{1}{\epsilon} \right) \operatorname{div} \mathbf{A}_\omega \right) \right\}, \tag{2}$$

where $\mathbf{k}$ is the wave vector in the direction of emission and $|\mathbf{k}| = \omega/c$. Knowing this asymptotic solution, we can construct the Poynting vector of the electromagnetic waves emitted by the particle and we can find the spectral–angular distribution of the radiation

$$\frac{dE}{d\omega do} = \frac{1}{4\pi^2 c} |\mathbf{k} \cdot (\mathbf{I}_e + \mathbf{I}')|^2, \tag{3}$$

where

$$\mathbf{I}_e = \int d^3 r e^{-i\mathbf{k} \cdot \mathbf{r}} \mathbf{j}_\omega(\mathbf{r}),$$

$$\mathbf{I}' = \frac{c}{4\pi} \int d^3 r e^{-i\mathbf{k} \cdot \mathbf{r}} \left(\frac{\omega^2}{c^2} \epsilon_1(\mathbf{r}) \mathbf{A}_\omega(\mathbf{r}) + \epsilon \left(\vec{\nabla} \frac{1}{\epsilon} \right) \operatorname{div} \mathbf{A}_\omega(\mathbf{r}) \right).$$

In our case of a thin target it can be assumed that the velocity of the particle is constant inside the target. Then $\mathbf{I}_e = 0$, and we are dealing only with transition radiation, which is determined by the nonuniformity of the permittivity $\epsilon(\mathbf{r})$. Furthermore, if

$$\epsilon_1 a_z \omega/c \ll 1, \tag{4}$$

where a_z is the thickness of the plate, then the field of the particle will change very little as the particle passes through the target. To a first approximation in the parameter (4), the solution of Eq. (1) will correspond to the vector potential of the field of the particle in vacuum

$$\mathbf{A}_\omega^0(\mathbf{r}) = \mathbf{n} \frac{2e}{c} e^{i\omega z/v} K_0(\rho \omega / v \gamma), \tag{5}$$

where e is the electron charge, γ is the Lorentz factor of the electron, $\mathbf{n}$ is a unit vector in the direction of the particle velocity $\mathbf{v}$, the z axis is parallel to $\mathbf{v}$, ρ is the transverse coordinate, and $K_0(x)$ is a modified Bessel function.[9] Substituting this expression for $\mathbf{A}_\omega^0$ into Eq. (3), we obtain the first term in the expansion of the spectral–angular radiation density in powers of the parameter $\epsilon_1 a_z \omega/c$. In the case when the particle passes through the center of a cylindrically symmetric thin plate with radius a_1, we find the following expression for the spectral distribution of the radiation in the angle interval $(\vartheta, \vartheta + d\vartheta)$:

$$\frac{d^2 E}{d\omega d\Omega} = \frac{d^2 E_\infty}{d\omega d\Omega} F^2(\gamma \sin \vartheta, \omega/\omega_\perp), \tag{6}$$

where $\omega_\perp = \gamma/a_\perp$, $d\Omega = \sin \vartheta d\vartheta$, and $d^2 E_\infty/d\omega d\Omega$ is the spectral–angular distribution of the radiation for a target with infinite transverse size ($a_\perp \to \infty$),[7,8]

$$\frac{d^2 E_\infty}{d\omega d\Omega} = \frac{2e^2}{\pi} \left(\frac{\epsilon_1 a_z \omega}{c} \right)^2 \frac{\sin^2 \vartheta}{(\sin^2 \vartheta + \gamma^{-2})^2}, \tag{7}$$

and the function $F(y,x)$ determines the effect of the transverse dimensions of the target on the transition radiation:

$$F(y,x) = \frac{y^2+1}{y}\left[\int_0^x u\,du\,K_1(u)J_1(yu) + \frac{\epsilon_1}{1+\epsilon_1}xK_0(x)J_1(yx)\right]. \tag{8}$$

Here $y = \gamma \sin \vartheta$, $z = \omega/\omega_\perp$, $K_1(x)$, $K_0(x)$, and $J_1(x)$ are the corresponding Bessel functions.[9]

The function $F(y,x)$ has a simple asymptotic form for small and large values of the argument x. If $x \gg 1$, then $F(y,x) \approx 1$. The spectral–angular density of transition radiation in this frequency range (i.e., for $\omega \gg \omega_\perp$) is identical to the corresponding result for a target of unbounded transverse size ($a_\perp \to \infty$).

However, if $x \ll 1$, i.e., $\omega \ll \omega_\perp$, then in the region of characteristic angles of the transition radiation $\vartheta \lesssim \gamma^{-1}$

$$F(y,x) = \frac{1}{4}(y^2+1)x^2\left[1 - 2\frac{\epsilon_1}{1+\epsilon_1}\left(C + \ln\frac{x}{2}\right)\right], \tag{9}$$

where $C = 0.577$ is the Euler constant. The spectral–angular radiation density in this frequency range decreases rapidly with ω and becomes small compared with the case $a_\perp \to \infty$ even for $\omega \sim \omega_\perp$. The integration over u in Eq. (8) corresponds to integration over the transverse radial coordinate of the target $\rho = v\gamma u/\omega$. The upper limit of the integral is determined by the transverse size of the target $\rho_{max} = a_\perp$. The main contribution to this integral comes from values

$$\rho_{eff} \lesssim \min(\lambda\gamma, a_\perp), \tag{10}$$

where $\lambda = c/\omega$ is the wavelength of the emitted wave. The second term in Eq. (8) is due to the transverse jump in the permittivity. For $\lambda\gamma \ll a_\perp$ the contribution of this term to the radiation spectrum can be neglected.

In summary, according to Eq. (6), the character of the transition radiation changes substantially for $\lambda\gamma \sim a_\perp$. In the frequency range where $\lambda\gamma \ll a_\perp$ the spectrum of the transition radiation does not depend on the transverse dimensions of the target. However, if $\lambda\gamma \gtrsim a_\perp$, then we find that the spectral density of the transition radiation is substantially suppressed in comparison with the spectral density in the limit $a_\perp \to \infty$. The parameters in the experiment of Ref. 1 were $\lambda \sim 0.1$ cm and $\gamma \sim 200$, so that $\lambda\gamma \sim 20$ cm. The transverse dimensions of the target in that experiment were 5×10 cm. Therefore in that experiment the transverse dimensions of the target should have had a large effect on the coherent transition radiation.

[a] e-mail: kfti@rocket.kharkov.ua

[1] Y. Shibata, K. Ishi, T. Takahashi *et al.*, Phys. Rev. E **49**, 785 (1994).
[2] Y. Shibata, K. Ishi, T. Takahashi *et al.*, Phys. Rev. A **44**, R3449 (1991); A **45**, R8340 (1992).
[3] U. Happek, A. J. Sievers, and E. B. Blum, Phys. Rev. Lett. **67**, 2962 (1991).
[4] V. L. Ginzburg and V. N. Tsytovich, *Transition Radiation and Transition Scattering* [in Russian], Nauka, Moscow, 1984.
[5] G. M. Garibyan, Zh. Éksp. Teor. Fiz. **33**, 1403 (1957) [Sov. Phys. JETP **6**, 1079 (1958)].

[6] V. E. Pafomov and I. M. Frank, Yad. Fiz. **5**, 631 (1967) [Sov. J. Nucl. Phys. **5**, 448 (1967)].

[7] G. M. Garibyan and Yan Shi, *X-Ray Transition Radiation* [in Russian], Arm. SSR Academy of Sciences Press, Erevan, 1983.

[8] M. L. Ter-Mikaelyan, *High-Energy Electromagnetic Processes in Condensed Media*, Wiley-Interscience, New York, 1972 [Russian original, Arm. SSR Academy of Sciences Press, Erevan, 1969].

[9] H. B. Dwight, *Tables of Integrals and Other Mathematical Data*, Macmillan, New York, 1961 [Russian translation, Nauka, Moscow, 1983].

Translated by M. E. Alferieff

Radiative energy loss of high-energy quarks in finite-size nuclear matter and quark–gluon plasma

B. G. Zakharov

Laboratoire de Physique Théorique et Hautes Energies, Université de Paris-Sud, 91405 Orsay Cedex, France; L.D.Landau Institute for Theoretical Physics, 117334 Moscow, Russia

The induced gluon radiation of a high-energy quark in a finite-size QCD medium is studied. For a sufficiently energetic quark produced inside a medium we find the radiative energy loss $\Delta E_q \propto L^2$, where L is the distance traveled by quark in the medium. It has a weak dependence on the initial quark energy E_q. The L^2 dependence turns to L^1 as the quark energy decreases. Numerical calculations are performed for a cold nuclear matter and a hot quark–gluon plasma. For a quark incident on a nucleus we predict $\Delta E_q \approx 0.1 E_q (L/10 \text{ fm})^\beta$, with β close to unity. © *1997 American Institute of Physics.* [S0021-3640(97)00508-2]

PACS numbers: 12.38.Qk, 13.60.Le, 25.20.Lj

The radiative energy loss of a high-energy parton in a QCD medium is currently under active investigation.[1–5] In classical electrodynamics the radiation of a charged particle in a dense medium was first considered long ago by Landau and Pomeranchuk.[6] The quantum treatment of this phenomenon was given by Migdal.[7] In Ref. 4 (see also Ref. 8) we developed a new path integral approach to the bremsstrahlung in a dense medium, applicable in both QED and QCD. In the present paper we evaluate within the formalism of Ref. 4 the radiative energy loss of a fast quark, ΔE_q, propagating through a finite-size uniform QCD medium. We consider both a cold nuclear matter and a hot quark–gluon plasma (QGP). Following Ref. 2, we model the QGP by a system of static scattering centers described by the Debye screened potential $\propto \exp(-r\mu_D)/r$, where μ_D is the color screening mass. For the screening mass we use perturbative formula $\mu_D = (1 + n_F/6)^{1/2} g_s T$ (Ref. 9), where $g_s = \sqrt{4\pi\alpha_s}$ is the QCD coupling constant, and T is the temperature of the QGP. We assume that a fast quark produced at $z = 0$ through a hard mechanism propagates in a medium of extent L along the z axis.

Neglecting the multigluon emission, we can write the radiative energy loss as

$$\Delta E_q = E_q \int_0^1 dx\, x \frac{dP}{dx}, \tag{1}$$

where E_q is the initial quark energy, x is the Feynman variable for the radiated gluon, and dP/dx is the probability of gluon radiation as function of x. In the approach of Ref. 4 the evaluation of dP/dx is reduced to solving a two-dimensional Schrödinger equation in impact-parameter space. The longitudinal coordinate z plays the role of time. This Schrödinger equation describes the evolution of the light-cone wave function of a fictitious

three-body $q\bar{q}g$ color singlet system. The relative positions of the constituents of the $q\bar{q}g$ system in the impact-parameter space are $\boldsymbol{\rho}_q=-\boldsymbol{\rho}x$, $\boldsymbol{\rho}_{\bar{q}}=0$, $\boldsymbol{\rho}_g=(1-x)\boldsymbol{\rho}$. The corresponding Hamiltonian has the form

$$H=\frac{\mathbf{p}^2}{2\mu(x)}+v(\boldsymbol{\rho},z),\tag{2}$$

$$v(\boldsymbol{\rho},z)=-i\frac{n(z)\sigma_3(\rho,x)}{2}.\tag{3}$$

Here $\mu(x)=E_qx(1-x)$ is the reduced "Schrödinger mass," $n(z)$ is the density of the medium, and $\sigma_3(\rho,x)$ is the cross section of interaction of the $q\bar{q}g$ system with a medium constituent (color center for QGP and nucleon for nuclear matter). In the case of QGP on the right-hand side of Eq. (3) there is an implicit summation over triplet (quark) and octet (gluon) color states.

In order to simplify the analysis we neglect the $q\to qg$ spin-flip transitions, which give a small contribution to the energy loss. Then the radiation rate is given by[4]

$$\frac{dP}{dx}=2\ \mathrm{Re}\int_0^\infty d\xi_1\int_{\xi_1}^\infty d\xi_2\ \exp\left[-\frac{i(\xi_2-\xi_1)}{L_f}\right]g(\xi_1,\xi_2,x)[K(0,\xi_2|0,\xi_1)$$

$$-K_v(0,\xi_2|0,\xi_1)].\tag{4}$$

Here the generalization of the QED vertex operator of Ref. 4 to QCD reads

$$g(\xi_1,\xi_2,x)=\frac{\alpha_s[4-4x+2x^2]}{3x}\frac{\mathbf{p}(\xi_2)\cdot\mathbf{p}(\xi_1)}{\mu^2(x)},\tag{5}$$

K is the Green's function for the Hamiltonian (2), K_v is the vacuum Green's function, $L_f=2E_qx(1-x)/[m_q^2x^2+m_g^2(1-x)]$ is the so called gluon formation length (time), m_q is the quark mass, and m_g is the mass of the radiated gluon. The latter plays the role of an infrared cutoff, removing the contribution of the long-wavelength gluon excitations, which cannot be treated perturbatively. In contrast to the expression of Ref. 4 for the bremsstrahlung spectrum of an electron incident on the target of Ref. 4, in which the integration over ξ_1 starts from $-\infty$, in Eq. (4) we integrate over ξ_1 from $\xi_1=0$, i.e., from the point where a fast quark is produced by hard scattering.

The three-body cross section entering the imaginary potential (3) can be expressed in terms of the dipole cross section for color singlet $q\bar{q}$ pair,[10] $\sigma_2(\rho)$,

$$\sigma_3(\rho,x)=\frac{9}{8}[\sigma_2(\rho)+\sigma_2((1-x)\rho))]-\frac{1}{8}\sigma_2(x\rho).\tag{6}$$

The radiation rate is dominated by the contribution from $\rho\lesssim1/m_g$ (Ref. 4), where $\sigma_2(\rho)=C_2(\rho)\rho^2$ and $C_2(\rho)$ has a smooth (logarithmic) dependence on ρ.[11,10] This allows one to estimate the energy loss by replacing $C_2(\rho)$ by $C_2(1/m_g)$. Then $\sigma_3(\rho,x)=C_3(x)\rho^2$, with $C_3(x)=\{9[1+(1-x)^2]-x^2\}C_2(1/m_g)/8$, and the Hamiltonian (1) takes the oscillator form with the frequency

$$\Omega = \frac{1-i}{\sqrt{2}} \left(\frac{n(z)C_3(x)}{\mu(x)} \right)^{1/2} = \frac{1-i}{\sqrt{2}} \left(\frac{n(z)C_3(x)}{E_q x(1-x)} \right)^{1/2}.$$

Making use of the oscillator Green's function after some algebra one can represent the bremsstrahlung rate (4) in the form

$$\frac{dP}{dx} = Ln \frac{d\sigma^{BH}}{dx} S(\eta, l), \tag{7}$$

where

$$\frac{d\sigma^{BH}}{dx} = \frac{4\alpha_s C_3(x)(4-4x+2x^2)}{9\pi x[m_q^2 x^2 + m_g^2(1-x)]}, \tag{8}$$

is the Bethe–Heitler cross section. The suppression factor $S(\eta, l)$, depending on the dimensionless variables

$$\eta = L_f |\Omega| = \frac{[4nC_3(x)E_q x(1-x)]^{1/2}}{m_q^2 x^2 + m_g^2(1-x)}, \tag{9}$$

$$l = L/L_f = \frac{L[m_q^2 x^2 + m_g^2(1-x)]}{2E_q x(1-x)}, \tag{10}$$

is given by

$$S(\eta, l) = S^{(1)}(\eta, l) + S^{(2)}(\eta, l), \tag{11}$$

$$S^{(1)}(\eta, l) = \frac{3}{l\eta^2} \operatorname{Re} \int_0^{l\eta} dy_1 \int_0^{y_1} dy_2 \, \exp\left(-\frac{iy_2}{\eta}\right) \left\{ \frac{1}{y_2^2} - \left[\frac{\phi}{\sin(\phi y_2)} \right]^2 \right\}, \tag{12}$$

$$S^{(2)}(\eta, l) = \frac{3}{l\eta^2} \operatorname{Re} \int_0^{l\eta} dy_1 \int_0^{\infty} dy_2 \, \exp\left[-\frac{i(y_1+y_2)}{\eta}\right]$$

$$\times \left\{ \frac{1}{(y_1+y_2)^2} - \left[\frac{\phi}{\cos(\phi y_1)(\tan(\phi y_1) + \phi y_2)} \right]^2 \right\}, \tag{13}$$

with $\phi = \Omega/|\Omega| = \exp(-i\pi/4)$. The two terms on the right-hand side of (11) correspond in (4) to the contributions from the integration regions $\xi_1 < \xi_2 < L$ and $\xi_1 < L < \xi_2$, respectively. The variables in (12), (13) in terms of those in (4) are $y_1 = (L-\xi_1)|\Omega|$, $y_2 = (\xi_2 - \xi_1)|\Omega|$ (in (12)) and $y_2 = (\xi_2 - L)|\Omega|$ (in (13)). In arriving at (13) we have used a representation of the first Green's function in the square brackets in (4) in terms of a convolution of the oscillator Green's function (for the interval (ξ_1, L)) and the vacuum one (for the interval (L, ξ_2)). Notice that the functional form of our results at $x \ll 1$ differs from the one obtained in Ref. 5 within the soft gluon approximation.

In a medium it is either L_f or $1/|\Omega|$ which sets the effective medium-modified formation length $L_f' = \min(L_f, 1/|\Omega|)$, which is the typical value of $\xi_2 - \xi_1$ in (4) for $L \gg L_f'$. The finite-size effects come into play only at $L \lesssim L_f'$, i.e., $l \lesssim l_0 = \min(1, 1/\eta)$. From (11)–(13) we find $S(\eta, l) \approx -l^2 \log l$ as $l \to 0$. The source of this suppression of radiation at small L is obvious: the energetic quark produced through a hard mechanism

loses the soft component of its gluon cloud, and radiation at distances shorter than the time required for regeneration of the quark gluon field turns out to be suppressed. For $l \gg l_0$ the expression for $S(\eta, l)$ reduces to that for the infinite medium, for which the expressions $S(\eta, l = \infty) \approx 3/\eta\sqrt{2}$ ($\eta \gg 1$) and $S(\eta, l = \infty) \approx 1 - 16\eta^4/21$ ($\eta \ll 1$) were derived in Ref. 4. Notice that according to Eqs. (9) and (10), $\eta \to 0$ and $l \to \infty$ as $x \to 0,1$, and the Bethe–Heitler regime obtains in these limits.

Before presenting the numerical result, let us consider the energy loss at a qualitative level. We begin with the case of a sufficiently large E_q such that the maximum value of L_f', $L_f'(\text{max})$, is much bigger than L. Taking into account the finite-size suppression of radiation at $L_f' \gtrsim L$, we find that ΔE_q is dominated by the contribution from two narrow regions of x: $x \lesssim \delta_g \approx Lm_g^2/2l_0 E_q$ and $1 - x \lesssim \delta_q \approx Lm_q^2/2l_0 E_q$. In both the regions the finite-size effects are marginal and the energy loss can be estimated using the infinite medium suppression factor. For instance,

$$\Delta E_q(x \lesssim \delta_g) \sim \frac{16\alpha_s C_3(0) E_q Ln}{9\pi m_g^2} \int_0^{\delta_g} dx\, S(\eta(x), l = \infty). \tag{14}$$

Using (9) one can show that $\eta(x \lesssim \delta_g) \lesssim 1$ at $L \lesssim m_g^2/2nC_3(0)$. In this region of L in (14) we can put $S(\eta(x), l = \infty) \approx 1$ and find $\Delta E_q \sim 0.25\alpha_s C_3(0)nL^2$, which does not depend on the quark energy. At $L \gg m_g^2/2nC_3(0)$ the typical values of η in (14) are much bigger than unity, and using the asymptotic formula for the suppression factor we obtain $\Delta E_q \sim \alpha_s C_3(0)nL^2$. A similar analysis for x close to unity gives a contribution to ΔE_q suppressed by a factor of $\sim 1/4$ as compared to that for small x. Notice that in this L^2 regime, despite the $1/m_{g,q}^2$ infrared divergence of the Bethe–Heitler cross section, ΔE_q has only a smooth m_g dependence originating from the factor C_3. We emphasize that the above analysis of the origin of the leading contributions makes it evident that L^2 dependence of ΔE_q cannot be regarded as a consequence of the Landau–Pomeranchuk–Migdal suppression of the radiation rate due to small-angle multiple scatterings.

The finite-size effects can be neglected and ΔE_q becomes proportional to L if $L_f'(\text{max}) \ll L$. If in addition the typical values of η are much bigger than unity, from (1), (7), (8) along with the asymptotic form of $S(\eta, l = \infty)$ at $\eta \gg 1$ one can obtain the following infrared-stable result: $\Delta E_q \approx 1.1\alpha_s L\sqrt{nC_3(0)E_q}$.

In numerical calculations we take $m_g = 0.75$ GeV. This value of m_g was obtained in Ref. 12 from the analysis of HERA data on the structure function F_2 within the dipole approach[13] to the BFKL equation. It is also consistent with the nonperturbative estimate[14] of the gluon correlation radius in the QCD vacuum. For scattering of the $q\bar{q}g$ system on a nucleon, we find from the double gluon model[11] that $C_2(1/m_g) \sim 1.3$–4, where the lower and upper bounds correspond to the t-channel gluon propagators with masses of 0.75 and 0.2 GeV, respectively. The latter choice allows one to reproduce the dipole cross section extracted from the data on vector meson electroproduction.[15] However, there is every indication[12,13] that a considerable part of the dipole cross section obtained in Ref. 15 comes from the nonperturbative effects, for which our approach is not justified. For this reason we take $C_2(1/m_g) = 2$, which seems to be a plausible estimate for the perturbative component of the dipole cross section.[12]

For scattering of the $q\bar{q}g$ system on a color center we estimated $C_2(1/m_g)$ using the double gluon formula with the Debye screened gluon exchanges. For $T=250$ MeV we obtained $C_2(1/m_g)\approx 0.5$ for a triplet center. For an octet center the result is $C_A/C_F=9/4$ times larger, where $C_A(C_F)$ is the octet (triplet) second-order Casimir invariant. For the quark mass, which controls the transverse size of the $q\bar{q}g$ system at $x\approx 1$, we take $m_q=0.2$ GeV. Notice that our prediction for ΔE_q is insensitive to the value of m_q.

For nuclear matter, taking $n=0.15$ fm^{-3} and $\alpha_s=1/2$ for $L\lesssim 5$ fm we obtained $\Delta E_q\approx a(L/5\text{ fm})^\beta$, with $a\approx$ 0.55, 1, 1.23 GeV and $\beta\approx$ 1.5, 1.85, 1.95 for $E_q=$ 10, 50, and 250 GeV. Calculations with $\alpha_s=1/3$ for QGP at $T=250$ MeV yield for the same energies: $a\approx$ 4.2, 10.2, 14.8 GeV and $\beta\approx$ 1.2, 1.65, 1.9. The above values of β were determined for $L\lesssim 5$ fm. In the region $5\lesssim L\lesssim 10$ fm β is 10–20% smaller. At $E_q\gtrsim 250$ GeV a and β flatten. Notice that $L_f'(\max)\sim 5$–10 fm for $E_q\sim 10$–40 GeV in nuclear matter and for $E_q\sim 150$–600 GeV in QGP. Thus our numerical results say that the onset of the L^2 regime takes place when $L_f'(\max)/L\gtrsim 2$. The closeness of β to unity at $E_q=10$ GeV for QGP agrees with a small value of $L_f'(\max)$ (~ 1 fm). We checked that variation of m_q gives a small effect. The m_g dependence of ΔE_q becomes weak at $E_q\gtrsim 50$ GeV. However, it is sizeable for $E_q\sim 10-20$ GeV. For instance $\Delta E_q(m_g=0.375)/\Delta E_q(m_g=0.75)\sim 1.5$ at $E_q=10$ GeV, $L\sim 5$ fm. Our predictions for ΔE_q must be regarded as rough estimates with uncertainties of at least a factor of 2 in either direction. Nevertheless, the rather large values of ΔE_q obtained for QGP indicate that the jet quenching may be an important potential probe for formation of the deconfinement phase in AA collisions.

We also studied the energy loss of a fast quark incident on a target. In this case radiation by the initial quark is allowed, and the lower limit of integration over ξ_1 in (4) must be replaced by $-\infty$. For the case of bremsstrahlung in QED this situation was discussed in Ref. 8. It was shown that after the medium Green's function is expanded in a series in the potential, the spectrum can be represented as a sum of the Bethe–Heitler term and an absorptive correction. For our choice of the gluon mass the absorptive correction is relatively small. This means that $\Delta E_q\propto E_q Ln\,\alpha_s C_3(0)/m_g^2$. For nuclear matter in the region $L\lesssim 10$ fm the numerical calculations give $\Delta E_q\approx 0.1E_q(L/10\text{ fm})^\beta$ with $\beta\approx 0.9$–1 for $E_q\lesssim 50$ GeV and $\beta\approx 0.85-0.9$ for $E_q\gtrsim 200$ GeV. This result differs drastically from the prediction of Ref. 1: $\Delta E_q\approx 0.25(L/1\text{ fm})$ GeV. Our estimate is in qualitative agreement with the longitudinal energy flow measured in hard pA collisions with a dijet final state[16] and with the energy loss obtained from the analysis of the inclusive hadron spectra in hA interactions.[17]

[1] S. J. Brodsky and P. Hoyer, Phys. Lett. B **298**, 165 (1993).
[2] M. Gyulassy and X.-N. Wong, Nucl. Phys. B **420**, 583 (1994); X.-N. Wong, M. Gyulassy, and M. Plümer, Phys. Rev. D **51**, 3436 (1995).
[3] R. Baier, Yu. L. Dokshitzer, S. Peigne, and D. Schiff, Phys. Lett. B **345**, 277 (1995).
[4] B. G. Zakharov, JETP Lett. **63**, 952 (1996).
[5] R. Baier, Yu. L. Dokshitzer, A. H. Mueller *et al.*, Nucl. Phys. B **483**, 291 (1997); Nucl. Phys. B **484**, 265 (1997).

[6] L. D. Landau and I. Ya. Pomeranchuk, Dokl. AN SSSR **92**, 535, 735 (1953).

[7] A. B. Migdal, Phys. Rev. **103**, 1811 (1956).

[8] B. G. Zakharov, JETP Lett. **64**, 781 (1996).

[9] E. V. Shuryak, Phys. Rep. **61**, 71 (1980).

[10] N. N. Nikolaev and B. G. Zakharov, Zh. Éksp. Teor. Fiz. **105**, 1117 (1994) [JETP **78**, 598 (1994)].

[11] F. E. Low, Phys. Rev. D **12**, 163 (1975); S. Nussinov, Phys. Rev. Lett. **34**, 1286 (1975).

[12] N. N. Nikolaev and B. G. Zakharov, Phys. Lett. B **327**, 149 (1994).

[13] N. N. Nikolaev, B. G. Zakharov, and V. R. Zoller, Phys. Lett. B **328**, 486 (1994).

[14] E. V. Shuryak, Rev. Mod. Phys. **65**, 1 (1993).

[15] J. Nemchik, N. N. Nikolaev, E. Predazzi, and B. G. Zakharov, Phys. Lett. B **374**, 199 (1996).

[16] R. C. Moore, R. K. Clark, M. Corcoran *et al.*, Phys. Lett. B **244**, 347 (1990).

[17] E. Quack and T. Kodama, Phys. Lett. B **302**, 495 (1993).

Grand unification and heavy axion

V. A. Rubakov

Institute for Nuclear Research of the Russian Academy of Sciences, 117312 Moscow, Russia

We argue that sufficiently complex grand unified theories involving extra strong intractions that confine at very short distances may lead to a heavy axion solution of the CP problem of QCD. This axion may have a mass within the accessible energy range, and its low-energy interactions emerge through mixing with axial Higgs boson(s). Another signature of this scenario is softly broken Peccei–Quinn symmetry in the electroweak Higgs sector. We present a toy GUT exhibiting these features. © *1997 American Institute of Physics.*
[S0021-3640(97)00608-7]

PACS numbers: 12.10.−g, 14.80.Mz

In QCD, the effective θ-parameter $\bar{\theta} = \theta + \arg \det M_{\text{quark}}$ breaks CP (Ref. 1) and is experimentally constrained to be unnaturally small, $\bar{\theta} \lesssim 10^{-10}$ (for reviews see, e.g., Ref. 2). An elegant solution to this strong CP problem is based on the Peccei–Quinn (PQ) symmetry[3] and predicts a light particle, an axion. In view of constraints obtained from experimental searches for the Weinberg–Wilczek[4] axion, a widely accepted option is an extremely light invisible axion.[5] A potential problem with the latter comes from possible non-renormalizable terms in the low-energy Lagrangian, which may be due to very high (say, Planckian) scales and need not respect PQ symmetry.[6] Negligible for other purposes, these terms would introduce an extra axion potential and ruin the PQ mechanism precisely because the QCD contribution to the axion potential is tiny. From this point of view it is safer to have the axion heavy enough.

In this paper we point out that heavy axions may appear in sufficiently complex grand unified theories containing extra gauge interactions (with unbroken gauge group) which become strong well above the accessible energies. The effective θ-parameters of QCD and these extra strong interactions may be equal to each other due to a symmetry built into a GUT. If there is *one* PQ symmetry relevant to *both* QCD and the extra strong interactions, the PQ mechanism rotates away both of these θ-parameters, and the axion obtains its mass predominantly from the extra strong interactions and is therefore heavy (much heavier than the Weinberg–Wilczek axion).

A similar idea was put forward by Tye[7] in the context of technicolor plus Higgs models with PQ symmetry. However, many (if not all) such models predict numerous pseudo-Goldstone bosons; some of these are charged and have masses well below 40 GeV, which is ruled out experimentally. This problem is not inherent in GUTs.[a]

To be specific, let us consider a toy GUT. This model is realistic for several reasons,

but we expect that it will pick up generic features of possible heavy axions. The model is a non-supersymmetric GUT with the gauge group $SU(5) \times SU(5)$, where the first $SU(5)$ is meant to model the real world and the second $SU(5)$ is a mirror group. Let the fermionic and Higgs content be mirror symmetric. Ordinary (mirror) fermions are singlets under mirror (ordinary) $SU(5)$ and form the usual $\bar{5}$- and 10-plets under ordinary (mirror) $SU(5)$. There are one Higgs 24-plet and two Higgs 5-plets in each $SU(5)$ sector which are singlets under partner $SU(5)$. Let us require that at this stage each $SU(5)$ sector has its own PQ symmetry that rotates the two Higgs 5-plets in the opposite ways,

$$\varphi_5^{(1)} \rightarrow e^{i\alpha} \varphi_5^{(1)}, \quad \varphi_5^{(2)} \rightarrow e^{-i\alpha} \varphi_5^{(2)} \tag{1}$$

for ordinary Higgs 5-plets $\varphi_5^{(1,2)}$, and

$$\Phi_5^{(1)} \rightarrow e^{i\beta} \Phi_5^{(1)}, \quad \Phi_5^{(2)} \rightarrow e^{-i\beta} \Phi_5^{(2)} \tag{2}$$

for mirror Higgs 5-plets $\Phi_5^{(1,2)}$. To have just one PQ symmetry, let us introduce an $SU(5) \times SU(5)$ singlet complex scalar field S of PQ charge 1 that interacts with both ordinary and mirror Higgs 5-plets,

$$L_{S,\varphi,\Phi} = h \varphi_5^{(1)\dagger} \varphi_5^{(2)} S^2 + h' \Phi_5^{(1)\dagger} \Phi_5^{(2)} S^2 + \text{h.c.} \tag{3}$$

The self-interaction of S is required to be symmetric under the phase rotations of S, so the remaining PQ symmetry is (1), (2) with $\beta = \alpha$ and $S \rightarrow e^{i\alpha} S$. Let us assume for definiteness that S does not obtain vacuum expectation value, though this assumption is not crucial for further discussion.

Let us now require that at the (high) energy scales where both $SU(5)$ groups are unbroken, the hard (dimension 4) terms in the whole Lagrangian are mirror symmetric, while the soft terms are not. This implies, in particular, that $\theta_{\text{ordinary}} = \theta_{\text{mirror}}$ (the θ terms are hard) and that the phases of Yukawa couplings are the same in ordinary and mirror sectors. This requirement also implies the equality of the couplings entering Eq. (3), $h' = h$. Hence, without loss of generality one sets h to be real (the phase of h can be rotated away by the phase rotation of S). In one loop, the interaction (3) introduces a direct interaction between ordinary and mirror Higgs 5-plets,

$$L_{\varphi,\Phi} = \lambda (\varphi_5^{(1)\dagger} \varphi_5^{(2)}) \cdot (\Phi_5^{(2)\dagger} \Phi_5^{(1)}) + \text{h.c.}, \tag{4}$$

where $\lambda \propto h^2 \ln(m_S/\mu)$ and μ is the normalization scale. Note that λ is real and the interaction (4) is still PQ symmetric.

Let us require that, just like ordinary $SU(5)$, mirror $SU(5)$ breaks down to $SU(3)_{mc} \times U(1)_{mEM}$, where mc and mEM refer to mirror color and mirror electromagnetism, respectively. Since the soft terms of the mirror sector are different from those of ordinary sector, this breaking occurs at different energy scales. Consider the case when mirror $SU(5)$ breaks down at much lower energy than the ordinary GUT scale. The coupling constant of $SU(5)$ runs faster than that of $SU(3)$, so the mirror coupling constant is larger than that of ordinary $SU(3)_c$ at the point where mirror $SU(5)$ breaks down. Hence, $SU(3)_{mc}$ becomes strong at a scale Λ_{mc} which is larger than the ordinary Λ_{QCD}. Assuming

$$\langle \Phi_5^{(1)} \rangle \sim \langle \Phi_5^{(2)} \rangle \sim v_m > \Lambda_{mc} \tag{5}$$

we have the mirror world similar to the ordinary world, but scaled up in energy (and with v_m/Λ_{mc} not necessarily of the same order as the ratio of the ordinary Higgs expectation value to the QCD confinement scale, $v/\Lambda_{QCD}\sim 10^3$).

By the mirror symmetry of the hard terms, the effective θ-parameters of the ordinary and mirror sectors are equal to each other,[b] at least at the tree level. By performing PQ rotation, one makes both of them equal to zero. By the mirror PQ mechanism, the axion field then takes a zero vacuum expectation value, and both the mirror and ordinary strong interactions conserve CP. In other words, at a nonzero mirror effective θ-parameter $\overline{\theta}_{mirror}$ the phase of the vacuum expectation value of $\Phi_5^{(1)\dagger}\Phi_5^{(2)}$ is proportional to $\overline{\theta}_{mirror}$ by the PQ mechanism; the interaction (4) aligns the phase of $\varphi_5^{(1)\dagger}\varphi_5^{(2)}$ to the same value, so the effective ordinary θ-parameter, after PQ rotation, becomes equal to $\overline{\theta}_{ordinary}-\overline{\theta}_{mirror}=0$, at least at the tree level.[c]

The axion obtains its mass predominantly due to mirror strong interactions. It is, in fact, a mirror Weinberg–Wilczek axion. The expression for the mass is a scaled-up version of the Weinberg formula. Recalling that the mass of the Weinberg–Wilczek axion scales as $m_{WW}\propto\Lambda_{QCD}^{3/2}v^{1/2}$, we estimate the axion mass in our model as

$$M_a\sim\left(\frac{\Lambda_{mc}}{\Lambda_{QCD}}\right)^{3/2}\left(\frac{v}{v_m}\right)^{1/2}m_{WW}.$$

This may certainly be much larger that m_{WW}.

To get an idea of the numbers, let us point out that non-supersymmetric $SU(5)$ becomes strong at about 10^5 GeV. Hence, $\Lambda_{mc}\lesssim10^5$ GeV. Under the assumption (5) and using $m_{WW}\sim100$ keV, we have

$$M_a\lesssim1\text{ TeV}.$$

Let us stress that by varying Λ_{mc} and v_m one can easily get the axion much lighter than 1 TeV. Say, at $\Lambda_{mc}\sim3$ TeV and $v_m\sim10$ TeV one has $M_a\sim20$ GeV.

The axion interactions with ordinary matter come from the term (4). At energies below v_m we have

$$\Phi_5^{(2)\dagger}\Phi_5^{(1)}=c_1v_m^2+ic_2v_ma(x), \tag{6}$$

where c_1 and c_2 are constants of order 1, and $a(x)$ is the axion field. The first term here produces the off-diagonal mass term for the ordinary Higgs fields that breaks the low-energy PQ symmetry (1) explicitly and softly. The corresponding mass parameter, $m_{12}=\sqrt{\lambda c_1}v_m$ should be of the order of 100 GeV to avoid fine tuning in the ordinary electroweak Higgs sector. The second term in Eq. (6), on being inserted into Eq. (4), induces mixing between axion and axial Higgs boson A^0 which is of order m_{12}^2v/v_m. Hence, one expects a mixing angle

$$|\theta_{a,A^0}|\sim\frac{v}{v_m}\frac{m_{12}^2}{|M_{A^0}^2-M_a^2|}.$$

With $v_m\sim10^4$–10^5 GeV this angle is in the range 10^{-2}–10^{-4}, but this estimate is again strongly parameter-dependent, and the mixing may be somewhat higher.

Thus, in our toy model the axion is a relatively light remnant of extra strong interactions operating at very short distances. The axion mass may be well within the accessible range of energies; its interactions with ordinary matter come from mixing with the axial Higgs boson A^0, and the mixing angle may not be negligibly small. The scalar potential of the ordinary Higgs fields exhibits softly broken PQ symmetry. We expect that these features are generic to the class of grand unified theories where the strong CP problem is solved in the way discussed in this paper.

[a] Mechanisms that may make invisible axion heavy enough are discussed in Ref. 8.

[b] Note that the soft terms consistent with PQ symmetry do not contain phases, which otherwise would be different in the ordinary and mirror sectors.

[c] The effective θ of ordinary strong interactions may acquire radiative corrections, but they are small.[9]

[1] G. 't Hooft, Phys. Rev. Lett. **37**, 172 (1976).

[2] N. V. Krasnikov, V. A. Matveev, and A. N. Tavkhelidze, Elem. Chast. At. Yad. **12**, 100 (1981) [Sov. J. Part. Nucl. **12**, 38 (1981)]; J. E. Kim, Phys. Rep. **150**, 1 (1987).

[3] R. D. Peccei and H. Quinn, Phys. Rev. Lett. **38**, 1440 (1977).

[4] S. Weinberg, Phys. Rev. Lett. **40**, 223 (1978); F. Wilczek, Phys. Rev. Lett. **40**, 279 (1978).

[5] J. E. Kim, Phys. Rev. Lett. **43**, 103 (1979); M. Shifman, A. Vainshtein, and V. Zakharov, Nucl. Phys. B **166**, 493 (1980); A. R. Zhitnitsky, Yad. Fiz. **31**, 497 (1980) [Sov. J. Nucl. Phys. **31**, 260 (1980)]; M. Dine, W. Fischler, and M. Srednicki, Phys. Lett. B **104**, 199 (1981).

[6] R. Holman, S. Hsu, T. Kephart *et al.*, Phys. Lett. B **282**, 132 (1992); M. Kamionkowski and J. March-Russell, Phys. Lett. B **282**, 137 (1992); S. Barr and D. Seckel, Phys. Rev. D **46**, 539 (1992); S. M. Lusignioli and M. Roncadelli, Phys. Lett. B **283**, 278 (1992); R. Kallosh, A. Linde, D. Linde and L. Susskind, Phys. Rev. D **52**, 912 (1995).

[7] S.-H. H. Tye, Phys. Rev. Lett. **47**, 1035 (1981).

[8] B. Holdom and M. Peskin, Nucl. Phys. B **208**, 397 (1982); B. Holdom, Phys. Lett. B **154**, 316 (1985).

[9] J. Ellis and M. K. Gaillard, Nucl. Phys. B **150**, 141 (1979); I. B. Khriplovich, Phys. Lett. B **173**, 193 (1986); I. B. Khriplovichand A. I. Vainshtein, Nucl. Phys. B **414**, 27 (1994).

Published in English in the original Russian journal. Edited by Steve Torstveit.

Observation of coherent x-ray production by 800-MeV electrons in a periodic triple-crystal target

M. Yu. Andreyashkin, V. N. Zabaev, V. V. Kaplin,[a] and S. R. Uglov

Scientific-Research Institute of Nuclear Physics at Tomsk Polytechnical, University, 634050 Tomsk, Russia

K. Nakayama

Toshiba Corporation, 210 Kawasaki, Japan

I. Endo

Hiroshima University, 739 Higashi–Hiroshima, Japan

The production of coherent x radiation by 800-MeV electrons in a target consisting of three 16-μm silicon crystals is investigated at the Tomsk synchrotron. The target structure makes it possible to observe from each crystal in turn, as the target is rotated, the radiation due to the summation of parametric x radiation (PXR) and the diffracted resonance transition radiation (DRTR) produced at the surfaces of the preceding crystals. The orientational dependence obtained shows that the contribution of the DRTR increases with the number of the crystal in the series, so that the angular density of the DRTR from the third crystal is approximately 1.7 times higher than the density of the PXR. © *1997 American Institute of Physics.* [S0021-3640(97)00708-1]

PACS numbers: 41.50.+h, 78.70.−g

A new concept for the generation of coherent x rays by relativistic electrons in complex periodic structures has been developed in a series of recent works.[1–4] According to this concept, narrowly directed (at large angles to the axis of the electron beam) quasimonochromatic x radiation is generated by passing electrons through composite targets of the type "layered structure + crystal" or assemblies of several thin, mutually oriented crystals. Here, besides parametric x radiation (PXR), there appears an additional contribution on account of the diffraction of the transition x radiation.

The well-studied electron PXR, generated in the Bragg direction[5] within a cone with an angle of several γ^{-1} (γ is the relativistic factor of an electron), has a spectral linewidth of less than 10% with a total yield of about 10^{-5} photons per electron.

The resonance transition x radiation (RTXR) arising when an electron passes through a layered target[5] is stronger than the PXR, and for several hundreds of thin foils it can comprise several photons per electron. The energies of the emitted RTXR photons range up to $E_\gamma \simeq \hbar \omega_p \gamma$, where ω_p is the plasma frequency of the medium and the spectral bandwidth of the radiation is ~ 50–80%, depending on the absorbing properties of the radiator material. The RTXR photons are emitted into a cone with an angle of several
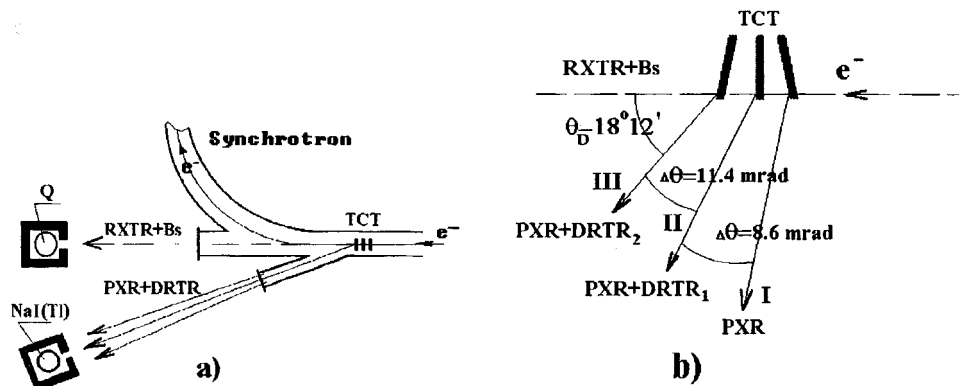
FIG. 1. a) Experimental arrangement: RXTR — resonance transition x radiation, Bs — bremsstrahlung, TCT — triple-crystal target, DRTR — diffracted transition radiation, PXR — parametric x radiation, Q — quantometer. b) Geometry of radiation generation in a triple-crystal target. I, II, and III — directions of the reflections of the radiation emitted from the first, second, and third crystals, respectively.

γ^{-1} in the direction of motion of the electrons. The form of the spectrum and the cone angle of the radiation can be varied by varying the foil thicknesses and the widths of the gaps between the foils.

According to the proposed concept, the RTXR formed in an amorphous layered structure is then diffracted by the crystallographic planes in the Bragg direction together with the PXR. However, if the target consists of a collection of mutually oriented thin crystals, then the RTXR formed by the surfaces of the crystals is also diffracted in the subsequent crystals in the Bragg direction together with the PXR. Experiments performed at the Tomsk and Tokyo synchrotrons showed that the new x-ray sources combine the positive qualities of the RTXR (high intensity) and PXR (monochromaticity, large angles of emission relative to the electron beam). In addition, it was found that the radiation yield from complex targets is much higher than the PXR yield from a crystal. The spectra and orientational dependences of the radiation from the aforementioned complex targets were measured, but the details of the photon emission from such structures were not investigated.

In the present work, on account of the special construction of the triple-crystal target, we were able to observe the formation of the total flux of coherent x radiation (PXR + DRTR) as a function of the number of plates participating in the emission (DRTR stands for diffracted resonance transition radiation).

The experimental arrangement is displayed in Fig. 1a. A 800-MeV accelerated electron beam in the Tomsk synchrotron was directed onto an inner target. The main layered crystalline target and a one-crystal target of equivalent thickness (48 μm) for measuring the "pure" PXR were secured on a goniometric head, which could be moved vertically so as to position the targets successively in the electron beam. The bremsstrahlung was detected with a Gauss quantometer, the readings of which were used to normalize the results of the measurements. The coherent radiation emitted from the crystal at the angle $\theta_D = 2\,\theta_B = 18°\,12'$ exited through the 200-μm thick beryllium window of the synchro-

tron chamber and entered the detector. The detector consisted of a NaI(Tl) γ-ray spectrometer with a 2-mm thick crystal. The energy resolution was equal to about 35% for ^{57}Co (6.4 keV line) and 16% for ^{241}Am (59.6 keV). The detection threshold was set at 7 keV. The beryllium entrance window of the detector was 40 mm in diameter and 200 μm thick. A 2-mm wide vertical slit collimator was placed in front of the detector. The target–detector distance was equal to 458 cm, including 243 cm of air.

The main target consisted of three 16-μm thick silicon crystals separated by 147-μm gaps. The crystal plates were cut so that the (220) crystallographic planes were perpendicular to their surfaces. The target was fabricated at the Toshiba Corporation and is described in detail in Ref. 7. The outer crystals of the target are disoriented relative to the central crystal by 4.3 and 5.7 mrad in different directions. Three well-separated x-ray reflections rays in the Bragg directions (see Fig. 1b), differing by twice the relative angle of disorientation of the crystals, can be obtained by passing a narrow electron beam through such a radiator at some angle to the (220) planes in the Laue geometry. The first reflection peak from the first crystal is formed as a result of PXR (we are neglecting the diffraction of the transition radiation produced at the entrance surface of this crystal). Then the second reflection peak is due to PXR from the second crystal and diffraction of the transition radiation produced at the surfaces of the first crystal. The third reflection peak, in turn, is formed by PXR from the third crystal and DRTR from the two preceding crystals. By measuring the characteristics of the reflections it is possible to draw inferences about the process in which coherent x rays are genterated by relativistic electrons passing through a complex crystal structure.

The experimental PXR spectrum obtained on an equivalent target in the Bragg orientation $\Theta_B = 0.5\Theta_D$ contains first- and second-order spectral peaks. The ratio of the outputs of the PXR photons in the energy range $E_\gamma = 29$–44 and 10–29 keV, corresponding to the second and first spectral peaks, equals 0.13. The orientational dependences (ODs) of the PXR photon yield in the indicated energy intervals were also measured on an equivalent target.

The experimental OD (dots) of the yield of PXR + DRTR photons ($E_\gamma = 10$–29 keV) from a triple-crystal target is displayed in Fig. 2. The OD obtained contains three peaks — I, II, and III, which appear when the target crystals are placed, in turn, in the Bragg positions. The three dashed curves show the partial contributions to the overall pattern of the PXR formed in each crystal. The form of these curves was obtained by analyzing the OD of the radiation measured on the equivalent target. The solid curve shows the OD of the PXR yield from a triple-crystal target as the sum of the above-mentioned partial contributions, taking into account the photoabsorption in the radiator material and the geometry of the radiator. The partial DRTR contributions (curve with dots) to the total yield of the radiation were obtained by subtracting from the experimental OD (dots) the total OD of the PXR (solid curve).

Figure 2 shows that the peaks in the OD of the partial DRTR yields from separate crystals are much narrower than for the PXR yield. Their widths equal 1.25 and 4.75 mrad, respectively. Therefore, the DRTR is a much more narrowly directed source of x rays than PXR. Furthermore, it follows from the figure that the DRTR yield at the maximum of the OD increases as the number of the crystal increases, so that the angular
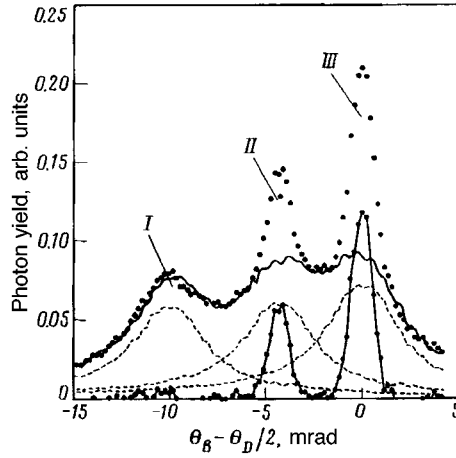
FIG. 2. Measured orientational dependence (dots) of the yield in a collimated detector of x rays generated by 800-MeV electrons in a triple-crystal target. Dashed curves — contributions to the OD due to PXR from three crystals; solid curve — sum of the PXR contributions; two peaks (solid curve with dots) — contributions due to DRTR from the first crystal (left-hand peak) and the second crystal (right-hand peak).

density of the DRTR from the third crystal is approximately 1.7 times higher than the PXR density.

According to the theory,[6] the distribution of the resonance transition x radiation is determined by the expression

$$\Theta_R = \left(\frac{4\pi\hbar c}{E_\gamma(l_1+l_2)} - \gamma^{-2} - \frac{l_1}{l_1+l_2}\left(\frac{\hbar\omega_p}{E_\gamma}\right)^2 \right)^{0.5}, \tag{1}$$

where l_1 and l_2 are, respectively, the thickness of the crystals and the width of the gaps between them. It is important to note that expression (1) implies that the angular distribution of the RTXR and therefore also the DRTR can be regulated by varying the parameters of the target, while the width of the angular distribution of the PXR is determined solely by the characteristics of the crystal:[8]

$$\triangle\Theta = ((1+\sqrt{2})^2[\gamma^{-2}+(\hbar\omega_p/E_\gamma)^2]+\langle\Theta\rangle_{ms}^2)^{0.5}, \tag{2}$$

where $\langle\Theta\rangle_{ms}^2$ is the mean-square angle of multiple scattering of the electrons in the target materials, $\hbar\omega_{p\,Si} \simeq 30$ eV.

The radiation spectra measured as the triple-crystal target is turned successively by angles corresponding to symmetric positions of the crystals are presented in Fig. 3. When the first crystal is symmetric relative to the electron beam and detector (Bragg orientation), the radiation spectrum is similar to the PXR spectrum. The ratio of the radiation yields in the second and first spectral peaks equals 0.13. When the target is placed in a position symmetric for the second crystal, this ratio becomes equal to 0.11 on account of the contribution of the DRTR, for which the proportion of photon yields in the first and
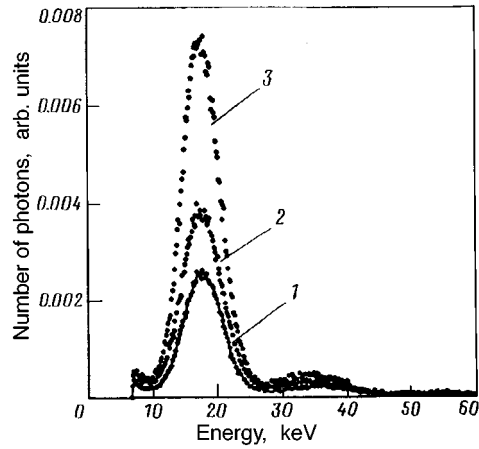
FIG. 3. Spectra of radiation emitted from a triple-crystal target at the centers of the reflections I, II, and III (curves *1*, *2*, and *3*).

second spectral intervals is different, as observed in Ref. 2. In a position which is symmetric for the third crystal, when the DRTR contribution increases, the value obtained for the ratio drops to 0.09.

In Fig. 4 the computed ODs of the PXR and DRTR yields are compared with experiment. The calculations were performed in the kinematic approximation. Theoretical models for PXR[8] and for DRTR[6] taking account of the experimental conditions were
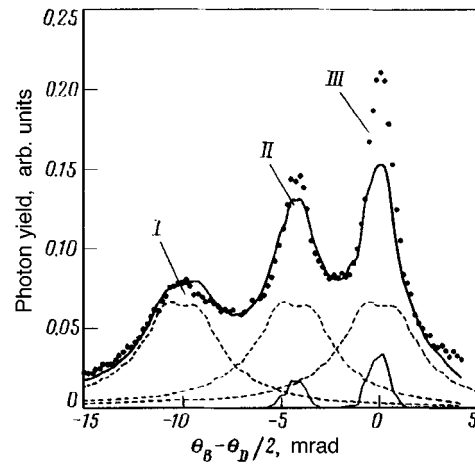
FIG. 4. Comparison of the experimental (dots) and computed orientational dependences of the PXR from three crystals (dashed curves), the DRTR from the second and third crystals (left- and right-hand peaks, denoted by the dotted curves), and the sum of the PXR and DRTR contributions from all crystals taking account of interference (solid curve).

used in the calculations. The dashed curves show the partial yields of PXR from the three crystals; the thin solid curves show the DRTR yields from the second and third crystals.

Comparing Figs. 4 and 2, it can be concluded that the computed ratio of the DRTR and PXR yields does not correspond to the ratio obtained in the experiment, and the sum of the yields does not describe the form of the experimental orientational dependence. We conjectured that the anomalously high radiation yield in the experimental peaks *2* and *3* is due to the interference of the DRTR and PXR. This interference was taken into account in a model approximation — the square of the sum of the DRTR and PXR amplitudes was calculated for the entire radiation cone, after which the geometry of the detector was taken into account. The curve obtained (thick line in Fig. 4) is in much better agreement with experiment, though the difference once again is quite large, especially for peak III. To understand the observed defect, additional investigations are probably required.

The main results of the experiment are as follows.

1. The use of a novel triple-crystal target whose crystals are slightly disoriented with respect to one another made it possible to observe the production of resonance transition x radiation diffracted by a crystal as a function of the number of interfaces separating the media participating in the generation of the RTXR.

2. The results confirm the results obtained in Refs. 2–4: When a layered structure, a source of RTXR, is positioned in front of the crystal, an effective increase in the x-ray yield is obtained at larger (Bragg) angles with respect to the electron beam than in the case of ''pure'' PXR.

3. The angular distribution of the DRTR is much narrower than that of the PXR and can be regulated by varying the parameters of the layered structure positioned in front of the crystal. As a consequence of the narrower angular distribution, the spectral DRTR peaks will be more monochromatic than the PXR peaks. Moreover, it was shown that the fraction of the contribution from the higher harmonics to the DRTR spectrum is much smaller than in the PXR spectrum.

4. Analysis of the ratios of the DRTR and PXR contributions to the formation of the orientational dependence of the radiation from a triple-crystal target shows that these components can add together synergistically. That is, the resulting radiation is not simply a sum of the DRTR and PXR, but rather it is the result of their interference. But this question requires further, more detailed, investigations.

[a]e-mail: kaplin@tsinph.tomsk.su

[1] M. Yu. Andreyashkin, V. V. Kaplin, V. N. Zabaev *et al.*, in *Proceedings of the International Symposium on Radiation by Relativistic Electrons in Periodic Structures*, RREPS-93, Tomsk, Russia, NPI TPU, 1993, p. 86.
[2] M. Yu. Andreyashkin, V. V. Kaplin, E. I. Rozum *et al.*, in *Proceedings of the 2nd International Symposium on Radiation of Relativistic Electrons in Periodic STructures*, RREPS-95, Tomsk, Russia, Cambridge International Science Publishers, 1996, p. 36.

[3] M. Yu. Andreyashkin, V. N. Zabaev, V. V. Kaplin *et al.*, JETP Lett. **62**, 791 (1995).

[4] K. Aramitsu, I. Endo, K. Goto *et al.*, Hiroshima University Preprint HUPD-9513 (1995).

[5] M. L. Ter-Mikaelyan, *High-Energy Electromagnetic Processes in Condensed Media*, Wiley-Interscience, New York, 1972 [Russian original, Arm. SSR Academy of Sciences, Erevan, 1969].

[6] G. M. Garibyan and Yan Shi, *X-Ray Transition Radiation* [in Russian], Arm. SSR Academy of Sciences, Erevan, 1983.

[7] K. Nakayama, M. Sekimura, I. Yanase *et al.*, in *Proceedings of the 2nd International Symposium on Radiation of Relativistic Electrons in Periodic Structures*, RREPS-95, Tomsk, Russia, Cambridge International Science Publishers, 1996, p. 240.

[8] I. D. Feranchuk and A. V. Ivashin, J. Phys. (France) **46**, 1981 (1985).

Translated by M. E. Alferieff

Magnetic moment of type-II superconductors near the critical field H_{c2} and the formation of metastable states for Ginzburg–Landau parameter $\kappa < 1$

Yu. N. Ovchinnikov

L. D. Landau Institute of Theoretical Physics, Russian Academy of Sciences, 117334 Moscow, Russia

The magnetic induction in cylindrical superconductor samples in magnetic fields close to H_{c2} is found. It is shown that vortex-type metastable states exist in a quite wide range of values of the Ginzburg–Landau parameter $\kappa < 1$ corresponding to type-I superconductors. © *1997 American Institute of Physics.* [S0021-3640(97)00808-6]

PACS numbers: 74.25.Ha, 74.60.Ec, 74.20.De

1. INTRODUCTION

The mixed state of type-II superconductors was investigated in Ref. 1. However, in calculating the magnetic field the author made an incorrect assumption, which, as it turns out, is nonetheless justified provided that the Ginzburg–Landau parameter κ is greater than and not close to 1. As a result, it was found that the mixed state does not exist for $\kappa < 1$. Actually, however, a mixed state can be realized in a wide range $\kappa < 1$, corresponding to type-I superconductors, and the structure of the vortex lattice itself depends on the value of κ.

2. SOLUTION OF THE GINZBURG-LANDAU EQUATION NEAR THE CRITICAL FIELD H_{c2}

The free energy F_S of the superconducting state in an external magnetic field H_0 can be represented in the form[2]

$$F_S - F_N = \nu \int d^2\mathbf{r} \left\{ -(1 - T/T_c)|\Delta|^2 + \frac{\pi D}{8 T_c}|\partial_-\Delta|^2 + \frac{7\zeta(3)}{16\pi^2 T_c^2}|\Delta|^4 \right\}$$

$$+ \frac{1}{8\pi} \int d^3\mathbf{r}((\nabla\mathbf{A})^2 - 2\mathbf{H}_0 \cdot (\nabla \times \mathbf{A}) + \mathbf{H}_0^2), \tag{1}$$

where $\mathbf{A}$ is the vector potential, $\partial_- = \partial/\partial\mathbf{r} - 2ie\mathbf{A}$, and $\nu = mp_0/2\pi^2$ is the density of states at the Fermi surface. The coefficient D depends on the electron transport mean free path l_{tr} and equals

$$D = D_{\text{dif}} \cdot \eta; \quad D_{\text{dif}} = \frac{v l_{\text{tr}}}{3}; \quad \eta = 1 - \frac{8 T \tau_{\text{tr}}}{\pi}\left(\psi\left(1/2 + \frac{1}{4\pi T \tau_{\text{tr}}}\right) - \psi(1/2)\right),$$

$$l_{\text{tr}} = v \cdot \tau_{\text{tr}}, \tag{2}$$

where v is the velocity of electrons at the Fermi surface and $\psi(x)$ is Euler's ψ function. Varying the free energy (1) with respect to Δ and $\mathbf{A}$, we obtain the Ginzburg–Landau equations

$$\frac{\pi D}{8T_c}\partial_-^2\Delta+(1-T/T_c)\Delta-\frac{7\zeta(3)}{8\pi^2 T_c}|\Delta|^2\Delta=0$$

$$\frac{1}{4\pi}\nabla\times\nabla\times\mathbf{A}=j, \quad j=\frac{i\pi e\nu D}{4T_c}(\Delta\partial_+\Delta^*-\Delta^*\partial_-\Delta). \tag{3}$$

In a magnetic field

$$H=H_{c2}=\frac{4T_c}{\pi e D}(1-T/T_c), \tag{4}$$

the linearized equation (3) has a solution of the form[2]

$$\Delta=\exp(2ieHx_1 y-eH(x-x_1)^2), \tag{5}$$

for arbitrary x_1. The gauge

$$A=(0,\,Hx,\,0) \tag{6}$$

was used in obtaining Eq. (5). We shall seek solutions of Eq. (3) for $H_0 < H_{c2}$ such that the physical quantities $|\Delta|^2$, $H(x,y)$, and j are periodic functions of the coordinates x and y. Let $\mathbf{a}_{1,2}$ be unit-cell vectors, i.e.,

$$|\Delta(\mathbf{r}+N\mathbf{a}_1+M\mathbf{a}_2)|^2=|\Delta(\mathbf{r})|^2. \tag{7}$$

From the condition that the current density be periodic we find

$$\oint_\Gamma\left(\frac{\partial\chi}{\partial\mathbf{r}}-2e\mathbf{A}\right)\cdot d\mathbf{l}=0, \tag{8}$$

where Γ is a closed contour drawn along the edge of the unit cell and χ is the phase of the order parameter. Since the order parameter is a single-valued function of the coordinates, Eq. (8) leads to the condition of quantization of the magnetic flux ϕ through the unit cell:

$$\phi=\frac{\pi}{e}N, \quad N=1,2,\ldots\ . \tag{9}$$

This exact relation greatly simplifies the search for a solution of the system of equations (3).

We seek in the following form a solution of Eqs. (3) in a magnetic field $H_0 < H_{c2}$:

$$\mathbf{A}=(0,\,Bx,\,0)+\mathbf{A}_1+\mathbf{A}_2+\ldots, \quad \Delta=\Delta_0+\Delta_1+\Delta_2+\ldots,$$

$$\Delta_0=\sum_N C_N\exp(2ieBNx_1 y-eB(x-Nx_1)^2), \tag{10}$$

where B is the magnetic induction inside the superconductor ($B=\langle H(\mathbf{r})\rangle$) and the vectors $\mathbf{A}_k$ possess two nonzero components (1, 2) and are proportional to $(H_{c2}-B)^k$. The

quantities $|\Delta_k|^2 \sim (H_{c2}-B)^{2k+1}$ and $C_N^2 \sim (H_{c2}-B)$. In what follows, we shall employ the gauge $\mathrm{div}\mathbf{A}=0$. In this gauge all quantities $\mathbf{A}_k$ are periodic functions of the coordinates. In the gauge employed in Ref. 1 the quantities A_k are increasing functions of x, which presents additional difficulties in investigations of the system of equations (3).

It should be expected that $|\mathbf{a}_1|=|\mathbf{a}_2|$ in an isotropic superconductor. Let $\mathbf{k}_{1,2}$ be the elementary reciprocal-lattice vectors. The order parameter $|\Delta|^2$ in this case can be represented as

$$|\Delta|^2 = \sum_{N,M=-\infty}^{\infty} C_{NM} \exp\left(i(N\mathbf{k}_1+M\mathbf{k}_2)\cdot\mathbf{r}\right). \tag{11}$$

For a triangular lattice with one flux quantum per cell we find

$$\mathbf{k}_1 = \frac{2\pi}{\sqrt{3}x_1}(0,1); \quad \mathbf{k}_2 = \frac{\pi}{\sqrt{3}x_1}(\sqrt{3},-1),$$

$$2\sqrt{3}eBx_1^2 = \pi; \quad C_N = C_0 \exp\left(-\frac{i\pi}{2}N^2\right),$$

$$C_{N,M} = C_0^2 3^{1/4} \exp\left(-i\pi NM - \frac{\pi}{\sqrt{3}}(N^2+M^2-NM)\right). \tag{12}$$

For a square lattice with one flux quantum per cell we obtain

$$\mathbf{k}_1 = \frac{2\pi}{x_1}(0,1); \quad \mathbf{k}_2 = \frac{2\pi}{x_1}(1,0),$$

$$eHx_1^2 = \pi; \quad C_{N+1} = C_N = C_0,$$

$$C_{N,M} = \frac{C_0^2}{\sqrt{2}}(-)^{MN} \exp\left(-\frac{\pi}{2}(N^2+M^2)\right). \tag{13}$$

We also give an expression for the quantities characterizing a triangular lattice with two flux quanta per cell:

$$\mathbf{k}_1 = \frac{2\pi}{\sqrt{3}x_1}(0,1); \quad \mathbf{k}_2 = \frac{\pi}{\sqrt{3}x_1}(\sqrt{3},-1),$$

$$\sqrt{3}eHx_1^2 = \pi; \quad C_{N+1} = C_N = C_0,$$

$$C_{N,2K+1} = 0; \quad C_{N,2K} = \frac{C_0^2 3^{1/4}}{\sqrt{2}} \exp\left(i\pi K(N-K) - \frac{\pi}{2\sqrt{3}}(N^2+4K^2-2KN)\right). \tag{14}$$

For the order parameter Δ_0 determined by expression (10) the current density j_1 can be expressed in terms of the square modulus $|\Delta_0|^2$ as

$$j_1 = -\frac{\pi e\nu D}{4T_c}\left(\frac{\partial}{\partial y};-\frac{\partial}{\partial x}\right)|\Delta_0|^2, \tag{15}$$

and therefore Eq. (3) for the magnetic field H_1 assumes the form[1]

$$\left(\frac{\partial}{\partial y}; -\frac{\partial}{\partial x}\right) H_1(\mathbf{r}) = -\frac{\pi^2 e \nu D}{T_c} \left(\frac{\partial}{\partial y}; -\frac{\partial}{\partial x}\right) |\Delta_0|^2. \tag{16}$$

It follows from Eq. (16) that the magnetic field $H_1(r)$ inside the superconductor can be represented as

$$H_1(\mathbf{r}) = -\frac{\pi^2 e \nu D}{T_c} (|\Delta_0|^2 - \langle |\Delta_0|^2 \rangle), \tag{17}$$

since the vector potential $\mathbf{A}_1$ ($\nabla \times \mathbf{A}_1 = \mathbf{H}_1$) should remain bounded.

In contrast to Ref. 1, we shall assume that the induction B cannot be reconstructed from Eq. (16), since in the thermodynamic limit the system of equations (3) has an enormous number of solutions $\sim e H R^2 \gg 1$ (R is the characteristic transverse size of the cylinder). The free parameter is the area of the unit cell (magnetic induction B). Therefore, the induction B should be determined from the condition that the free energy (1) has a minimum with respect to B for a prescribed value of the external magnetic field H_0:

$$\frac{\partial (F_S - F_N)}{\partial B} = 0. \tag{18}$$

Ultimately, the impossibility of determining the magnetic induction B from Eq. (3) for the vector potential is due to the flow of surface currents. The total magnetic moment $\mathbf{M}$ is produced by both the volume (lattice) and surface currents. The volume current is determined by the structure of the lattice and can be easily found. The contribution of the surface currents leads to the formation of a large number of metastable states. The condition (18) selects from among them the state that gives a minimum of the free energy.

It follows from Eqs. (1) and (10) that the free energy density $(F_S - F_N)/V$ can be represented as a power series in $(H_{c2} - B)$

$$(F_S - F_N)/V = \frac{1}{8\pi} \{(B - H_0)^2 + P_1 (H_{c2} - B)^2 + P_2 (H_{c2} - B)^3 / H_{c2} + \ldots \}. \tag{19}$$

The coefficients P_k in Eq. (19) are determined by the type of vortex lattice and the value of the parameter κ. To determine the coefficient C_0, we shall employ the method of eliminating secular terms in Eq. (3).

The condition $|\Delta_1| \ll |\Delta_0|$ can be satisfied, provided that the nonuniform part in the linearized equation (3) is orthogonal to Δ_0 (see also Ref. 1). This condition yields the following equation for C_0:

$$\frac{\pi e D}{4 T_c} (H_{c2} - B) \langle |\Delta_0|^2 \rangle - \frac{7 \xi_{(3)}}{8 \pi^2 T_c^2} \langle |\Delta_0|^4 \rangle + \frac{1}{\nu} (\mathbf{A}_1 \cdot \mathbf{j}_1) = 0, \tag{20}$$

where the vector potential $\mathbf{A}_1$ is determined by the expression

$$\nabla \times \mathbf{A}_1 = H_1 \quad \text{or} \quad -\frac{\partial^2 \mathbf{A}_1}{\partial r^2} = 4\pi \mathbf{j}_1. \tag{21}$$

In Eq. (21) $\mathbf{A}_1$ is a periodic function of the coordinates, and the magnetic field H_1 and the current density $\mathbf{j}_1$ are determined by Eqs. (17) and (15).

Using Eqs. (15), (16), and (21), we find

$$\langle \mathbf{A}_1 \cdot \mathbf{j}_1 \rangle = \frac{1}{4\pi} \langle H_1^2 \rangle. \tag{22}$$

From Eqs. (17), (20), and (22) we find the following expression for $\langle |\Delta_0|^2 \rangle$

$$\langle |\Delta_0|^2 \rangle = \frac{2\pi^3 eDT_c}{7\zeta(3)} \frac{H_{c2} - B}{\beta - (\beta - 1)/\kappa^2}, \tag{23}$$

where κ is the Ginzburg–Landau parameter and β is determined by the relation

$$\beta = \frac{\langle |\Delta_0|^4 \rangle}{\langle |\Delta_0|^2 \rangle^2}; \quad \kappa = \frac{1}{\pi^2 eD} \left(\frac{7\zeta(3)}{2\pi\nu} \right)^{1/2}, \tag{24}$$

where $\zeta(x)$ is the Riemann ζ function.

The values of the coefficient β are given below for three types of lattices. These values can be trivially found using Eqs. (12), (13), and (14):

$\beta = 1.15952$ — triangular lattice with one flux quantum;

$\beta = 1.18034$ — square lattice with one flux quantum;

$\beta = 1.33897$ — triangular lattice with two flux quanta.

Now we can find the free energy F_S in the vortex state. From Eqs. (1), (22), and (23) we find

$$(F_S - F_N)/V = \frac{1}{8\pi}(B - H_0)^2 - \frac{(H_{c2} - B)^2}{8\pi\kappa^2 \left(\beta - \dfrac{\beta - 1}{\kappa^2} \right)} + P_2 \frac{(H_{c2} - B)^3}{8\pi H_{c2}} + \dots . \tag{25}$$

The coefficient P_2 in Eq. (25) is of the order of 1. We shall find its dependence on κ and the structure of the lattice elsewhere.

We also note that if the parameter $\kappa > 1$ and not close to 1, then near H_{c2} the last term in Eq. (25) is small and can be dropped. In this case we find from Eq. (18)

$$H_0 - B = \frac{H_{c2} - B}{\beta\kappa^2(1 - 1/\kappa^2)}. \tag{26}$$

Expression (26) is identical to Abrikosov's result.[1] However, as $\kappa \to 1$ the region of applicability of formula (26) becomes narrower. For $\kappa < 1$ the solution of Eq. (17) by Abrikosov's method corresponds to a maximum and not a minimum of the free energy (1). To obtain the minimum the third term in Eq. (25) must be taken into account. Let

$$Z = H_{c2} - B. \tag{27}$$

We find from Eqs. (18) and (25)

$$Z = -\frac{H_{c2}\beta(\kappa^2-1)}{3P_2(1+\beta(\kappa^2-1))} + \sqrt{\left(\frac{H_{c2}\beta(\kappa^2-1)}{3P_2(1+\beta(\kappa^2-1))}\right)^2 + \frac{2H_{c2}(H_{c2}-H_0)}{3P_2}}. \quad (28)$$

We note that the correction to the free energy given by Eqs. (25) and (28) is always negative at the point of the minimum. Similarly, the free energy (25) is also negative on the entire path of B from H_0 up to the point $B_{\min}$. This means that ''supercooling'' — a delay with a transition to the superconducting state ($\kappa < 1$) — can occur only up to the point $H_{c2} < H_c$ (H_c is the thermodynamic critical field).

The expression for the free energy given by formulas (25) and (28) exhibits a nontrivial dependence on the parameters κ and β. Therefore, it is necessary to calculate P_2 in order to determine the type of lattice near the point $\kappa = 1$.

[1] A. A. Abrikosov, Zh. Éksp. Teor. Fiz. **32**, 1442 (1957) [Sov. Phys. JETP **5**, 1174 (1957)].
[2] V. L. Ginzburg and L. D. Landau, Zh. Éksp. Teor. Fiz. **20**, 1064 (1950).
[3] R. D. Parks (ed.), *Superconductivity,* Dekker, New York, 1969.
[4] P.-G. de Gennes, *Superconductivity of Metals and Alloys,* Benjamin, New York, 1966.

Translated by M. E. Alferieff

Effect of impurities on the low-temperature behavior of the specific heat of anisotropic superconductors in a mixed state

Yu. S. Barash and A. A. Svidzinskiĭ

P. N. Lebedev Physics Institute, Russian Academy of Sciences, 117924 Moscow, Russia

V. P. Mineev

L. D. Landau Institute of Theoretical Physics, Russian Academy of Sciences, 142432 Chernogolovka, Moscow District, Russia

In the presence of zeros of the order parameter in an anisotropic super-conductor, the combined effect of a magnetic field and impurities leads to two different limiting magnetic-field dependences of the specific heat. These dependences are studied both for Born scatterers and in the unitary limit for several specific examples of anisotropic pairing. A estimate is given for the crossover field. © *1997 American Institute of Physics.* [S0021-3640(97)00908-0]

PACS numbers: 74.60.Ec, 74.25.Bt, 74.62.Dh

The experimental study of the thermodynamic and transport properties of anisotropic superconductors in magnetic fields yields important information about the existence and locations of zeros of the order parameter on the Fermi surface, which is essential for determining the symmetry of the superconducting state.[1–3]

In the case of an anisotropic superconductor in a magnetic field the quasiparticle density of states at the Fermi surface is nonzero for momentum directions near the zeros of the order parameter.[4–8] In a clean superconductor, in the case of a line of simple zeros of the order parameter the density of states in the mixed state is proportional to $\sqrt{H}$, which leads to the appearance of a characteristic magnetic-field-dependent term $C \propto T\sqrt{H/H_{c2}}$ in the specific heat.[5] A dependence of this kind was recently observed experimentally in YBCO.[1,2]

Impurities can also result in a nonzero density of states near the zeros of the order parameter on the Fermi surface.[9–12] For this reason, it is natural to expect competition between the effect of impurities and a magnetic field on the behavior of the density of states. The combined effect of a magnetic field and impurities on superconductivity in isotropic superconductors was studied in Ref. 13. The present letter examines the effect of impurities on the low-temperature behavior of the specific heat of superconductors with anisotropic pairing in a mixed state. As will be shown below, in the presence of zeros of the order parameter even a comparatively small amount of impurities can have a large effect on the magnetic-field dependence of the thermodynamic characteristics of a superconductor.

We shall find the quasiparticle density of states at low temperatures for the vortex phase in a field $H \ll H_{c2}$, parallel to a high-symmetry crystallographic axis, at distances $\xi_0 \ll r \ll R$ from the axis of the vortex, where $R \sim \xi_0 \sqrt{H_{c2}/H}$ is the distance between the vortices (for the temperatures considered we set $\xi(T) \simeq \xi_0$). In this range of distances the modulus of the impurity-averaged order parameter is constant in space, to a high degree of accuracy, and the magnetic-field-induced superfluid velocity varies quite slowly as a function of the distance from a vortex. This makes it possible to use the well-known expressions for the impurity-renormalized quasiparticle energy $\widetilde{\omega}$ and order parameter $\widetilde{\Delta}$ for a homogeneous superconductor. For isotropic impurity scattering, we have in the Born approximation

$$\widetilde{\omega} = \omega + \frac{i}{2\tau} g(\omega), \quad g(\omega) = 2i\tau\Sigma(\omega) = \left\langle \frac{\widetilde{\omega} - \mathbf{v}_s \cdot \mathbf{k}_f}{\sqrt{(\widetilde{\omega} - \mathbf{v}_s \cdot \mathbf{k}_f)^2 - |\widetilde{\Delta}(\mathbf{k}_f, \omega)|^2}} \right\rangle_{\mathbf{k}_f}, \qquad (1)$$

$$\widetilde{\Delta}(\mathbf{k}_f, \omega) = \Delta(\mathbf{k}_f) + \frac{i}{2\tau} \left\langle \frac{\widetilde{\Delta}(\mathbf{k}_f', \omega)}{\sqrt{(\widetilde{\omega} - \mathbf{v}_s \cdot \mathbf{k}_f')^2 - |\widetilde{\Delta}(\mathbf{k}_f', \omega)|^2}} \right\rangle_{\mathbf{k}_f'}, \qquad (2)$$

where τ is the relaxation time in the normal metal and $\langle \ldots \rangle_{\mathbf{k}_f}$ denotes an average over all orientations of the Fermi momentum $\mathbf{k}_f$.

In Eqs. (1) and (2) the square root is defined so that the real part of the expression being averaged in Eq. (1) is always nonnegative (specifically, Re $g(\omega) \geq 0$). This requirement determines the rule for selecting the regular branch of the square root in expressions (1) and (2).

The quasiparticle density of states is $N_S(\omega) = N(0)\mathrm{Re}\, g(\omega)$, where $N(0)$ is the density of states at the Fermi surface in a normal metal. The quasiparticle density of states at the Fermi surface is important for low-temperature thermodynamic properties of a superconductor. For this reason, we set $\omega = 0$ everywhere. Then Eqs. (1) become

$$\Omega = \frac{g(\Omega)}{2\tau}, \quad g(\Omega) = \left\langle \frac{i\Omega - \mathbf{v}_s \cdot \mathbf{k}_f}{\sqrt{(i\Omega - \mathbf{v}_s \cdot \mathbf{k}_f)^2 - |\widetilde{\Delta}(\mathbf{k}_f, \Omega)|^2}} \right\rangle_{\mathbf{k}_f}, \qquad (3)$$

where $i\Omega = \widetilde{\omega}(\omega = 0)$, $\Omega \geq 0$, $g(\Omega) \equiv g(\omega = 0)$, and $\widetilde{\Delta}(\mathbf{k}_f, \Omega) \equiv \widetilde{\Delta}(\mathbf{k}_f, \omega = 0)$.

It follows from the conditions Re $g(\Omega) \geq 0$ and $\Omega \geq 0$ that the corresponding branch with a cut in the complex z plane along the positive abscissa must be chosen for the function $\sqrt{z}$ in the denominator in Eq. (3). Then the imaginary part of the function $\sqrt{z}$ is always positive. The sign of the real part of this function is the same as the sign of Im $z = -2(\mathbf{v}_s \cdot \mathbf{k}_f)\Omega$. (specifically, the real part of $\sqrt{z}$ is an odd function of $(\mathbf{v}_s \cdot \mathbf{k}_f)$). Hence it follows that the imaginary part of the expression being averaged in Eq. (3) vanishes after being averaged over all directions of $\mathbf{k}_f$. As a result, $g(\Omega)$ is a real function taking on nonnegative values.

Next, for this choice of the regular branch of $\sqrt{z}$ and with the condition Re $z < 0$

$$\Omega^2 + |\widetilde{\Delta}(\mathbf{k}_f, \Omega)|^2 > (\mathbf{v}_s \cdot \mathbf{k}_f)^2, \qquad (4)$$

the real part of the function being averaged in Eq. (3) is an analytic, even function of $(\mathbf{v}_s \cdot \mathbf{k}_f)$. As a result, the integration over the directions of the Fermi momentum for which the condition (4) holds gives a contribution to $g(\Omega)$ for which the first term in its expansion in powers of the superfluid velocity is proportional to $\mathbf{v}_s^2$. In the opposite case, $\mathrm{Re}\, z > 0$, $\sqrt{z}$ has different signs on the two edges of the cut and the function being averaged in Eq. (3) is found in the clean limit to depend on $|\mathbf{v}_s \cdot \mathbf{k}_f|$. Therefore $g(\Omega)$ acquires a contribution proportional to the modulus of the superfluid velocity. It is important that in contrast to expression (1) the numerator in Eq. (2) does not have a term which is linear in $\mathbf{v}_s$. As a result, terms linear in $\mathbf{v}_s$ do not arise in the description of the combined effect of impurities and a magnetic field on $\widetilde{\Delta}(\mathbf{k}_f, \Omega)$.

If the order parameter of an anisotropic superconductor possesses zeros on the Fermi surface (or is anomalously small in some regions of the Fermi surface), then a narrow region of integration over momentum directions near the zeros gives the main contribution to the function $g(\omega)$, at least when $\Omega, \mathbf{v}_s \cdot \mathbf{k}_f \ll \widetilde{\Delta}_0$, where $\widetilde{\Delta}_0 = \max_{S_f} |\widetilde{\Delta}(\mathbf{k}_f, \Omega)|$. When the order parameter possesses zeros, the condition (4) approximately reduces to the inequality $\Omega > |\mathbf{v}_s \cdot \mathbf{k}_f|$, which breaks down for small Ω, i.e., sufficiently low impurity densities. Therefore two qualitatively different types of behavior of the quasiparticle density of states as a function of the magnetic field and impurity density can be realized. In the limiting case $\Omega \gg \mathbf{v}_s \cdot \mathbf{k}_f$ the first term in the expansion of the density of states is proportional to $\mathbf{v}_s^2$, while the term linear in $\mathbf{v}_s$ dominates if $\Omega \ll \mathbf{v}_s \cdot \mathbf{k}_f$.

Let us consider a superconducting phase in which the order parameter has a line of zeros on the equator of a ''spherical'' Fermi surface, and near this line

$$|\Delta(\mathbf{k}_f)| = \Delta_0 |\theta - \pi/2|. \tag{5}$$

Furthermore, let the order parameter change sign on reflection in the equatorial plane: $\Delta(\pi - \theta) = -\Delta(\theta)$. These conditions are satisfied, for example, by the polar phase $\Delta(\mathbf{k}_f) = \Delta_0 \cos\theta$ and the superconducting phases $(1, i)$ for E_{1g} and E_{2u} pairing in a hexagonal superconductor. The last two phases are often used[14,15] to explain the properties of the heavy-fermion superconductor UPt$_3$. For $\Omega, \mathbf{v}_s \cdot \mathbf{k}_f \ll \Delta_0$ the contribution from a narrow region near such a line of zeros to the quantities under study dominates and makes it possible to describe analytically, to logarithmic accuracy, the behavior of the density of states in explicit form, if the magnetic field is oriented along an axis of high symmetry. In this case there is no impurity renormalization of the order parameter.

Taking into account only the contribution to $g(\Omega)$ from a narrow region near the line of zeros of the order parameter, we substitute expression (5) into Eq. (3) and we confine the integration over orientations of the momentum on the Fermi surface to integration over $\cos\theta$ from zero to some value A of the order of 1. This is justified if $\Omega, \mathbf{v}_s \cdot \mathbf{k}_f \ll \Delta_0$. As a result, we obtain

$$g(\Omega) = \frac{\Omega}{\Delta_0}\left[\sqrt{1 + \left(\frac{\mathbf{v}_s \cdot \mathbf{k}_f}{\Omega}\right)^2} - 1 \right] + \frac{\Omega}{\Delta_0} \ln\left\{ \frac{4A\Delta_0}{\Omega[\sqrt{1 + (\mathbf{v}_s \cdot \mathbf{k}_f/\Omega)^2} + 1]} \right\}. \tag{6}$$

In the limiting case of no magnetic field there is no need to cut off the integration over the angle θ. Since the coefficient A is of the order of 1 and appears only in the argument of the logarithmic function, we can see that the approximation made is quite accurate.

To take impurity scattering into account beyond the Born approximation, the relation (6) must be studied together with the following equation (see, for example, Refs. 12 and 6):

$$\Omega = \Gamma \frac{g(\Omega)}{\cos^2 \delta_0 + g^2(\Omega)\sin^2 \delta_0}, \tag{7}$$

where δ_0 is the phase of impurity scattering in a normal metal, and $\Gamma = \Gamma_u \sin^2 \delta_0$. In the Born approximation we have $\Gamma = 1/2\tau$, and in the unitary limit $\Gamma = \Gamma_u = n_{\mathrm{imp}}/\pi N(0)$.

In a ''dirty'' superconductor ($\Omega \gg \mathbf{v}_s \cdot \mathbf{k}_f$) we find from Eq. (6)

$$g(\Omega) \approx \frac{\Omega}{\Delta_0}\ln\left(\frac{2A\Delta_0}{\Omega}\right) + \frac{(\mathbf{v}_s \cdot \mathbf{k}_f^2)}{4\Delta_0 \Omega}, \tag{8}$$

while for sufficiently high purity $\Omega \ll \mathbf{v}_s \cdot \mathbf{k}_f$ we have

$$g(\Omega) \approx \frac{\mathbf{v}_s \cdot k_f}{\Delta_0} + \frac{\Omega}{\Delta_0}\ln\left(\frac{4A\Delta_0}{\mathbf{v}_s \cdot k_f e}\right). \tag{9}$$

From Eqs. (7) and (8) we find in the Born approximation ($\delta_0 \ll 1$) for the density of states in a ''dirty'' superconductor

$$N_S(\mathbf{v}_s) = N(0)\mathrm{Re}\ g(\Omega) \approx N(0)2\tau\Omega \approx 4AN(0)\tau\Delta_0 e^{-2\tau\Delta_0}\left(1 + \frac{(\mathbf{v}_s \cdot \mathbf{k}_f)^2}{16\Delta_0^2 e^{-4\tau\Delta_0}}\right), \quad (10)$$

and in the unitary limit ($\delta_0 \to \pi/2$)

$$N_S(\mathbf{v}_s) \approx N_{su}(\mathbf{v}_s=0)\left(1 + \frac{1}{8\Gamma_u\Delta_0}(\mathbf{v}_s \cdot k_f)^2\right). \tag{11}$$

Here $N_{su}(\mathbf{v}_s=0)$ is the density of states in the unitary limit in the absence of a magnetic field. Actually, this quantity is nonzero for any arrangement of the line of zeros (not only along the equator) on the Fermi surface.[11,12]

In a ''clean'' superconductor ($\Omega \ll \mathbf{v}_s \cdot \mathbf{k}_f$), we find from Eq. (9) in the Born approximation

$$N_S(\mathbf{v}_s) = N(0)\mathrm{Re}\ g(\Omega) \approx N(0)2\tau\Omega \approx N(0)\frac{\mathbf{v}_s \cdot \mathbf{k}_f}{\Delta_0}\left[1 + \frac{1}{2\tau\Delta_0}\ln\left(\frac{4A\Delta_0}{\mathbf{v}_s \cdot \mathbf{k}_f e}\right)\right], \tag{12}$$

while in the unitary limit we have

$$N_S(\mathbf{v}_s) = N(0)\mathrm{Re}\ g(\Omega) \approx \frac{N(0)\Gamma_u}{\Omega} \approx N(0)\frac{\mathbf{v}_s \cdot \mathbf{k}_f}{\Delta_0}\left[1 + \frac{\Gamma_u\Delta_0}{(\mathbf{v}_s \cdot \mathbf{k}_f)^2}\ln\left(\frac{4A\Delta_0}{\mathbf{v}_s \cdot \mathbf{k}_f e}\right)\right]. \tag{13}$$

The function $N_s(\mathbf{v}_s)$ for the polar phase $\Delta(\mathbf{k}_f) = \Delta_0\cos\theta$ and the superconducting phases (1,i) for E_{1g} and E_{2u} pairing in a hexagonal superconductor is constructed in Fig. 1. The functions $|\Delta(\mathbf{k}_f)| = \Delta_0\cos\theta\sin\theta$ and $|\Delta(\mathbf{k}_f)| = \Delta_0\cos\theta\sin^2\theta$, respectively, were chosen as the basis functions in the last two cases. The three examples under discussion were studied both in the case when the Born approximation is applicable and in the case when scattering by impurities must be described in the unitary limit (for $\Gamma_u = 0.01\Delta_0$ and $\Gamma_u = 0.1\Delta_0$). In the scale employed in Fig. 1, the ''dirty'' limit $\Omega \gg \mathbf{v}_s \cdot \mathbf{k}_f$ in the Born
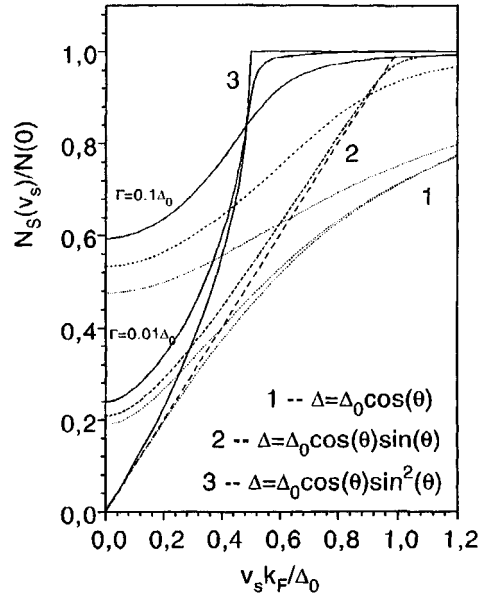
FIG. 1. $N_S(v_s)$ for the polar phase (dotted line) and the phases (1,i) E_{1g} (dashed line) and E_{1u} (solid line) in a hexagonal superconductor. The three families of curves from bottom to top correspond to Born scattering and the unitary limit with $\Gamma = 0.01\Delta_0$ and $\Gamma = 0.1\Delta_0$.

approximation is realized for indistinguishably small values of $\mathbf{v}_s$ (see also Eq. (10), where we can set approximately, for example, $\tau\Delta_0 \simeq 5$). The function $N_s(\mathbf{v}_s)$ in the Born approximation reflects, to within this accuracy, only the behavior of a "clean" superconductor. In agreement with Eq. (12), in the Born approximation with sufficiently small values of $\mathbf{v}_s \cdot \mathbf{k}_f/\Delta_0$ we have $N_S(\mathbf{v}_s) = N(0)\mathbf{v}_s \cdot \mathbf{k}_f/\Delta_0$ for all three types of pairing. As the values of $\mathbf{v}_s \cdot \mathbf{k}_f/\Delta_0$ increase, the analytical results obtained above become inapplicable even for the polar phase, since under these conditions a wide region of momentum directions, and not only a narrow interval of these directions near the line of zeros, now contributes to the formation of the density of states. For E_{1g} and E_{2u} pairings, as $\mathbf{v}_s \cdot \mathbf{k}_f/\Delta_0$ increases, the contribution of the zeros of the order parameter which are located at the poles of the Fermi surface begin to make a very large contribution to the density of states. This contribution increases the density of states compared with the case of a polar phase, where there are no such points. The density of states in the presence of second-order zeros is higher than in the case of first-order zeros. These factors determine the relative positions of the curves under discussion. As one can see from Fig. 1 and as a direct calculation confirms, the density of states in the Born approximation in a "clean" superconductor with the order parameter $|\Delta(\mathbf{k}_f)| = \Delta_0 \cos\theta \sin\theta$ is a linear function of $\mathbf{v}_s$ $(N_S(\mathbf{v}_s)/N(0) = \mathbf{v}_s \cdot \mathbf{k}_f/\Delta_0)$ all the way up to values $\mathbf{v}_s \cdot \mathbf{k}_f/\Delta_0 = 1$, where the derivative of N_S changes abruptly to zero. In the presence of scattering in the unitary limit this dependence changes appreciably with increasing impurity density as a result of the high value of $N_{su}(0)$ ($\approx 0.21N(0)$ for $\Gamma_u = 0.01\Delta_0$ and $\approx 0.53N(0)$ for $\Gamma_u = 0.1\Delta_0$) and the smearing of the jump in the derivative.
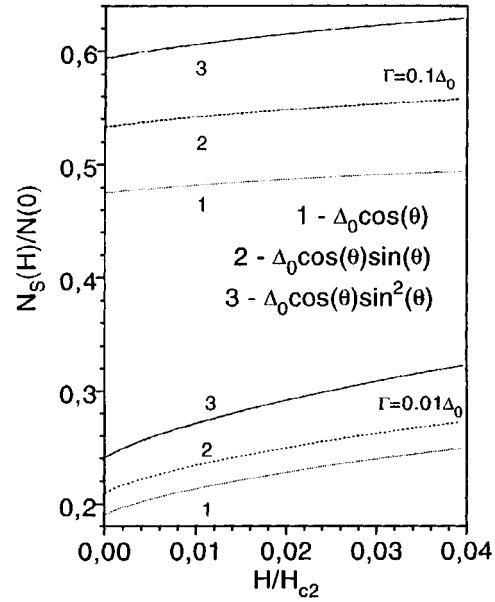
FIG. 2. $N_S(H)$ for superconducting phases in a hexagonal superconductor in the unitary limit for $\Gamma = 0.01\Delta_0$ and $\Gamma = 0.1\Delta_0$.

Spatial averaging of the main term $N(0)\mathbf{v}_s \cdot \mathbf{k}_f / \Delta_0$, describing the local density of states ($\mathbf{v}_s(r) = 1/2mr$) in the case of quite clean superconductors, over the vortex phase ($\xi_0 \leqslant r \ll R$) gives, as is well known, the expression $N_S(H) = KN(0)\sqrt{H/H_{c2}}$, where the coefficient K is of the order of 1 (this coefficient is calculated in Ref. 16). This behavior of the average density of states $N_S(H)$ occurs, generally speaking, in fields $H^* \ll H \ll H_{c2}$, where H^* is the crossover field. Under the condition $H < H^*$, impurities play a large role in the formation of the average density of states. On averaging the density of states over the vortex phase in a ''dirty'' superconductor in the unitary limit (11) we find

$$N_S(H) = N_{su}(0)\left(1 + D\frac{H}{H_{c2}}\ln\left(\frac{H_{c2}}{H}\right)\right), \tag{14}$$

where $D = \alpha\Delta_0/32\Gamma_u$ (α is a coefficient of the order of 1). We have for the low-temperature specific heat $C/T \propto N_S(H) + BN(0)H/H_{c2}$. The last term is due to the contribution of the vortex cores (B is a coefficient of the order of 1). A function of the form (14) was recently discussed in Ref. 3.

The functions $N_S(H)$ for the three cases of anisotropic pairing discussed above are displayed in Fig. 2 for the unitary limit with $\Gamma_u = 0.1\Delta_0$ and $\Gamma_u = 0.01\Delta_0$. Since the averaging is performed under the assumption that $R \sim \xi_0(H_{c2}/H)^{1/2} \gg \xi_0$, only fields in the range $H_{c1} < H \leqslant 0.04H_{c2}$ are studied. To estimate H^* in the unitary limit, we obtain $H^*/H_{c2} \simeq (2\Gamma_u N(0)/\Delta_0 N_S)^2$, $H^* \sim 0.01H_{c2}$ for $\Gamma_u = 0.01\Delta_0$ and $H^* \sim 0.1H_{c2}$ for $\Gamma_u = 0.1\Delta_0$.

In closing, let us state once again the main result: In a mixed state of superconductors with lines of zeros in the excitation spectrum, the square-root dependence of the density of states on the magnetic field can change to a dependence of the form $H \ln H$ if the impurity density is sufficiently high.

[1] K. A. Moler, D. J. Baar, J. S. Urbach *et al.*, Phys. Rev. Lett. **73**, 2744 (1994).
[2] R. A. Fisher, J. E. Gordon, S. F. Reklis *et al.*, Physica C **252**, 237 (1995).
[3] E. Janod, R. Calemczuk, J.-Y. Henry, and J. Flouquet, preprint (1996).
[4] G. E. Volovik, J. Phys. C: Solid State Phys. **21**, L221 (1988).
[5] G. E. Volovik, JETP Lett. **58**, 469 (1993).
[6] D. Xu, S. Yip, and J. A. Sauls, Phys. Rev. B **51**, 16223 (1995).
[7] Yu. S. Barash and A. A. Svidzinsky, Phys. Rev. B **53**, 15254 (1995).
[8] N. B. Kopnin and G. E. Volovik, JETP Lett. **64**, 690 (1996).
[9] L. P. Gor'kov and P. A. Kalugin, JETP Lett. **41**, 253 (1985).
[10] K. Ueda and T. M. Rice in *Theory of Heavy Fermions and Valence Fluctuations*, edited by T. Kasuya and T. Saso, Springer, Berlin, 1985, p. 267.
[11] P. Hirschfeld, D. Vollhardt, and P. Wölfle, Solid State Commun. **59**, 111 (1986).
[12] P. Hirschfeld, P. Wölfle, and D. Einzel, Phys. Rev. B **37**, 83 (1988).
[13] K. Maki, in *Superconductivity*, edited by R. D. Parks, Dekker, New York, 1969.
[14] M. Sigrist and K. Ueda, Rev. Mod. Phys. **63**, 239 (1991).
[15] J. A. Sauls, Adv. Phys. **43**, 113 (1994).
[16] H. Won and K. Maki, Phys. Rev. B **53**, 5927 (1996).

Translated by M. E. Alferieff

Effect of spin relaxation on the polarization of excitonic luminescence in disordered systems

L. E. Golub and A. A. Kiselev

A. F. Ioffe Physicotechnical Institute, Russian Academy of Sciences, 194021
St. Petersburg, Russia

The kinetics of localized excitons in systems with disorder is studied with allowance for the fine structure of the excitonic state and for spin relaxation processes. The exciton distribution function, formed as a result of the competition between radiative and nonradiative recombination, spin relaxation, and intercenter transitions with an exponentially wide scatter in transition times, is calculated. © *1997 American Institute of Physics.* [S0021-3640(97)01008-6]

PACS numbers: 71.55.Jv, 71.35.Cc, 78.60.Ya, 76.60.Es, 77.22.Ej

Low-temperature luminescence in quantum-well structures is due to radiative recombination of excitons localized at nonuniformities of the heterointerfaces or at composition fluctuations. Therefore the presence of disorder in a system is directly reflected, for example, in the inhomogeneous width of the excitonic luminescence line and in the Stokes shift of the line relative to the excitonic absorption peak. This letter examines the influence of the exciton fine structure and the effect of spin relaxation processes on the behavior of such a system in an external magnetic field. The photoluminescence spectra of localized excitons are calculated, opening up additional possibilities for characterizing structures with nonuniformities by polarized luminescence methods.

BALANCE EQUATIONS IN HOPPING RELAXATION

If the arrival at all localization centers is identical, then in the absence of energy relaxation the luminescence spectrum has the same form as the density of localized states $g(\epsilon)$.[1,2] For convenience, here and below, the localization energy ϵ of a state is used as the argument. The fine structure of the state for each independent localization center can be taken into account, just as for excitons in an ideal system (see, for example, Ref. 3).

In the contrary case, the excitonic distribution forms as a result of competition between recombination processes (radiative and nonradiative) and spin and energy relaxation processes. Energy relaxation results in transitions of an exciton between states (at low temperature — with an increase in the localization energy). In disordered systems these processes are characterized by a substantial scatter in the times. For example, the rate of intercenter tunneling transitions is determined by the overlap of the states and therefore it is a rapidly decreasing (exponential) function of the distance between the centers.[4] In this case, from among all the localized states one can distinguish those from which departure due to energy relaxation is inefficient. The rate of transfer into other states is determined by the local configuration of the centers. The ratio of the total

recombination rate in a given excitonic state and the rate of departure into other states makes it possible to characterize the state as ''recombining'' or ''relaxing.'' The density $g^*(\epsilon)$ of the recombining states must be calculated in a specific model.

As a model system of the tail of localized states we shall consider a collection of localization centers distributed randomly in space. For simplicity, we confine our attention to energy relaxation in the approximation of hops to a nearest neighbor.[4,5] In this approximation the excitonic states can be classified according to the localization energy ϵ and the distance r to the nearest accessible center. Neglecting, in accordance with the approximation chosen, the dependence of the rate of intercenter transitions on the localization energy of the initial and final states, we obtain

$$g^*(\epsilon) = g(\epsilon)\exp[-\rho(\epsilon)V], \quad \rho(\epsilon) = \int_\epsilon^\infty d\epsilon' g(\epsilon'). \tag{1}$$

Here $\rho(\epsilon)$ is the density of localization centers with energy $\epsilon' > \epsilon$, and V is the volume of the region in which the absence of a nearest neighbor dictates whether the state is a recombining state. For example, for isotropic two-dimensional systems $V(r) = \pi r^2$, the area of a circle of radius r.

With allowance for the electron spin $s = \pm 1/2$ and the angular momentum of a heavy hole $j = \pm 3/2$, the bottom excitonic state $e1 - hh1(1s)$ is fourfold degenerate. Further, excitonic states with the projection of the angular momentum $s + j = +2, +1, -1$, and -2 on the growth axis of the structure are enumerated successively by the indices $m = 1, 2, 3$, and 4.

Assuming that the rate of hole spin relaxation is higher than that of the electron spin relaxation (see, for example, Ref. 6), we take into account only the flips of the hole spins. Then the spin relaxation processes are associated with the sublevels 1,3 and 2,4 of the excitonic quartet. Depending on the type of semiconductors in the heterostructure, the g factor of the electron and hole in the exciton can be positive or negative.[7] For definiteness, we choose $|g_e| < g_h$ (the case typical for GaAs/AlGaAs structures). In a magnetic field such that $\Delta_h \equiv \mu_B g_h B > k_B T$ this results in thermalization of the holes in the bottom Zeeman sublevel. Here the transitions $1 \rightarrow 3$ and $2 \rightarrow 4$ are the only important processes in the spin-flip problem.

The density $g_m^*(\epsilon)$ of recombining localized states is related with the sizes of the region $V_m \equiv V(r_m)$ by the relation (1), where $r_1, \ldots, r_4$ are determined by the rates of departure from the sublevels of the quartet

$$\omega_h(r_1) = \omega_n + \omega_s, \quad \omega_h(r_2) = \omega_r + \omega_n + \omega_s, \quad \omega_h(r_3) = \omega_r + \omega_n, \quad \omega_h(r_4) = \omega_n. \tag{2}$$

Here $\omega_r(\omega_n)$ is the radiative (nonradiative) recombination rate of an exciton and $\omega_h(r)$ determines the intercenter transition rate. We note that hole spin relaxation rate ω_s is included in the total recombination rate in the quartet states, since when the hole spin flips, the exciton departs from the corresponding sublevel. So, the density $g_m^*(\epsilon)$ of recombining states is different for different sublevels of a quartet.

Neglecting the spin relaxation processes, the following set of integral equations can be obtained for the average arrival $\Gamma_m(\epsilon)$ in an excitonic sublevel m of a state with localization energy ϵ in the stationary state in the case of low pump intensities:

$$\Gamma_m(\epsilon) = \Gamma_m^{(0)}(\epsilon) + \int_0^\epsilon d\epsilon' \frac{g(\epsilon') - g_m^*(\epsilon')}{\rho(\epsilon')} \Gamma_m(\epsilon'). \tag{3}$$

Here $\Gamma_m^{(0)}(\epsilon)$ is the arrival due to localization of free excitons or direct resonance generation of localized excitons. For sublevels 3 and 4, in taking into account the hole spin relaxation it is also necessary to take into account the arrival from sublevels 1 and 2, respectively. For the arrival $1 \rightarrow 3$ of interest to us below, this is most easily done if $\omega_r > \omega_s$. In this case an exciton in a recombining state (i.e., with a distance to the nearest neighbor $r > r_1$) is known to be in a recombining state $r > r_1 > r_3$ after the hole spin flips. Therefore further energy relaxation of such an exciton to sublevel 3 is impossible. Thus the transition $1 \rightarrow 3$ does not change $\Gamma_3^{(0)}(\epsilon)$, but the additional contribution to the luminescence from excitonic sublevel 3 due to flipping of the hole spin in the exciton must be taken into account. If $\omega_r < \omega_s$, then after the hole spin flips the localized exciton can continue to hop along the system of localization centers. This ''couples'' equations (3), and the resulting closed system of integral equations must be solved by numerical methods.

POLARIZATION LUMINESCENCE IN A MAGNETIC FIELD

Assuming the excitation to be nonresonant, we shall neglect the difference of the capture rates of excitons to states with different localization energies. Then $\Gamma_m^{(0)}$ does not depend on ϵ, and the luminescence intensities of an optically active doublet $m = 2,\ 3$ equal, respectively,

$$I_2(\epsilon) = \frac{\omega_r}{\omega_n + \omega_r + \omega_s} \mathcal{F}_2(\epsilon), \tag{4}$$

$$I_3(\epsilon) = \frac{\omega_r}{\omega_n + \omega_r} \left[\mathcal{F}_3(\epsilon) + \frac{\omega_s}{\omega_n + \omega_s} \mathcal{F}_1(\epsilon) \right],$$

where

$$\mathcal{F}_m(\epsilon) \equiv g_m^*(\epsilon) \Gamma_m(\epsilon) = \rho(0) \Gamma_m^{(0)} \frac{g(\epsilon)}{\rho(\epsilon)} \exp\{ -\rho(\epsilon) V_m + \mathrm{Ei}[-\rho(\epsilon) V_m]$$

$$- \mathrm{Ei}[-\rho(0) V_m]\},$$

and $\mathrm{Ei}(x)$ is the exponential integral function. The second term in $I_s(\epsilon)$ takes into account the above-described contribution to the luminescence of excitons arriving at sublevel 3 upon a flip of the hole spin.

With allowance for the Zeeman splitting of the states of the radiation doublet $\Delta \equiv \mu_B(g_h - g_e)B$, the degree of circular polarization of the luminescence is

$$P(\epsilon) = \frac{I_2(\epsilon + \Delta/2) - I_3(\epsilon - \Delta/2)}{I_2(\epsilon + \Delta/2) + I_3(\epsilon - \Delta/2)}. \tag{5}$$
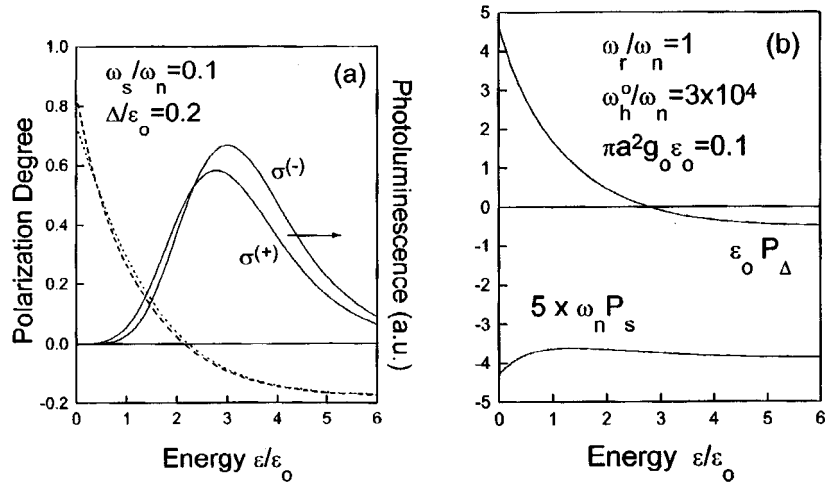
FIG. 1. a) Polarization of the luminescence of the tail of localized states in a magnetic field. The results of exact and approximate calculations of the circular polarization are shown by the dashed and dotted lines, respectively. The luminescence spectra in $\sigma^{(+)}$ and $\sigma^{(-)}$ polarizations are shown by the solid lines. b) Contributions of the Zeeman splitting of the radiation doublet (P_Δ) and spin relaxation processes (P_s) to the degree of circular polarization of the luminescence.

In moderately strong magnetic fields, such that the splitting Δ is much less than the characteristic localization energies, for a low spin relaxation rate ($\omega_s \ll \omega_n$) and the same rate of arrival in all sublevels ($\Gamma_m^{(0)} = \Gamma^{(0)}$), the expression for $P(\epsilon)$ can be expanded in a power series in Δ and ω_s:

$$P(\epsilon) = P_\Delta(\epsilon)\Delta + P_s(\epsilon)\omega_s,$$

$$P_\Delta(\epsilon) = \frac{g(\epsilon)}{2\rho(\epsilon)}[\rho(\epsilon)V_3 - e^{-\rho(\epsilon)V_3}] + \frac{1}{2}\frac{d}{d\epsilon}\ln\left[\frac{g(\epsilon)}{\rho(\epsilon)}\right], \qquad (6)$$

$$P_s(\epsilon) = -\frac{1}{2(\omega_r + \omega_n)} - \frac{S_3}{2V_3}[\rho(\epsilon)V_3 - e^{-\rho(\epsilon)V_3} + e^{-\rho(0)V_3}]\left[\frac{d\omega_h}{dr}\right]_{r=r_s}^{-1}$$

$$-\frac{1}{2\omega_n}\frac{\mathcal{F}(\epsilon)}{\mathcal{F}_3(\epsilon)},$$

where $S_3 = (dV/dr)_{r=r_s}$. We underscore the fact that here we have derived universal relations valid for arbitrary functions $g(\epsilon)$ and $\omega_h(r)$.

DISCUSSION

The solid lines in Fig. 1a show the luminescence spectra in $\sigma^{(\pm)}$ polarization calculated on the basis of the above model according to Eqs. (4) with an exponential localization-energy dependence of the excitonic density of states and a tunneling mechanism of intercenter transitions:

$$g(\epsilon) = g_0 e^{-\epsilon/\epsilon_0}, \qquad \omega_h(r) = \omega_h^0 e^{-r/a}, \tag{7}$$

where g_0 specifies the total density of localized states $\rho(0) = g_0 \epsilon_0$ and a is determined by the localization radius of the exciton. The calculation was performed for a two-dimensional system with the following set of parameters: $\pi a^2 g_0 \epsilon_0 = 0.1$, $\omega_r = \omega_n$, $\omega_s = 0.1 \omega_n$, $\omega_h^0 = 3 \cdot 10^4 \omega_n$, and $\Delta = 0.2 \epsilon_0$.

The luminescence contours are displaced with respect to one another on account of the Zeeman splitting of the radiation doublet. The integrated $\sigma^{(-)}$-polarization signal is stronger than the $\sigma^{(+)}$-polarization signal because of the hole spin relaxation. The polarization of the luminescence of the localized excitons is shown in Fig. 1 by the dashed line. The computational results obtained with the approximate formula (6) are shown by the dotted line. For the chosen parameter set a discrepancy between the results of the exact and approximate calculations is observed only near the mobility threshold, where the degree of circular polarization reaches high values, $P \simeq 1$.

The curves in Fig. 1 demonstrate the relative extent to which the degree of circular polarization of the luminescence is affected by Zeeman splitting (P_Δ) and spin relaxation processes (P_s).

The relaxation of localized excitons in a magnetic field is determined by the relative sizes of three energy scales — ϵ_0, Δ_h, and $k_B T$ — and requires a separate analysis of different limiting cases. For example, at temperatures $k_B T \ll \epsilon_0$ there is no need to take account of hops accompanied by a decrease of the localization energy or delocalization of the exciton. For typical values of ϵ_0 of the order of several meV, liquid-helium temperatures turn out to be low. However, the inequality $\Delta_h \gg k_B T$ can be satisfied only in strong magnetic fields or in heterostructures with large g factors. In the opposite case, both direct and inverse hole transitions between Zeeman sublevels must be taken into account. Relating the rates of inverse (ω_s^*) and direct (ω_s) transitions by the phenomenological relation $\omega_s^* = \omega_s e^{-\Delta h/k_B T}$, we obtain in the limit of a low spin relaxation rate $\omega_s \ll \omega_n$

$$P_s(T) = P_s (1 - e^{-\Delta_h/k_B T}).$$

Let us also point out a possible additional effect of external magnetic fields. In the case of nonresonance excitation of electron–hole pairs with a substantial density, the probability that an electron binds with its own hole (twin exciton) is negligibly small. This means that random electrons and holes bind to form an exciton, i.e., both the radiative and nonradiative states of an excitonic quartet are filled. An external magnetic field impedes carrier motion and effectively confines carriers near the point of production of the electron–hole pair, as a result of which the number of twin excitons increases and the radiation doublet is predominantly filled. This theory can be extended to the case of selective generation of an exciton on the sublevels of a quartet.

We note that in Ref. 8, in characterizing the disordered solid substitution solutions GaSeS, an analysis was made of the polarized luminescence spectra in a magnetic field in the Voigt geometry. Spin relaxation processes were neglected, and the polarization was due to mixing of the states of an excitonic triplet by the magnetic field.

The polarized luminescence of localized excitons in single crystals of the solid solution $CdS_{1-x}S_x$ in a magnetic field was recently investigated experimentally in Ref. 9. A spectral change in the sign of the circular polarization was observed at the short-

wavelength edge of the emission band. The fact that the positions of zero polarization and maximum luminescence do not coincide with one another is interpreted in Ref. 9 qualitatively in terms of the thermalization of excitons. In the present letter a systematic microscopic theory explaining this difference was constructed. A comparison with the calculations performed in the proposed model can be used for characterization of the samples, e.g., for determining the Urbach parameters of the tail of localized states, the spin relaxation rates, and the g factors of electrons and holes.

CONCLUSIONS

In this letter we have examined the kinetics of excitons in the tail of localized states of a disordered system in an external magnetic field in the Faraday geometry. We investigated the effect of energy and spin relaxation processes on the polarized luminescence spectra of localized excitons. The spectral dependence of the luminescence signals was obtained analytically for a model system in the approximation of hops between nearest neighbors.

[1] G. Bastard, C. Delalande, M. H. Meynadier *et al.*, Phys. Rev. B **29**, 7042 (1984).

[2] P. S. Kop'ev, I. N. Ural'tsev, Al. L. Éfros *et al.*, Fiz. Tekh. Poluprovodn. **22,** 424 (1988) [Sov. Phys. Semicond. **22**, 259 (1988)].

[3] F. Meier and B. P. Zakharchenya [Eds.], *Optical Orientation*, North-Holland, Amsterdam, 1984.

[4] A. G. Abdukadyrov, S. D. Baranovskiĭ, S. Yu. Verbin *et al.*, Zh. Éksp. Teor. Fiz. **98**, 2056 (1990) [Sov. Phys. JETP **71**, 1155 (1990)].

[5] L. E. Goub, E. L. Ivchenko, and A. A. Kiselev, J. Opt. Soc. Am. B **13**, 1199 (1996).

[6] E. L. Ivchenko and G. E. Pikus, *Superlattices and Other Heterostructures. Symmetry and Optical Phenomena*, Springer-Verlag, New York, 1995.

[7] A. A. Kiselev and L. V. Moiseev, Fiz. Tverd. Tela (St. Petersburg) **38,** 1574 (1996) [Phys. Solid State **38**, 866 (1996)].

[8] E. L. Ivchenko, M. I. Karaman, D. K. Nel'son *et al.*, Fiz. Tverd. Tela (St. Petersburg) **36,** 400 (1994) [Phys. Solid State **36**, 218 (1994)].

[9] A. N. Reznitskiĭ, S. Yu. Verbin, S. A. Permogorov *et al.*, Fiz. Tverd. Tela (St. Petersburg) **37,** 2140 (1995) [Phys. Solid State **37**, 1164 (1995)].

Translated by M. E. Alferieff

Evolution of vacancy defects in the surface layers of a metal irradiated with a pulsed electron beam

V. I. Lavrent'yev and A. D. Pogrebnyak
Sumy Institute of Surface Modification,[a) 244030 Sumy, Ukraine

R. Sandrik
Oxford University, OX1 3NP Oxford, UK

The distribution of vacancy defects in the surface layers of α-Fe after irradiation with a high-current pulsed electron beam is studied experimentally by unique nuclear-physical methods — low-energy positron annihilation, Rutherford backscattering (RBS), and proton-induced x-ray emission (PIXE). Regions with low local density, which are sources of crater formation on the surface of the irradiated sample, are observed by scanning a proton microbeam. Positron lifetime measurements reveal that as the electron beam power increases, nonequilibrium vacancies tend to be captured by carbon impurity atoms. © *1997 American Institute of Physics.* [S0021-3640(97)01108-0]

PACS numbers: 61.80.Fe, 61.72.Ji, 78.70.Bj

1. The interaction of high-density pulsed particle beams (photons, ions, electrons) with matter produces substantial changes in the properties of the surface layers[1–3] through a combination of energy absorption mechanisms. The absorption processes in such interactions generate high densities of point[4] and linear[5] defects. Reliable data on the defects produced by pulsed irradiation are required for studying the nature of the absorption mechanisms. At present these mechanisms have not been studied in detail because of the limited possibilities of the experimental methods for studying thin (thickness ranging from several nanometers up to several micrometers) surface layers with a nonuniform depth distribution of the defects.[1]

In the present work we employed a combination of modern nuclear-physical methods to study the characteristic features of the defect structure produced in the surface layers of α-Fe by irradiation with a pulsed low-energy high-current electron beam (LE-HCEB).

2. Annealed α-Fe samples with an initial grain size of 2–3 mm were used in the experiment. The total impurity content did not exceed 0.01 wt.% and the initial dislocation density was less than 10^7 cm^{-2}. The samples were irradiated in a Nadezhda-2 electron source[6] with average electron energy of about 20 keV, pulse duration $\tau \approx 0.8$ μs, and deposited energy density w per pulse from 1.0 to 5.3 J/cm^2. The working vacuum was equal to 10^{-4} Pa. The vacancy subsystem of the defect structure was studied by the low-energy positron beam method with positron energy from 0.2 to 30 keV (Trento University, Italy)[7] by measuring the lifetime τ_p and Doppler broadening parameter S of
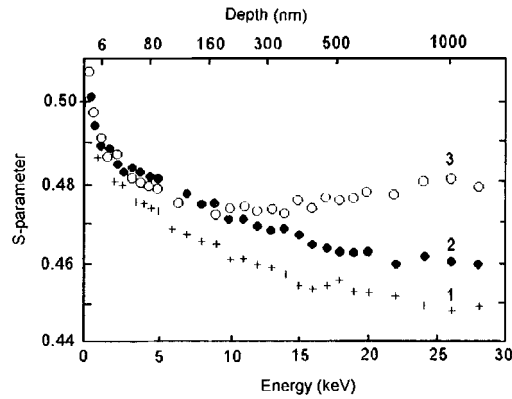
FIG. 1. S parameter of the Doppler broadening of the annihilation peak at 0.51 MeV versus the positron beam energy (layer depth) for α-Fe: 1 — initial state; 2 — after irradiation with a LEHCEB with $w=2.5$ J/cm^2, $\tau=0.8$ μs; 3 — average irradiation with a LEHCEB with $w=4.2$ J/cm^2, $\tau=0.8$ μs.

the annihilation peak (DBAP).[8] A ^{22}Na(e^+,γ) positron source with a measurement activity of 12 μCi in a Mylar packet was used to measure the positron lifetime. The lifetime of the source was described by two components: $\tau_1=250$ ns, $I_1=6.2\%$ and $\tau_2=450$ ns, $I_2=2.5\%$. A ^{207}Bi source was used for calibration. A qualitative analysis of the elemental distribution over the surface of the sample was performed using colored maps with regions ranging in size from 100×100 up to 2500×2500 μm, obtained by the RBS and PIXE methods by scanning a 3-MeV proton microbeam (Oxford University). The microbeam current was equal to 100 nA and the beam diameter was less than 1 μm.

3. Computer analysis of the time spectra of the positrons made it possible to determine the quantitative characteristics of the annihilating positrons in the experimental samples: the lifetime τ_p and the intensity I_p of the annihilation photons (in relative units). For example, for α-Fe samples irradiated with an electron beam with energy density $w=3.3$ J/cm^2, the positron time spectrum has two components: $\tau_{1p}=108$ ns, $I_{1p}=67\%$ and $\tau_{2p}=195$ ns, $I_{2p}=33\%$. Increasing the energy density of the electron beam to $w=4.2$ J/cm^2 changes the parameters of the positrons as follows: $\tau_{1p}=108$ ns, $I_{1p}=72.5\%$ and $\tau_{2p}=165$ ns, $I_{2p}=27.5\%$.

Figure 1 displays the energy spectra of the parameter S of the DBAP of α-Fe samples before and after one shot of an electron beam with different energy densities w. Actually, these dependences show the density distribution of vacancy defects over the depth beneath the surface. The results displayed in Fig. 1 attest to an increase in the vacancy content over the entire extent of the profile investigated (up to 1020 nm), starting at 20 nm. Increasing the energy density introduced by the electron beam in the interval 1.0–4.5 J/cm^2 increases the S parameter for the entire experimental range of positron energies. As w is further increased up to 5.2 J/cm^2, the density of the vacancy defects (S parameter) decreases, especially in the surface layers (up to 400 nm).

The RBS and PIXE investigations of the distribution of the elemental composition of the surface of α-Fe samples irradiated at low energy densities (w up to 3.5 J/cm^2),
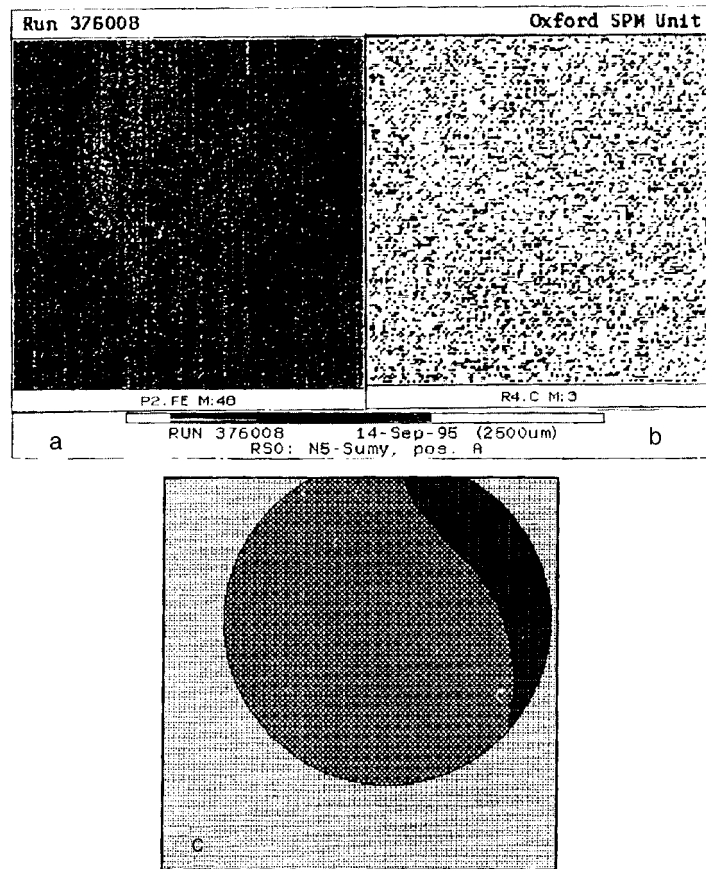
FIG. 2. PIXE (a) and RBS (b) maps, obtained for the distribution of the elements by scanning a proton microbeam, from 2500×2500 μm regions on the surface of an α-Fe sample irradiated with a LEHCEB with $w = 2.0$ J/cm^2: a — Fe; b — C; c — diagram of the surface distribution of Fe, showing a clearer image of the map a.

performed by scanning a proton microbeam, showed the presence of a carbon impurity distributed comparatively uniformly with average density 10–15 at.% in the investigated regions (Fig. 2b). No other impurities were observed in these experiments. However, characteristic ''shadings'' are observed on the color maps showing the iron distribution; these shadings define an apparently circular region of the surface about 2000 nm in size (Fig. 2a). The diagram presented in Fig. 2c exhibits a sharper black-and-white image of the observed iron distribution.

4. The initial depth profile of the energy absorbed in the pulsed irradiation of the metal surface by a 20-keV electron beam is a Gaussian with a maximum at a depth of about 1 μm.[1] Therefore if the energy density deposited in the sample is high enough, melting starts in the subsurface layers. Calculations performed by solving numerically a one-dimensional heat conduction equation for α-Fe irradiated with a 20-keV pulsed

electron beam (one pulse, $\tau = 0.8$ μs) show that as w increases from 2.3 to 5.2 J/cm^2, the thickness and lifetime of the melted layer increase in the range 0.7–2.5 μm and 0.5–3 μs, respectively.[2] The surface layer of α-Fe cools at a rate of $5 \cdot 10^9$ K/s and the crystallization front moves with a velocity from 2 to 5 m/s, depending on the cooling time and the depth of the layer.[2]

5. The results of a modeling of the melting of the surface layers of α-Fe under a pulsed electron beam show that for energy densities w less than 3 J/cm^2 there is rapid melting and quenching of a subsurface layer located at a depth of approximately 1 μm. At such high quenching rates $(5 \cdot 10^9$ K/s) a high density of nonequilibrium vacancies forms (up to 10^{-3}; Ref. 4), and these are detected by the positron annihilation method. The component of the positron lifetime $\tau_{1p} = 108$ ns, obtained by irradiating α-Fe ($w = 3.3$ J/cm^2), corresponds to the lattice of the defect-free iron crystal.[9] The second component $\tau_{2p} = 195$ ns is close to the lifetime of a positron at a divacancy.[10] Therefore, the nonequilibrium vacancies formed with low energy densities w of the electron beam mainly combine to form divacancies. The maximum density of divacancies initially lies at a depth of about 1 μm, corresponding to the maximum of the absorbed energy. As heat is redistributed under the influence of temperature gradients, the layers of material lying closer to the surface are heated more rapidly because the temperature in the surface layers is increasing at a higher rate than the temperature is decreasing into the interior of the sample.[1,2] As a result, most of the nonequilibrium vacancies (divacancies) migrate toward the surface. The easiest vacancy migration paths are dislocations and grain boundaries. This should result in the accumulation of vacancies near one- and two-dimensional defects in the surface layers of the sample. Therefore, the local density of the material should decrease near such defects. This phenomena is observed in the investigation of the surface distribution of the elements in a α-Fe sample irradiated with an electron beam with low energy w (up to 3 J/cm^2), for which the maps of the iron distribution along the boundary of a grain-sized region exhibit shadings indicating a decrease in the local density of the material at these locations (Fig. 2c). The fact that nonequilibrium vacancies migrate toward the surface is also conistent with the high values of the S parameter in the surface layers of the material (Fig. 1). Evidently, these regions with a low local density are the sources of cratering on the surface of material irradiated with a LEHCEB at high energy densities.[11,12]

The change in the second component of the positron lifetime to $\tau_{2p} = 165$ ns as the LEHCEB energy density increases to $w = 4.2$ J/cm^2 shows that the nonequilibrium vacancies join together to form ''vacancy–carbon atom'' complexes.[9] At this value of w the carbon density in α-Fe increases substantially after the action of the LEHCEB. Carbon enters the surface layers of the sample from the residual vapors in the vacuum chamber under the action of an intense electron beam even at low energy densities; this is illustrated by the results of the analysis of the elemental composition of the surface (Fig. 2b). Carbon migrates into the material under the action of the deformation wave generated by the LEHCEB; this determines the extended spatial distribution of the ''carbon–vacancy'' complexes and the high values of the S parameter in deeper layers (Fig. 1). Some of the vacancies, as a result of redistributions, annihilate with interstitial atoms, and in consequence the intensity of the second component I_{2p} decreases as w increases. Furthermore, the decrease in I_{2p} in the latter case could be due to the formation of complexes consist-

ing of a vacancy plus two or three carbon atoms as a result of an increase in the carbon concentration. The binding energy of a positron with a vacancy decreases sharply in such complexes, since the addition of carbon in ''vacancy–carbon atom'' complexes lessens the ability of a positron to be localized in the states formed.[9]

In summary, in the present work the evolution of vacancy defects in the surface layers of α-Fe after irradiation with a LEHCEB was studied by nuclear-physical methods (RBS, PIXE, low-energy positron annihilation). It was shown that as a result of the absorption of the energy deposited in the sample by the LEHCEB, regions with a low local density, in which the nonequilibrium vacancies displaced by the heat front from the quenched subsurface layer are concentrated, form on the surface of the sample near the boundary of an initial grain of the material. As the energy density in the electron beam increases, these regions can become sources of cratering. At the same time, as the carbon content increases, the nonequilibrium vacancies form ''vacancy–carbon atom'' complexes.

[a] e-mail: SIMP@demex.sumy.ua

[1] J. M. Poate, G. Foti, and D. C. Jacobson [Eds.], *Surface Modification and Alloying by Laser, Ion and Electron Beams*, Plenum Press, New York and London, 1985.

[2] A. D. Pogrebnyak and D. I. Proskurovskii, Phys. Status Solidi A **145**, 9 (1994).

[3] A. D. Pogrebnyak, Phys. Status Solidi A **117**, 17 (1990).

[4] V. I. Lavrent'ev, Fiz. Tverd. Tela (St. Petersburg) **36**, 3563 (1994) [Phys. Solid State **36**, 1896 (1994)].

[5] V. I. Lavarent'ev, Fiz. Tverd. Tela (St. Petersburg) **37**, 368 (1995) [Phys. Solid State **37**, 199 (1995)].

[6] D. I. Proskurovskii, G. E. Ozur, and V. P. Rotstein, Surf. Tech. **173**, 221 (1996).

[7] A. Zecca, V. Paridanse, N. M. Duarte *et al.*, Phys. Lett. **175**, 443 (1993).

[8] I. Ya. Dekhtyar, Phys. Rep. C **9**, 243 (1974).

[9] M. J. Puska and R. M. Nieminen, J. Phys. F **12**, L211 (1982).

[10] M. J. Puska and R. Nieminen, J. Phys. F **13**, 333 (1983).

[11] I. M. Goncharenko, V. I. Itin, S. I. Isichenko *et al.*, Zashchita Metallov **29**, 932 (1993).

[12] Yu. F. Ivanov, V. I. Itin, S. V. Lykov *et al.*, Izv. Ross. Akad. Nauk Metally, No. 3, 130 (1993).

Translated by M. E. Alferieff

Exciton−exciton collisions and conversion of interwell excitons in GaAs/AlGaAs superlattices

A. I. Filin,[a)] V. B. Timofeev, and S. I. Gubarev

Institute of Solid-State Physics, Russian Academy of Sciences, 142432 Chernogolovka, Moscow District, Russia

D. Birkedal and J. M. Hvam

Microelectronic Centret, Technical University of Denmark, DK28000, Lyngby, Denmark

The ratio of the densities of intra- and interwell excitons in a symmetric system of coupled quantum wells — a superlattice based on a GaAs/AlGaAs heterostructure — is investigated over a wide range of optical excitation power densities. Conversion of interwell excitons into intrawell excitons as a result of exciton−exciton collisions is observed at high exciton densities. Direct evidence for such a conversion mechanism is the square-root dependence of the interwell exciton density on the optical excitation level. The decrease in the lifetime of interwell excitons with increasing excitation density, as measured directly by time-resolved spectroscopy methods, confirms the explanation proposed for the effect. *© 1997 American Institute of Physics.* [S0021-3640(97)01208-5]

PACS numbers: 71.35.Gg, 78.47.+p

1. Excitonic states in semiconductor superlattices (SLs) remain a subject of scientific interest due to the importance of the influence of excitonic effects on the carrier energy spectrum in such systems. The overlapping of the wave functions of the size-quantum states corresponding to neighboring wells in semiconductor SLs leads to the appearance of coupled excitonic states in which electrons and holes are spatially separated and lie in different quantum wells.[1–4] Such states are called interwell excitons. Interwell excitons play an important role in the description of the optical and transport properties of semiconductor SLs, specifically, they determine the spectrum of optical transitions in the case of Wannier−Stark quantization of the carriers in an axial electric field.[3–5] Interwell excitonic states are also of interest because of the experimental discovery of Bloch oscillations and the electromagnetic radiation associated with them.[6,7]

Interwell excitons can also exist in symmetrically coupled quantum systems: double quantum wells and superlattices.[3,4,8–10] In the latter case the interwell excitons are similar to Wannier−Stark excitons in a superlattice with inclined bands, but in the symmetric case localization is of a Coulomb origin. In this situation the width of an excitonic miniband is much smaller than that of the corresponding electron and hole minibands.

In the present work we used time-resolved optical spectroscopy to study the processes that affect the lifetimes of interwell excitons in a symmetric system of coupled
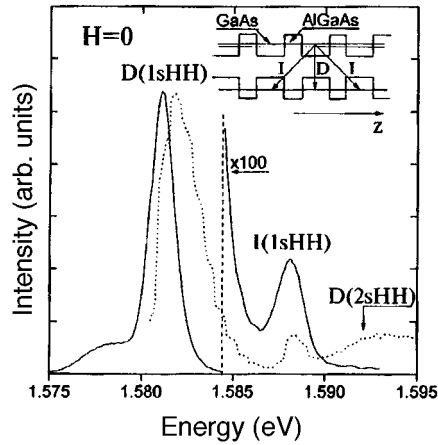
FIG. 1. PL spectrum (solid line) and fragment of the PL excitation spectrum (dotted line) of excitons with heavy holes. Inset: Arrangement of the experimental structure.

quantum wells. We discovered that the luminescence of interwell excitons is quenched with increasing density because the interwell excitons are converted into intrawell excitons as a result of exciton–exciton collisions.

2. We investigated a superlattice based on a $GaAs/Al_{0.3}Ga_{0.7}As$ heterostructure grown by molecular-beam epitaxy. The superlattice consisted of 20 symmetrically coupled GaAs wells, 80 Å wide, with $Al_{0.3}Ga_{0.7}As$ barriers, 50 Å wide, between them. It was shown previously on the basis of the luminescence excitation spectra that close to optimal conditions for observing interwell excitons are realized in such structures.[10,11] Specifically, it was that the oscillator strength of an interwell exciton is about 10^{-1} of the corresponding quantity for an intrawell exciton.

The photoluminescence (PL) spectra were studied as a function of the power density of continuous-wave (He–Ne laser, $\hbar\omega = 1.959$ eV) and pulsed (picosecond laser system, $\hbar\omega = 2.033$ eV) excitation. A optical waveguide technique was used to excite and collect the PL signal. The PL signal was detected by the time-correlated photon counting method, which made it possible to detect both the luminescence kinetics and the PL spectra with a definite time delay (time resolution 0.3 ns), including the time-integrated spectra.

3. Figure 1 displays the PL spectrum (solid line) and a fragment of the PL excitation spectrum (dotted curve) of excitons with heavy holes. The strongest line in the spectrum is $D(1sHH)$ — a state of an intrawell exciton. The excited state $D(2sHH)$, lying near the dissociated states of intrawell excitons, also appears in the PL excitation spectra. A line $I(1sHH)$ due to interwell excitons is observed between the $D(1sHH)$ and $D(2sHH)$ lines. These lines were identified on the basis of an investigation of the PL excitation spectra in magnetic fields.[11] Comparison of the intensities of the PL lines of intra- and interwell excitons in Fig. 1 shows that the interwell excitons are not in thermal equilibrium with the intrawell excitons, and the actual population of the states corresponding to the interwell excitons at $T = 1.5$ K is many orders of magnitude higher than
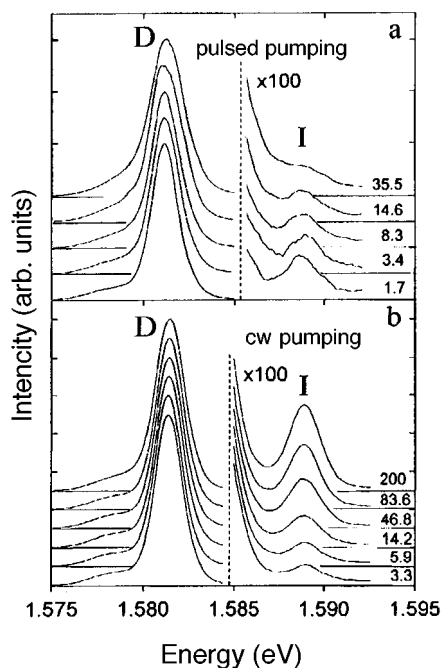
FIG. 2. a — Variation of the form of the PL spectra with increasing average pulsed-excitation power density P. The value of P, in W/cm^2, is indicated to the right of the spectra. All spectra are normalized to the intensity of the intrawell-exciton line. b — The same, for continuous excitation.

the thermal equilibrium population. We note that the $D(2sHH)$ line is not present in the PL spectrum. This means that the relaxation of intrawell excitons from an excited state to the ground state is much more rapid. The relatively slow relaxation of an interwell exciton into a intrawell exciton in the system under study is not unexpected, since for weak steady pumping the main relaxation mechanism is nonresonant subbarrier electron tunneling, which is a slow process. For the barrier widths in our system the tunneling time is estimated to be $\tau_{tun} \sim 10^{-9}$ s.

4. The behavior of the luminescence spectra of the intrawell (D) and interwell (I) excitons as a function of the stationary and pulsed excitation power density in the range from 10^{-3} to 10^{-1} W/cm^2 is illustrated in Figs. 2a and b. The density n_{intra} of intrawell excitons varied in the process, from 10^5 to 10^7 cm^{-2} in the case of cw pumping and from 10^8 to 10^{10} cm^{-2} in the case of pulsed excitation. The density n_{intra} was estimated assuming that all of the laser radiation energy absorbed in the sample goes into the formation of excitons. It has been established that, to a high degree of accuracy, the intensity of the luminescence from intrawell excitons is a linear function of the pumping over the entire experimental range of power densities. At the same time, the luminescence of the interwell excitons exhibits a clearly nonlinear character: superlinear growth of the intensity of an interwell exciton at low excitation levels and sublinear growth at high excitation levels (Fig. 3).
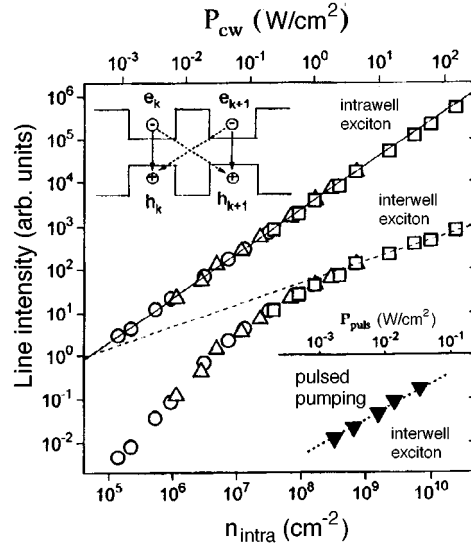
FIG. 3. Open symbols — intensity of the lines of intrawell (top set of points) and interwell (bottom set of points) excitons as a function of the intrawell exciton density. The top abscissa shows the continuous excitation power density. Filled symbols — intensity of an interwell-exciton line with pulsed excitation on the same density scale. The corresponding power density scale is displayed on the additional axis in the bottom right-hand side of the figure. The straight lines correspond to dependences of the form $y = x^\alpha$: solid line — $\alpha = 1.0$ (linear dependence); dashed line — $\alpha = 0.5$ (square-root dependence); and, dotted line — $\alpha = 0.85$ (sublinear dependence). Inset: Diagram of the conversion process from an interwell to an intrawell exciton .

We attribute the quenching of the luminescence of interwell excitons under strong pumping to inelastic exciton-exciton collision processes. As the density of the interwell excitons increases, the probability of exciton–exciton pair collisions with conversion into intrawell excitons increases appreciably. This process is illustrated schematically in the inset in Fig. 3 and can be written as follows: $e_k h_{k+1} + e_{k+1} h_k \rightarrow e_k h_k + e_{k+1} h_{k+1}$, where $e_k h_{k+1}$ and $e_{k+1} h_k$ is an interwell exciton, consisting of an electron and a hole localized in different (kth and $k + 1$st) wells, and $e_k h_k$ and $e_{k+1} h_{k+1}$ is a intrawell exciton consisting of an electron and hole localized in the same well. This conversion mechanism does not require subbarrier electron or hole tunneling and can be very efficient at high interwell exciton densities.

The kinetic equation describing the interwell exciton density n_{inter} has the form

$$\frac{dn_{\text{inter}}}{dt} = g_{\text{inter}} - \frac{n_{\text{inter}}}{\tau_{\text{rad}}} - \frac{n_{\text{inter}}}{\tau_{\text{tun}}} - \frac{n_{\text{inter}}}{\tau_{\text{con}}},$$

where the term g_{inter} is responsible for the generation of interwell excitons, τ_{rad} is the radiative lifetime, τ_{tun} is the quantum tunneling time, and τ_{con} is the conversion time of interwell into intrawell excitons. Here the different channels for nonradiative losses of interwell excitons, besides tunneling and conversion, are neglected. Assuming that τ_{con} is the average inelastic collision time for interwell excitons, we can write

$\tau_{con}^{-1} = \sigma_{ex-ex} V_{ex} n_{inter}$, where σ_{ex-ex} is the exciton–exciton scattering cross section and V_{ex} is the thermal velocity of the excitons. Under stationary conditions we have

$$g_{inter} = \left(\frac{1}{\tau_{rad}} + \frac{1}{\tau_{tun}} \right) n_{inter} + (\sigma_{ex-ex} V_{ex}) n_{inter}^2.$$

At high densities the terms linear in n_{inter} can be neglected. Then $n_{inter} \sim (g_{inter})^{1/2}$. Assuming that $g_{inter} \sim P \sim n_{intra}$, where P is the excitation power density and n_{intra} is the intrawell exciton density, and taking into account the fact that the intensity I_{inter} of the interwell exciton line is given by $I_{inter} = n_{inter} / \tau_{rad}$, we obtain $I_{inter} \sim n_{intra}^{1/2} \sim P^{1/2}$, i.e., in the limit of high densities the intensity of an interwell-exciton line asymptotically approaches a square-root dependence on the excitation power density (dashed line in Fig. 3).

The superlinear growth of the intensity of an interwell exciton at low excitation densities could be due to electron and hole localization on fluctuations of the random potential (fluctuations of the relief at the heterointerfaces of the quantum wells). In the case of strong localization the overlap of the electron and hole wave functions in the plane of the wells decreases, and the radiative probability of an interwell exciton decreases. As the pump power density increases, the localized states are filled and most interwell excitons are above the mobility threshold. The exciton–exciton scattering mechanism becomes possible for mobile excitons and for this reason, as the excitation power density increases further, the superlinear dependence of the intensity changes into a sublinear dependence.

In the low densities the term quadratic in n_{inter} can be neglected in the kinetic equation. Then, since $\tau_{rad} \gg \tau_{tun}$, we obtain $I_{inter} \sim g_{inter} \tau_{tun} / \tau_{rad}$. Therefore, at low densities the superlinear increase of the intensity could be due to the decrease in the τ_{rad}.

The assumption that the conversion time of interwell into intrawell excitons decreases as a result of exciton–exciton collisions at high densities is confirmed by measurements of the decay kinetics of PL. Curves of the decay of the PL of an interwell exciton are displayed in the top part of Fig. 4. The decrease in the lifetime is already evident from the kinetic curves obtained for four different pump power densities. However, the interwell-exciton line lies on the comparatively intense short-wavelength shoulder of the line of an intrawell exciton, whose dynamics can distort the kinetics of the line under study. The time dependences of the intensity of the interwell-exciton line are shown at the bottom of Fig. 4 for two pump power densities. The curves were obtained from the time-delayed spectra by the spectral deconvolution method. The very small decrease in the lifetime from $\tau = 0.58$ ns for $P_1 = 1.7 \cdot 10^{-3}$ W/cm^2 to $\tau = 0.42$ ns for $P_4 = 3.5 \cdot 10^{-2}$ W/cm^2 is due to the fact that in this range of pump power densities the lifetime is determined mainly by τ_{tun}, while according to our estimates τ_{con} varies from 15 to 5 ns.

The intensity of the PL line of interwell excitons is shown at the bottom right-hand side of Fig. 3 as a function of the peak intrawell-exciton density with pulsed excitation. (To simplify the figure, the curve of the intrawell-exciton line intensity, which is linear just as in the case of continuous pumping, is not presented in the figure.) The scale of the peak densities with pulsed pumping is combined with the scale of the densities with
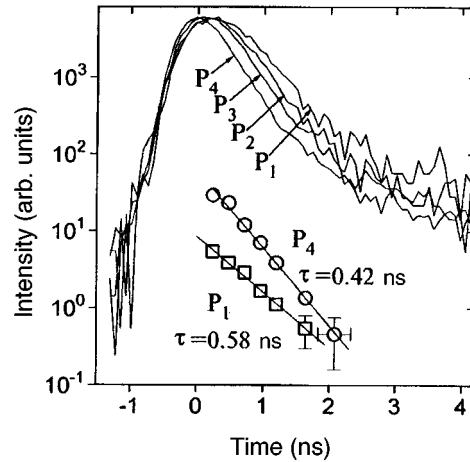
FIG. 4. Variation of the PL kinetics of an interwell exciton with increasing pumping from $P_1 = 1.7 \cdot 10^{-3}$ to $P_4 = 3.5 \cdot 10^{-2}$ W/cm^2. Bottom part of the figure — time dependence of interwell-exciton line intensities for two pump power densities; the values plotted were obtained from time-delayed spectra by the spectral-deconvolution method. The straight lines correspond to a decay with the characteristic time $\tau = 0.58$ ns for P_1 and $\tau = 0.42$ ns for P_4. The experimental error along the X axis is the same for all points and corresponds to the width of the time gates. The error along the Y axis is indicated for the points where it exceeds the size of the symbol.

continuous pumping. The dependence shown is clearly sublinear (see also the spectra in Fig. 2a) and is described by the power law $y = x^\alpha$ with $\alpha = 0.85$. This value of α agrees with the fact that the peak density in the pulsed experiment corresponds to the transitional region from a superlinear to a square-root law.

5. In closing, we note that the proposed mechanism of conversion of inter- into intrawell excitons as a result of exciton–exciton collisions is most efficient in a symmetrically coupled system of quantum wells with flat bands. In systems with tilted bands, this mechanism should be suppressed as a result of the polarization of the electron and hole by the electric field.

[a] e-mail: filin@issp.ac.ru

[1] A. Chomette, B. Lambert, B. Deveaud et al., Europhys. Lett. **4**, 461 (1989).
[2] H. Chu and Y.-C. Chang, Phys. Rev. B **39**, 10861 (1989).
[3] D. M. Whittaker, Phys. Rev. B **41**, 3238 (1990).
[4] M. M. Dignam and J. E. Sipe, Phys. Rev. B **41**, 2865 (1990); Phys. Rev. B **43**, 4097 (1991).
[5] E. Mendez, F. Agulli-Rueda and F. Hong, Phys. Rev. Lett. **60**, 2426 (1988).
[6] K. Leo, P. Bolivar, F. Bruggemann, and R. Schwedler, Solid State Commun. **84**, 943 (1992).
[7] H. Roskos, M. C. Nuss, J. Shah et al., Phys. Rev. Lett. **68**, 2216 (1992).

[8] L. V. Butov, A. Zrenner, G. Abstreiter *et al.*, Phys. Rev. B **52**, 12 153 (1995).
[9] M. Bayer, V. B. Timofeev, F. Faller *et al.*, Phys. Rev. B **54**, 8799 (1996).
[10] D. Birkedal, K. El Sayed, G. Sanders *et al.*, Phys. Rev. B **54**, 10316 (1996).
[11] A. I. Tartakovskiĭ, V. B. Timofeev, V. G. Lysenko *et al.*, JETP, in press (1997).

Translated by M. E. Alferieff

Characteristic features of vortex depinning in a layered superconductor

V. N. Zavaritskiĭ[a)]

Kapitsa Institute of Physics Problems, Russian Academy of Sciences, 117334 Moscow, Russia; IRC in Superconductivity, University of Cambridge, Cambridge CB3 0HE, England; Institute of General Physics, Russian Academy of Sciences, 117942 Moscow, Russia

The field $H^*(T)$ for the onset of dissipation is estimated self-consistently from the results of an investigation of the transverse resistance and current–voltage characteristics of a $Bi_2Sr_2CaCu_2O_8$ (BSCCO-2212) single crystal in a mixed state. It is established that H^* is close to H_{c1} in the interval $T_c/2 \leq T \leq T_c$. Rapid growth of $H^*(T)$, accompanied by a transformation of the current–voltage characteristics, as the temperature decreases below ≈ 40 K attests to the formation of a nonvanishing region of stability of an ordered state of the vortex system, possibly as a result of a change in the effective dimensionality of the fluxoid. © *1997 American Institute of Physics.* [S0021-3640(97)01308-X]

PACS numbers: 74.60.Ge, 74.72.Hs

There are a large number of theoretical works,[1] which need to be verified experimentally, on the properties of the vortex system in layered high-T_c superconductors. Of greatest interest is the prediction that the thermodynamic character of the melting of a regular vortex lattice will change from a first-order phase transition in the weak-disorder limit to various types of ''vortex glass–vortex liquid'' transitions as the degree of disorder increases.[1] There are many works, most of which were performed on BSCCO-2212 crystals, devoted to verifying these predictions.[2–6] Perfect single crystals are used for investigations of the effect of weak disorder because the coherence length is small, which decreases to the atomic level the scale of defects which influence the properties of the vortex system. In most investigations[2–6] (see footnote[b)]) the phase transformation in a vortex system has been identified with an experimentally measured quantity, the so-called line of irreversibility or irreversibility field $H_{irr}(T)$, which in field–temperature coordinates separates the dissipative state from the region of undamped currents. Although most papers on the BSCCO-2212 system claim good agreement of the results with the corresponding models, a comparison of the results obtained by different methods reveals both quantitative discrepancies (reaching several orders of magnitude) and a different character of the temperature dependence $H_{irr}(T)$. Since the ''vanishingly small'' value of the critical current is often associated with the observational capability of the experimental method, the discrepancies mentioned can presumably be attributed to differences in the sensitivity of the methods employed. However, as far as I know, the problem of taking

into account the influence of the criterion used on the magnitude and character of the temperature dependence $H_{irr}(T)$ has thus far not even been posed, even though in several cases, for example in Ref. 4, the aforementioned discrepancies have been invoked to confirm the applicability of some elegant theoretical constructs.

In the present work the dynamic characteristics of a vortex system in the mixed state of a $Bi_2Sr_2CaCu_2O_8$ (BSCCO-2212) crystal were investigated by the resistive method; transverse charge-carrier transport was used to obtain a weak measuring current regime. An additional argument was that the transverse transport is sensitive to the interlayer interaction, which determines the properties of the system.[8] The influence of the resistive criterion R^* employed to determine H_{irr} on the magnitude and character of the temperature dependence $H^*(T)$ extracted from the experimental data was studied and the interpolation construction of the $H^*(T)$ dependence for the level R_{th} corresponding to the onset of a deviation from linearity of the current–voltage characteristic (IVC) of the crystal was tested.

For the experimental BSCCO-2212 crystals $T_{c0} \simeq 86.3$, 89, 92.3, and 92.9 K,[c] the high critical temperature being due to the partial substitution of yttrium impurity for calcium in the lattice.[9] The samples were selected according to their macroscopic composition uniformity and the absence of blocks[10] (see footnote[d]); low-resistance electrical contacts were prepared by fusing a conducting composite in both ab planes.[11] The temperature dependences of the transverse resistance were measured with an ac current bridge (10–100 μA) at 10–77 Hz. The rate of change of the temperature was chosen so that that maximum temperature difference between the measuring thermometer and the sample did not exceed 10 mK. The quasistationary IVCs were measured for dc current; the noise level of the circuit did not exceed 2 nV in a 15 T field. These experiments were conducted in a short-circuited solenoid at constant (± 5 mK) temperature. The measurements were performed in the previously described superconducting cryomagnetic systems with an active temperature control scheme;[11,12] the orientation $H \perp ab$ was set directly in the course of the experiment according to the maximum of the angular dependence of the resistance in the mixed state of the crystal.

The typical temperature dependences of the interlayer resistance of a BSCCO-2212 single crystal are displayed in Fig. 1a in $R–1/T$ coordinates. They clearly illustrate the character of the variation of the resistance as the resistive state is established in the sample. Since the irreversibility field is determined according to the resistance decreasing below a definite value R^* determined by the resolution of the particular experiment, and since the broadening of the transition in a magnetic field is continuous, the decisive influence of the criterion R^* on H_{irr} is obvious. This is illustrated in Fig. 1b, which displays the values of H^* determined from the data in Fig. 1a for a number of values of R^*. In constructing the functions $H^*(T)$ a correspondence was established between the temperature at which the resistance decreased to R^* and this external field. As one can see from the figure, while H^* depends strongly on R^*, the change in the character of the temperature dependences $H^*(T)$ is not so great. Therefore, in order to estimate the physically reasonable values of $H_{irr}(T)$, an attempt was made to construct the $H^*(T)$ curves for an arbitrarily small level R^* by extrapolating the experimental data of Fig. 1b, assuming that the character of the change in the dynamical characteristics of the system remains unchanged as $R \rightarrow 0$. Specifically, it was postulated that the character[e] of the
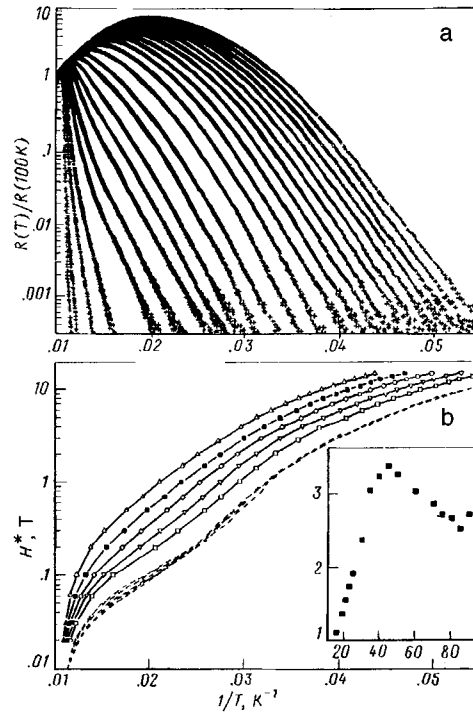
FIG. 1. a) Typical temperature dependences of the reduced transverse resistance of BSCCO-2212 in a constant external field perpendicular to the *ab* plane of the crystal. The results are presented for $H = 0.02, 0.03, 0.06, 0.1,$ 0.2, 0.3, 0.5, 0.7, 1.0, 1.4, 2.0, 3.0, 4.0, 5.0, 6.0, 7.0, 8.0, 9.0, 10.0, 11.0, 12.0, 13.0, 14.0, and 15.0 T (left to right). b) Values of H^* determined according to the data in *a* for the levels $R^*/R(100 \text{ K}) = 3 \cdot 10^{-2},$ $1 \cdot 10^{-2}, 3 \cdot 10^{-3}, 1 \cdot 10^{-3},$ and $3 \cdot 10^{-4}.$ The dashed curve is an extrapolation of the experimental curves $H^*(T)$ to the level $R_{th}.$ Inset: Temperature variation of the exponent γ in the approximation of $H^*(R^*)$ by the relation $R^* \sim H^{\gamma(T)}.$

dependence $R^* \sim H^\gamma$ determined for $T =$ const from the data in Fig. 1b remains unchanged; the values of the exponent γ are given in the inset in Fig. 1b. Finally, it was assumed that this approximation could be extrapolated to a range of temperatures only partially measured experimentally, specifically, to two bounded intervals — one interval directly near T_{c0} and the other at low temperatures. On the basis of these assumptions, the construction of a $H^*(T)$ curve for an arbitrarily small level of R^* is trivial. But since the phase transition in a vortex system presupposes *a priori* the development of strong nonlinearities in the dynamical characteristics of the system,[1] additional investigations were required in order to clarify the limits of applicability of the assumptions employed.

Since the IVCs are sensitive to the dynamical properties of the vortex system,[1] the transverse $V(I)$ curves were measured in the temperature range 27–100 K for several fixed values of the external magnetic field. Special attention was focused on the region $50 < T < 75$ K, where the effect of R^* on $H^*(T)$ is strongest (see Fig. 1b). It was determined that the transverse $V(I)$ characteristics of the BSCCO-2212 crystal in a mixed state are very complicated, their character being illustrated by the curves in Fig. 2. As one
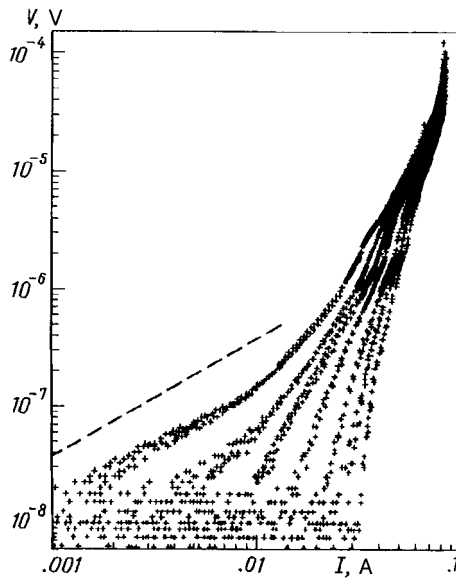
FIG. 2. Temperature evolution of the transverse IVC of a BSCCO-2212 crystal at $T \approx 52.7$, 53.3, 54.6, 55.1, 55.6, and 56.2 K, $H = 0.08$ T. Dashed curve — $V \propto I$.

can see from the data presented, appreciable nonlinearities are observed at high currents. As a rule, they are accompanied by a multivalued, hysteretic IVC; moreover, asymmetry of the characteristics with respect to the direction of the current is often observed, as one can see from the data for $T \approx 55.1$ K in Fig. 2. The nonlinearity and especially the multivaluedness of the characteristic evidently are due to the Josephson nature of the interlayer interaction, though the parasitic effect of overheating also cannot be completely ruled out. A more detailed discussion of this question falls outside the scope of this letter.

We note that in most measurements of the transverse IVCs in BSCCO-2212 attention was focused mainly on the characteristics of the internal Josephson effect,[13,14] specifically, on the magnitude of the superconducting gap in the excitation spectrum and in consequence a voltage sensitivity several orders of magnitude coarser than ours was used. Perhaps this is why it remained unnoticed that in a wide range of temperatures and fields jumps to ''quasiparticle'' branches occur not from a nondissipative Josephson ''trunk'' but from a substantially resistive characteristic, which is close to Ohmic in the low-voltage region. At the same time, it must be said that our results, though exhibiting clear discrepancies with the data in Refs. 13–15, are in qualitative agreement with the more precise measurements in Ref. 4.

In contrast to Refs. 13 and 14, in the present study the initial segments of the IVCs of the crystal were of greatest interest. It was determined that they are satisfactorily approximated by a linear law over a wide (field-dependent) temperature range below the critical temperature, while as the temperature decreases below a field-dependent threshold T_{th}, deviations from Ohm's law are observed first at the lowest voltages detected in the experiment. This is illustrated in Fig. 2, which displays IVCs measured at several
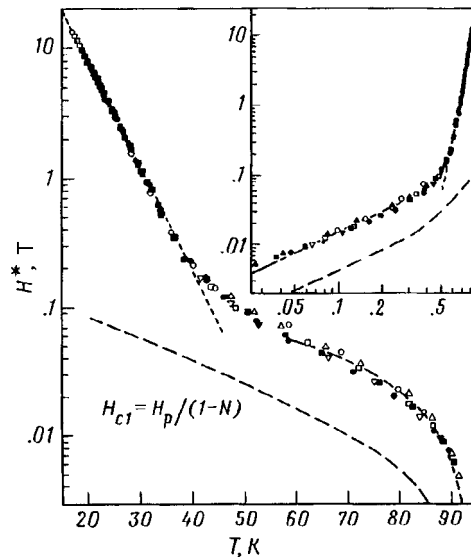
FIG. 3. Characteristic field $H^*(T)$ constructed by extrapolating the experimental points to the level R_{th}; the designations are the same as in Fig. 1b. Dashed curves — asymptotic expressions (1) and $H_{c1}(T)$. The penetration field H_p was determined according to the deviation of the diamagnetic susceptibility from a constant;[16] these data were obtained on two fragments of the same crystal in a separate SQUID magnetometric experiment. Close values of the demagnetizing factor N were determined both by a calculation in which the shape of the sample was approximated by an inscribed ellipsoid, and by a direct experiment with a tin sphere and foil close in size to the sample. Inset: Identical data presented as a function of the reduced temperature $1 - T/T_c$.

temperatures in a narrow region $T \approx 52$–56 K near T_{th}; the dashed curve shows the Ohmic dependence $V(I)$. It is obvious that the development of nonlinearities of the IVC, attesting to the presence of a nonvanishing critical current, simultaneously changes the meaning of the concept of resistance and establishes a natural limit of applicability for our assumptions.

As one can see from Fig. 2, the change in the character of the IVC from linear to non-Ohmic occurs in a relatively narrow temperature range of width ≈ 1 K. The effect can be characterized by a threshold resistance R_{th} corresponding to the lower limit of the Ohmic response. Analysis of families of IVCs (similar to those presented in Fig. 2) measured for several values of the external field gave estimates R_{th} of virtually the same magnitude for $T_{th} \approx 35$, ≈ 47, ≈ 55, and ≈ 76 K.

The temperature dependence obtained for the characteristic field H^* by extrapolating the experimental points to the level R_{th}, which is obviously a natural lower limit of applicability of the extrapolation procedure employed, is shown by the dashed curve in Fig. 1b. These same data are presented in the standard scales in Fig. 3, where the different symbols denote the initial levels of R^* (the designations are the same as in Fig. 1b). As one can see from Fig. 3, the curve constructed is satisfactorily approximated by the relations

$$H \sim \exp(-T/T_0), \quad H \sim (1 - T/T_c)^{\beta}, \tag{1}$$

at low temperatures and at temperatures near T_c, respectively, as shown in the figure by the dashed lines for the parameters $T_0 \simeq 5.4$ K, $T_c \simeq 93.9$ K, and $\beta \simeq 1$. We note that the critical exponent is determined with a low accuracy, since the scatter of the points admits an approximation with $\beta = 0.9 - 1.4$. The value $\beta \simeq 1$ was used on the basis of the fact that the adjustable parameter T_c was close to the experimentally determined value $T_{c0} \approx 92.9$ K.

As one can see from Fig. 3, in a wide region $T \gtrsim 40$ K the temperature dependence of the characteristic field is close to $H_{c1}(T)$, demonstrating only quantitative discrepancies. This result agrees qualitatively with Zel'dov's observations[5] and supports the idea that the efficacy of vortex pinning vanishes at high temperatures as a result of an effective breakdown of their cohesiveness due to thermal fluctuations.

The decending character of the IVC, similar to what we observed at temperatures $T < T_{th}$, is ordinarily attributed to a nonvanishing critical current. However, since the detective power of the experiment corresponds to a substantial electric field $\approx (1-10) \cdot 10^{-6}$ V/cm in the sample, it is impossible to rule out the possibility that the $V(I)$ characteristic is S-shaped with a second Ohmic segment beyond the limits of our resolution. In this case the true phase boundary for the existence of an undamped supercurrent in a wide temperature range, $T > 40$ K, obviously approaches, if not asymptotically, H_{c1} and the existence region of the vortex lattice becomes vanishingly narrow, casting doubt on the adequacy of the interpretation in Ref. 5.

The sharp change in the character of the temperature dependence $H^*(T)$ at low temperatures $T < 40$ K is probably due to an additional mechanism that increases the effectiveness of pinning and can tentatively be attributed to a change both in the character of the pinning itself and in the effective dimension of the vortex filament. Indirect evidence in support of the latter conjecture could be the change, observed at $T \approx 30-35$ K, in the character of the IVC from the type illustrated in Fig. 2 to the hysteretic quasi-Josephson characteristics with a distinguished nondissipative (at the noise level) branch separated from the numerous ''quasiparticle'' branches by a gap $\approx 10^{-5}-10^{-4}$ V. Such an IVC attests, with a high degree of reliability, to the development of a nondissipative state and is consistent with the model of two-dimensional melting,[1] which predicts a temperature $T_m^{2D} \approx 25$ K close to that obtained experimentally. At the same time, both the type of dependence of the low-temperature branch $H^*(T)$ and the parameters of the corresponding asymptotic expressions (1) satisfactorily agree with those calculated in Ref. 17 under the assumption that the geometric barrier has the governing effect.

[a] e-mail: vlad@kapitza.ras.ru

[b] References 2–6 are by no means exhaustive: There are more than 100 published works on this subject, and the interpretation of the results of the few known exceptions requires *a priori* the validity of some assumptions that are by no means obvious.[7]

[c] T_{c0} was determined at the level $R = 10^{-4} R_{max}$ according to the $R(T)$ measurements in the laboratory field. The main conclusions of this work are based on the results of detailed investigations of the crystal with $T_{c0} \approx 92.9$ K, which agree well with the data obtained in control experiments on all other samples.

[c] The spread in the critical temperatures for any pair of contacts to the sample did not exceed the transition width, equal to 0.6–1.8 K according to the $(0.9 - 10^{-4}) R_{max}$ criterion. The absence of splitting and a fine structure of the minima in the angular dependences $R(\phi)$ in the resistive state in 80 kOe gives an estimated upper bound of $<0.015°$ for the angle of disorientation of the blocks.

[e] In other words, it is postulated that the activational character of the decrease in the resistance with temperature remains unchanged: As one can see from Fig. 1a, the resistive ''tails'' for $R(T)/R(100$ K$) \lesssim 3 \cdot 10^{-2}$ are satisfactorily approximated by this law over the entire range of fields investigated.

[1] G. Blatter, M. V. Feigel'man, V. B. Geshkenbein *et al.*, Rev. Mod. Phys. **66**(4), 1125 (1994).

[2] C. Duran, J. Yazyi, F. de la Cruz *et al.*, Phys. Rev. B **44**, 7737 (1991).

[3] A. Shilling, R. Jin, J. D. Guo, and H. R. Ott, Physica C **235−240**, 2741 (1994).

[4] J. H. Cho, L. N. Bulaevskii, M. P. Maley *et al.*, Phys. Rev. B **50**, 6493 (1994).

[5] E. Zeldov, D. Majer, M. Konczykowski *et al.*, Nature **375**, 373 (1995).

[6] C. D. Dewhurst, D. A. Cardwell, A. M. Campbell *et al.*, Phys. Rev. B **53**, 14594 (1996).

[7] S. L. Lee, P. Zimmerman, H. Keller *et al.*, Phys. Rev. Lett. **71**, 3862 (1993).

[8] S. L. Cooper and K. E. Gray, *Physical properties of HTSC IV*, edited by D. M. Ginsberg, World Scientific, 1994.

[9] N. V. Zavaritskiĭ, V. N. Zavaritskiĭ, A. P. McKenzie *et al.*, JETP Lett. **60**, 193 (1994).

[10] V. N. Zavaritsky and W. Y. Liang, J. Low Temp. Phys. **105**, 1273 (1996).

[11] V. N. Zavaritskiĭ, JETP Lett. **63**, 139 (1996).

[12] V. N. Zavaritsky, Phys. Scr. **66**, 230 (1996).

[13] R. Kleiner and P. Müller, Phys. Rev. B **49**, 1327 (1994).

[14] A. A. Yurgens, D. Winkler, N. V. Zavaritsky *et al.*, Phys. Rev. B **53**, R8887 (1996).

[15] T. Yasuda, M. Tonouchi, and S. Takano, Czech. J. Phys. **46**, Suppl. S3, 1265 (1996).

[16] N. V. Zavaritskiĭ and V. N. Zavaritskiĭ, JETP Lett. **53**, 226 (1991).

[17] L. Burlachkov, V. B. Geshkenbein, A. Koshelev *et al.*, Phys. Rev. B **50**, 16770 (1994).

Translated by M. E. Alferieff

Application of symmetry operations for construction of quasiperiodic structures in a plane

A. A. Polyakov[a)]

Chelyabinsk State Technical University, 454080 Chelyabinsk, Russia

A method is proposed for constructing a quasiperiodic structure of symmetry elements — regular pentagons and five-pointed stars — in a plane. The growth of the structure is determined by the action of the symmetry operations, whose effect is not completely identical to that of similar operations in classical crystallography. The tiling (''flower of pentagons''), consisting of a central pentagon and five side pentagons joined along the edges, is studied. The growth of this tiling is accompanied by the appearance of a ''flower of stars'' and by the formation of isolated pores in the form of rhombi. The relation between the obtained structure and Penrose tiling is examined, and it is noted that some vertices of the Penrose tiling coincide with all vertices of the polygons of the packing obtained. © *1997 American Institute of Physics.* [S0021-3640(97)01408-4]

PACS numbers: 61.50.Ah, 61.44.Br

The experimental discovery of quasicrystals[1] has generated a spate of interest in possible methods for resolving the conflict between the existence of quasiperiodic structures with five- and tenfold symmetry axes and the fact that classical crystallography forbids such structures. Before this discovery, planar quasiperiodic structures with five-fold axes had been constructed by means of Penrose tiling.[2] This packing and an entire class of quasiperiodic structures have been described by different methods, among them projecting methods[3,4] and methods for constructing two- and three-dimensional Penrose tilings by formulating matching rules or deflation rules[2,4,5] for polygons or polyhedra. A transition from cubic lattices in five and six dimensions to quasicrystalline lattices in two and three dimensions has been worked out in the projecting methods. The existence of translational and rotational symmetry in such models has been suspected (a N-dimensional periodic lattice was used as the initial lattice), but thus far an approach to constructing such structures by means of the symmetry operations belonging to classical crystallography and acting on symmetric geometric objects has not been worked out.

At the same time, attempts have been made to describe quasiperiodic structures from the standpoint of the regular defectiveness of standard crystal packings as well as by constructing a Frank–Casper phase with a large unit cell.[6,7] Pauling,[6] applying a twinning operation to periodically arranged atoms, was able to arrange ~ 2000 atoms in a unit cell and calculate a diffraction pattern close to that obtained from an icosahedral phase.[1] This approach is distinguished by the fact that at some stage a transition occurs from a quasiperiodic to a periodic structure.
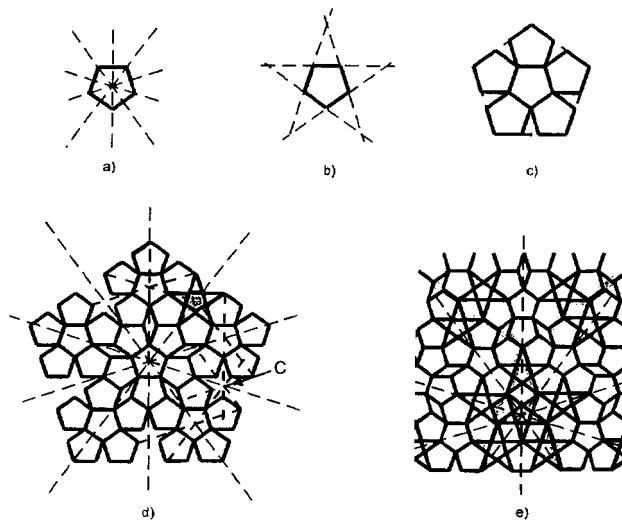
FIG. 1. Growth of a quasiperiodic packing of pentagons and stars with a global fivefold axis. Application of the operations ''opening of a flower.''

In the present letter a model of a quasicrystalline structure in two dimensions is constructed by means of reflection operations in the plane and rotation about a symmetry axis; the structure so obtained does not reduce to a periodic structure. Consider a tiling consisting of regular pentagons 5_τ and regular five-pointed stars Z_1 with equal edges. The ratio of the 5_τ edge length to the edge length of an interior pentagonal star Z_1, obtained by continuing the sides of the star, equals $\tau : 1$, where $\tau = (1 + \sqrt{5})/2 = 1.618$ is the golden mean. Figure 1d shows a structure which Mackay[5] has called a ''snowflake.'' The growth of this structure is accompanied by an increase in the pores between the pentagons and merging of the pores into figures with a large area. We shall construct a similar structure from pentagons and stars, and in the process we shall change the structure so that the pores in it are isolated. The construction is associated with the symmetry of a pentagon (Fig. 1a), characterized by the presence of a fivefold axis at the center and symmetry planes. If a pentagon 5_τ is subjected to simultaneous reflections in the five symmetry planes passing through its edges (Fig. 1b), then a structure which we shall term below a ''flower'' obtains (Fig. 1c). We shall call the operation forming a ''flower'' from a pentagon the ''opening of a flower.''

Such a ''flower'' can be generalized by continuing the outer edges of 5_τ until they intersect; the resulting figure can be called a generalized pentagon 5(I). Repeating the operation ''opening of a flower'' applied to 5(I), we obtain the ''snowflake'' of Ref. 5. The further development of the ''flower'' differs from the growth of ''snowflake,'' since the pores will be filled by a different mechanism. Note that a number of symmetry planes of the pentagons intersect at the point C (Fig. 1d): a) global planes — pentagons 5_τ, 5(I), 5(II); b) ''petals'' of the flower 5(II); c) petals of the flower 5(I), which is a petal of 5(II). By analogy to classical crystallography, it can be conjectured that a fivefold center of symmetry appears at this point. The action of this axis will give rise to the
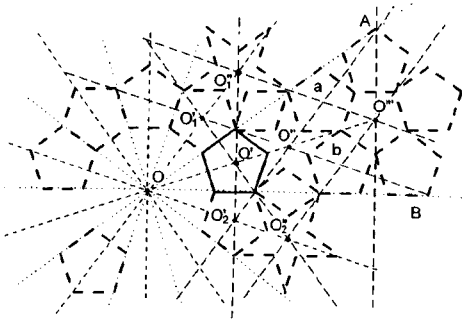
FIG. 2. Symmetry axes and planes operating during the growth of a quasiperiodic structure with a global tenfold axis.

formation of a star Z_1 at the location of a pore. The result of repeating the operation ''opening up of a flower'' on 5(II) and the action of the fivefold axis in the interpetal space will be a ring consisting of five stars (Fig. 1e). The space at the center is empty. It is logical to apply to it the operation opposite to ''opening of a flower'' (''closing of the flower''). This will produce a ''flower of stars,'' in the pores between whose petals pentagons 5_τ are now present. Repetition of the operation ''opening of a flower'' on 5(III) will engender between the petals a ''flower of a flower of stars'' in whose interpetal space a ''flower of 5_τ'' coinciding with 5(I), is formed. Therefore the processes by which a structure of pentagons and stars grows are intertwined. A similar structure with a star at the center (''flower of stars'') can also be obtained. For this, a star Z_1 is placed at the center of the structure and the operations ''opening of a flower'' are repeated. This process will be accompanied by a growth of the flower of 5_τ in the pores and will develop in a manner similar to the growth of a ''flower of stars'' in the pores of a ''flower of pentagons.''

The ''flower'' tiling can be used to form a structure with a tenfold global axis. Let the symmetry planes AO and BO, which engender 5_τ with centers O_1' and O_2', pass through two nonadjacent sides of a pentagon centered at O' (Fig. 2). The characteristic symmetry plane OO' of the initial pentagon and the planes AO and BO intersect at the point O. This intersection forms a global tenfold axis. Therefore, all elements located in the sector AOB automatically appear in other sectors of the surface. The characteristic symmetry planes of the pentagons centered at O_1' and O_2' ($O_1'O''$ and $O_2'O''$) intersect at the point O'' and produce at the point O'' a fivefold symmetry axis which operates mainly in the sector AOB. The action of this axis leads to the formation of a star of pentagons a and b. The characteristic symmetry planes $O_2''O'''$ and $O_1''O'''$ of stars centered at O_2'' and O_1'' in turn generate a fivefold symmetry axis at the point O'''. The action of this axis (similarly to the axis O'') inside the sector AOB is expressed in the appearance of a ring of five pentagons and also in the cloning of all figures relative to the planes AO''' and BO'''. The pentagon 5_τ centered at O''' is filled by an operation of the type ''closing of a flower.'' It should be noted that the elements of the structure are growing ''flowers'' of 5_τ and stars Z_1 (Fig. 3).

A quantitative analysis showed that the tilings obtained (''flower of 5_τ,'' ''flower of
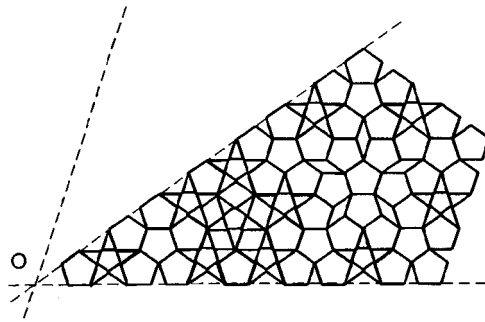
FIG. 3. Packing of pentagons and stars in the presence of a tenfold symmetry axis.

Z_1,'' structure with a tenfold axis) are characterized by the ratio of the number of elements that converge, with growth, to the same values. The pores in these packings are isolated and consist of two types of rhombi similar to those in the Penrose tiling — large (L) and small (S). The edges of the rhombi are equal to the edges of the pentagons 5_τ and the angles between the edges are equal to $2\pi/5$ (L) and $\pi/5$ (S). The ratios of the reciprocals of the total areas of the pentagons, stars, and L and S rhombi equal $S_5^{-1}:S_Z^{-1}:S_L^{-1}:S_S^{-1} = 1:(\tau^2 - 0.5):\tau^3:\tau^6$. The ratio of the number of pentagons and stars is $N_5:N_Z = \tau^2:1$. The pores comprise 16.54% of the area. The convergence of the real quantities to the indicated values is very slow: The error is $\sim 10^{-3}$% at a total number of pentagons $\sim 10^{20}$.

Attempts to describe the obtained structure by a decoration of the Penrose tiling were unsuccessful. At the same time, if a global center is made to coincide (in the case of the construction of a ''flower'' of 5_τ) with the center of symmetry of the first star with true (in the terminology of Ref. 5) fivefold symmetry axes of the Penrose tiling, marked in Fig. 4 by the dots, then all vertices of 5_τ and Z_1 will also be the vertices of the rhombi in the Penrose tiling. The points with the ''true'' fivefold symmetry of the Penrose tiling correspond to the vertices of a generalized large rhombus after five deflation operations.
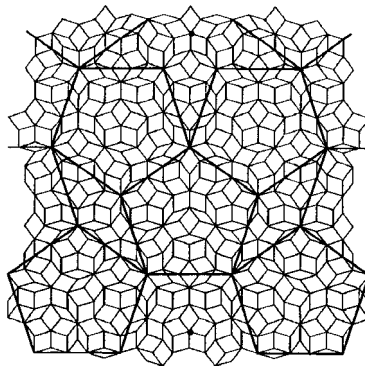

FIG. 4. Superposition of Penrose tiling on a ''flower of pentagons.''

In such a construction the edge of a pentagon 5_τ equals the sum of the short diagonal of the large rhombus and twice the long diagonal of the small rhombus. At the centers of the pentagons 5_τ aredecagons circumscribed around stars consisting of six rhombi with a center of the type $\langle 22222 \rangle^*$ and around figures with vertices $\langle 33121 \rangle$ and $\langle 4222 \rangle^*$, joined along the central large rhombus (the designations of the vertices in the Penrose tiling are taken from Henley's article[2]). The centers of the stars Z_1 will also be centers of the stars of large rhombi of the Penrose tiling of the type $\langle 22222 \rangle$ and $\langle 22222 \rangle^*$. Large rhombi will stand at the centers of all 5_τ and Z_1 edges, and the edges of the pentagons and stars will pass along the shortest diagonals of the rhombi.

Let us now note the characteristic features of the techniques used to construct structures consisting of pentagons and stars: 1) The symmetry operations operate on existing elements of the structure and engender new elements with which these operations can conflict (''opening of a flower''); 2) they engender new elements in free space without changing the old elements; and, 3) a local action is possible (symmetry axis, ''closing of a flower''). The first feature is not characteristic for the symmetry operations of classical crystallography. For example, it is evident that when the operation ''opening of a flower'' is used to pack honeycombs consisting of regular hexagons, the operative symmetry planes are intrinsic symmetry planes for the new elements. A very important property is that the symmetry operations include time as a parameter. The concept of ''a given point in time'' is at work. The growth process can be described only in terms which include the direction of time. Time reversal changes the essence of the symmetry operations.

Concentration nonuniformities of the structure grow along linear dimensions with each step of the growth of the structure, while the amplitude of these nonuniformities does not exceed the initial values (the maximum ratio of the pentagons and stars in 5(I) is $N_5:N_Z=30:5$ and the maximum density of stars in Z(I) is $N_Z:N_5=6:5$). In the case when this model works, the following characteristics of quasicrystals are possible: 1) The diffraction pattern formed by the scattering of radiation by surface atoms or atoms in the bulk will change slightly as the region of the crystal diffracting the radiation changes, and a decrease in the size of the crystallites will result in a redistribution of the intensity, and 2) in the case of a single crystal there should exist a weak diffraction pattern for scattering of radiation with wavelengths many times longer than the interatomic distance. An example is the diffraction of visible-range radiation accompanying reflection from crystal faces.

The ''flower'' motif is not the only motif in the construction of planar quasiperiodic structures by means of symmetry operations, but apparently it is the simplest. It is also possible to build by analogous principles structures of 5_τ and Z_1 in which a star is the main motif. A star of the next order will form in a manner such that its interior pentagon will consist of a single star Z_1 and fifteen pentagons 5_τ. The extension of the above operations of quasicrystal growth to three dimensions will result in the appearance of structural elements — two types of icosahedra, differing in size by a factor of τ. All icosahedra will have the same orientation. Neighboring icosahedra of the same size will share an edge, and their centers and the center of the edge will lie on the same line. Icosahedra of different size touch one another at the vertices, and once again their centers and the common vertex also lie on the same straight line. Three-dimensional structures

with a global fivefold or tenfold axes can be obtained, and the figures presented above can be interpreted as surfaces of section through these structures.

In Ref. 8 it is noted, in describing real (containing defects) and incommensurate crystals from the standpoint of modern crystallography, that the change in symmetry as compared with the ideal crystal lattice is manifested not as a decrease but rather as an increase in the degree of symmetry (in the case when the floral symmetry is taken into account, more than three dimensions are used to describe the properties, and a crystal is treated as a large molecule or cluster of atoms). As is well known, incommensurate crystals are often used as an analog of quasicrystals, so that it is not surprising that these characteristics are close to the structure described in this letter.

In closing, I wish to thank Academician N. A. Vatolin and Professor B. R. Gel'chinskiĭ for their encouragement and for a critical discussion of the material.

[a]e-mail: poliakov@physics.tu-chel.ac.ru

[1] D. Shechtman, I. Blech, D. Gratias, and J. W. Cahn, Phys. Rev. Lett. **53**, 1951 (1984).
[2] R. Penrose, Bull. Inst. Math. Appl. **10**, 266 (1974); C. L. Henley, Phys. Rev. B **34**, 797 (1986); F. Gähler, M. Baake, and M. Schlottmann, Phys. Rev. B **50**, 12548 (1994).
[3] P. A. Kalugin, A. Yu. Kitaev, and L. S. Levitov, JETP Lett. **41**, 145 (1985).
[4] N. G. de Bruijn, Ned. Akad. Weten. Proc. A **43**, 39 (1981); A **43**, 53 (1981); D. Levin and P. J. Steinhardt, Phys. Rev. B **34**, 596 (1986); J. E. S. Socolar and P. J. Steinhardt, Phys. Rev. B **34**, 617 (1986).
[5] A. L. Mackay, Kristallografiya **26**, 910 (1981) [Sov. Phys. Crystallogr. **26**, 910 (1981)].
[6] L. Pauling, Nature **317**, 512 (1985).
[7] N. A. Bul'enkov and V. S. Kraposhin, Pis'ma Zh. Tekh. Fiz. **19**(23), 1 (1993) [Tech. Phys. Lett. **19**, 739 (1993)].
[8] V. A. Koptsik, *Regularities in the Development of Complex Systems* [in Russian], Nauka, Leningrad, 1980.

Translated by M. E. Alferieff

From effective BCS action to vortex dynamics

G. E. Volovik

Low Temperature Laboratory, Helsinki University of Technology, 02150 Espoo, Finland;
L.D. Landau Institute for Theoretical Physics, Russian Academy of Sciences,
117940 Moscow, Russia

The topological term in the effective action for the electrically neutral BCS system is discussed. It is applied for the calculation of the transverse force acting on a vortex in the limit of a smooth vortex core and vanishing interlevel distance in the vortex core. The controversy between the topological terms in the articles by I. J. R. Aitchison *et al.*, Phys. Rev. B **51**, 6531 (1995) and A. van Otterlo *et al.*, cond-mat/9703124 is resolved. *© 1997 American Institute of Physics.* [S0021-3640(97)01508-9]

PACS numbers: 11.27.+d, 67.57.Fg, 74.20.Fg, 74.60.−w

1. INTRODUCTION

There have been many papers on the subject of the effective action for the BCS system. They differ in the topological terms: while in most of these papers the topological term is taken to be $n\dot{\phi}/2$, where n is the particle density and ϕ is the phase of the order parameter (see, e.g., Ref. 1), in a few papers it is taken as $(n-C_0)\dot{\phi}/2$, where $C_0 = p_F^3/3\pi^2$ is the particle density in the normal metal (see, e.g., Ref. 2). These different topological actions lead to different predictions for the transverse force acting on a moving vortex. Here we discuss this controversy.

Actually both actions give the correct hydrodynamic equations for the BCS system in the uncharged limit. This is because the difference between the topological actions is a total time derivative if the parameter C_0 is treated as a dynamical invariant. This means that both actions should lead to the same prediction for the vortex dynamics. However, this is contingent on proper treatment of the time derivative of the action. On the other hand, in the presence of a vortex the phase ϕ is not defined globally, which means that the topological action in terms of ϕ is ill-defined. That is why we propose another form of the topological term in the effective action, which does not contain the phase of the order parameter explicitly and which follows from the gradient expansion of the effective action.

This action allows us to find the transverse force acting on a vortex in the special limiting case in which the bosonic effective action provides a complete description of the vortex dynamics, i.e., in the case when the quantization of the levels in the vortex core can be neglected and the vortex core is smooth on the scale of the coherence length. In this limit our result for the transverse force coincides with that obtained in microscopic calculations.[3]

2. EFFECTIVE BCS ACTION AT $T=0$

The calculated topological term in the BCS action can be expressed in terms of the order parameter (gap function) Δ as

$$S_{\text{top}}=\frac{1}{2i}\int d^3r \int_0^1 d\tau \int_{-\infty}^{\infty} dt \frac{\partial n}{\partial(|\Delta|^2)}\left(\frac{\partial \Delta}{\partial t}\frac{\partial \Delta^*}{\partial \tau}-\frac{\partial \Delta}{\partial \tau}\frac{\partial \Delta^*}{\partial t}\right). \tag{1}$$

Here τ is an auxiliary coordinate introduced when the effective action $\text{Tr} \ln G^{-1}$ is represented as $\text{Tr} \int_0^1 d\tau G\partial_\tau G^{-1}$. The dependence on τ is chosen in such a way that at $\tau=0$ the coupling and the gap function are absent, $\Delta(\mathbf{r},t,\tau)|_{\tau=0}=0$, while $\tau=1$ corresponds to the physical $3+1$ dimensions, i.e., $\Delta(\mathbf{r},t,\tau)|_{\tau=1}=\Delta(\mathbf{r},t)$. In Eq. (1) n is the particle number density, which depends on Δ. At $\tau=0$ one has $n(\tau=0)=p_F^3/3\pi^2\equiv C_0$, which is the particle density in the absence of the gap at the same chemical potential.

The quantity $n-C_0$ is small in the weak-coupling limit of the BCS model, where it is determined by the particle–hole asymmetry, $n-C_0\sim n\Delta^2/E_F^2\ll n$. In a smooth crossover from the BCS superconductivity to the condensate of the Cooper pairs, discussed in many papers (see the recent papers[4–6], the parameter C_0 decreases and can become zero at some value of the coupling parameter g: $C_0(g)=0$ at $g>g_c$. In this case at $g=g_c$ one has the quantum (Lifshitz) transition at $T=0$. This zero-temperature transition definitely happens if the quasiparticle spectrum has nodes, e.g., in the case of the d-wave Cooper pairing or in the p-wave state with the symmetry of the A phase of superfluid ^{3}He. In this case at $g=g_c$ the spectrum of quasiparticles is reconstructed — the nodes disappear (see Secs. 6.2 and 9.4 in Ref. 7). This is similar to the Lifshitz transition in metals, where the topology of Fermi surface changes. In what follows we assume that we are on the BCS (weak-coupling) side, i.e., below the Lifshitz point, $g<g_c$.

In the BCS action the relevant variable is the gap function Δ, which means that all other variables, including n are the functions of $|\Delta|^2$. The variation of the action over the order parameter is the surface integral in the 5-dimensional space $(\mathbf{r},\tau,t)$ and thus is expressed in terms of the physical coordinates $(\mathbf{r},t)$:

$$\delta S_{\text{top}}=\frac{1}{2i}\int d^3r \int_{-\infty}^{\infty} dt \frac{\partial n}{\partial(|\Delta|^2)}\left(\frac{\partial \Delta}{\partial t}\delta\Delta^*-\delta\Delta\frac{\partial \Delta^*}{\partial t}\right). \tag{2}$$

In principle from the variation of this topological action one can recover the action in the physical space–time, but the well-defined action explicitly contains the parameter $C_0=n(|\Delta|^2=0)=p_F^3/3\pi$:

$$S_{\text{top}}=\frac{1}{4i}\int d^3r \int_{-\infty}^{\infty} dt(n-n(|\Delta|^2=0))\left(\frac{\dot{\Delta}^*}{\Delta^*}-\frac{\dot{\Delta}}{\Delta}\right). \tag{3}$$

If $\Delta(\mathbf{r},t)$ is nowhere zero (this requirement excludes the case when vortices are present) one can introduce the phase ϕ of the order parameter:

$$\Delta=|\Delta|e^{i\phi}. \tag{4}$$

This allows one to express the variation of the topological action in Eq. (2) in terms of the canonically conjugate variables n and ϕ:

$$\delta S_{\text{top}} = \frac{1}{2} \int d^3r \int_{-\infty}^{\infty} dt \left(\frac{\partial n}{\partial t} \delta\phi - \frac{\partial \phi}{\partial t} \delta n \right), \tag{5}$$

where

$$\delta n = \frac{\partial n}{\partial(|\Delta|^2)} \delta(|\Delta|^2). \tag{6}$$

The action in Eq. (3) can be also used in this case, it gives

$$S_{\text{top}} = -\frac{1}{2} \int d^3r \int_{-\infty}^{\infty} dt (n - C_0) \frac{\partial \phi}{\partial t}. \tag{7}$$

This is what was obtained in Ref. 2.

The conventional contribution to the action is

$$S_0 = \int d^3r \int_{-\infty}^{\infty} dt \left(\frac{1}{2} m n_s \mathbf{v}_s^2 + \epsilon(|\Delta|^2) \right), \tag{8}$$

where n_s is the superfluid density, m is the mass of the fermion, $\mathbf{v}_s = (\hbar/2m) \nabla \phi$ is the superfluid velocity, and ϵ is the energy density, which depends on $|\Delta|^2$. Varying $S = S_0 + S_{\text{top}}$ over ϕ and $|\Delta|^2$ gives the conventional hydrodynamic equations (we have neglected the nonlinear terms in this procedure)

$$\frac{\partial n}{\partial t} + \nabla \cdot (n_s \mathbf{v}_s) = 0, \tag{9}$$

$$\frac{\partial \phi}{\partial t} = -2\mu, \quad \mu = \frac{\partial \epsilon / \partial(|\Delta|^2)}{\partial n / \partial(|\Delta|^2)}. \tag{10}$$

It is important here that the hydrodynamic equations are general and do not contain the parameter C_0. This is because the term containing the factor C_0 in Eq. (7) is a total derivative. In this sense there is no difference between the topological terms discussed in Refs. 1 and 2. The difference becomes important when zeroes appear in Δ and the phase of the order parameter is no longer defined globally. This is the case with vortices. To find the vortex dynamics we must return to the action in Eq. (2) for the order parameter, which does not contain the phase ϕ explicitly.

3. EFFECTIVE ACTION FOR THE VORTEX DYNAMICS IN CONTINUOUS LIMIT

The effective action $S = S_0 + S_{\text{top}}$ can be used in the derivation of the dynamics of a vortex line only under certain conditions. We assume that the description in terms of the order parameter is complete, i.e., there are no other degrees of freedom. All the fermionic degrees of freedom are assumed to have been integrated out when the effective action was obtained. In this integration the fermionic spectrum is treated classically, i.e., the spectrum is taken as a function of commuting spatial coordinate $\mathbf{r}$ and momentum $\mathbf{p}$: $E = \sqrt{\varepsilon^2(\mathbf{p}) + |\Delta(\mathbf{r})|^2}$. This means that if one applies this effective action to vortices one neglects the quantization of the fermions in the vortex background. This is justified only when the distance between the energy levels is small compared to the width of the levels,

$\omega_0\tau \ll 1$. This is a necessary condition for application of the effective action to the vortex motion. Another important condition is that the core size of the vortex must be large compared to the coherence length so that one can neglect the higher-order gradient terms in the action.

Under these conditions we can show that the BCS effective action leads to the following equation of motion for the vortex:

$$\pi N\hbar (n - C_0)\hat{z}\times \mathbf{v}_L = \pi N\hbar n_s \hat{z}\times \mathbf{v}_{s0}. \qquad (11)$$

Here $\mathbf{v}_L$ is the vortex velocity with respect to the heat bath (normal component or crystal lattice), which is here assumed to be at rest; $\mathbf{v}_{s0}$ is the superfluid velocity of the external superflow; N is the winding number of the vortex. This agrees with the result of microscopic calculations[3] for the electrically neutral case in the limit of large core size and in the regime $\omega_0\tau \ll 1$.

To get Eq. (11) from the BCS action, let us introduce the vortex coordinate $\mathbf{r}_L(t)$. For simplicity we consider a rectilinear vortex along the z axis, so the order parameter Δ depends only on $\mathbf{r} - \mathbf{r}_L(t)$, where both vectors are 2-dimensional:

$$\Delta(\mathbf{r},t) = \Delta(\mathbf{r} - \mathbf{r}_L(t)). \qquad (12)$$

The variation of the topological action in Eqs. (2) and (3) becomes

$$\delta S_{\text{top}} = \frac{1}{2i}\int d^3 r \frac{\partial n}{\partial (|\Delta|^2)}\left(\frac{\partial \Delta}{\partial x}\frac{\partial \Delta^*}{\partial y} - \frac{\partial \Delta}{\partial y}\frac{\partial \Delta^*}{\partial x}\right)\int_{-\infty}^{\infty} dt\left(\frac{\partial x_L}{\partial t}\delta y_L - \delta x_L\frac{\partial y_L}{\partial t}\right). \qquad (13)$$

For an axisymmetric vortex with

$$\Delta(r,\varphi) = a(r)e^{iN\varphi}, \qquad (14)$$

where r and φ are cylindrical coordinates and N is the winding number, one obtains

$$-i\int d^3 r \frac{\partial n}{\partial (|\Delta|^2)}\left(\frac{\partial \Delta}{\partial x}\frac{\partial \Delta^*}{\partial y} - \frac{\partial \Delta}{\partial y}\frac{\partial \Delta^*}{\partial x}\right) = 2\pi NL\int_0^{\infty} dr\frac{\partial n}{\partial r} = 2\pi NL(n(\infty) - n(0))$$

$$= 2\pi NL(n - C_0), \qquad (15)$$

where L is the length of the straight vortex line. We took into account that on the vortex axis ($r=0$) the order parameter is zero, $a(0)=0$, and therefore $n(0)=C_0$.

The same result can be obtained for any type of vortex with winding number N, because the volume integral can be transformed to a surface integral far from the vortex core, the outcome of which depends only by N and $n(|\Delta(\infty)|^2) - n(|\Delta|^2 = 0) = n - C_0$. As a result

$$\delta S_{\text{top}} = \pi\hbar NL(n - C_0)\int_{-\infty}^{\infty} dt\left(\frac{\partial x_L}{\partial t}\delta y_L - \delta x_L\frac{\partial y_L}{\partial t}\right). \qquad (16)$$

The variation of this topological action over $\delta\mathbf{r}_L$ gives the force acting on the vortex, which is represented by the term on the left-hand side of Eq. (11).

Note that the expression for the variation of Eq. (2):

$$\frac{\delta S_{\text{top}}}{\delta \mathbf{r}_L} = \frac{1}{2i} \int d^3 r \frac{\partial n}{\partial(|\Delta|^2)} \left(\frac{\partial \Delta}{\partial t} \nabla \Delta^* - \nabla \Delta \frac{\partial \Delta^*}{\partial t} \right) \tag{17}$$

transforms to Eq. (10) of Ref. 3 if one neglects the coordinate dependence of $\partial n / \partial(|\Delta|^2)$. That approximation is justified only in the weak-coupling limit, $g \ll 1$, explored in Ref. 3, while our approach is not limited by the weak-coupling assumption: we assume only that $g < g_c$.

In Ref. 8 the Eq. (10) of Ref. 3 is generalized to the case of anisotropic pairing with a momentum-dependent gap function $\Delta(\mathbf{p}, \mathbf{r})$, but still in the weak-coupling limit. We can generalize this to the arbitrary coupling strength by introducing a momentum-dependent particle distribution function

$$n(\mathbf{p}, \mathbf{r}) = \frac{1}{2} \left(1 - \frac{\varepsilon(\mathbf{p})}{\sqrt{\varepsilon^2(\mathbf{p}) + |\Delta(\mathbf{p}, \mathbf{r})|^2}} \right), \quad n(\mathbf{r}) = 2 \int \frac{d^3 p}{(2\pi)^3} n(\mathbf{p}, \mathbf{r}). \tag{18}$$

Then

$$\delta S_{\text{top}} = -i \int \frac{d^3 p \, d^3 r}{(2\pi)^3} \int_{-\infty}^{\infty} dt \frac{\partial n(\mathbf{p}, \mathbf{r})}{\partial(|\Delta(\mathbf{p}, \mathbf{r})|^2)}$$

$$\times \left(\frac{\partial \Delta(\mathbf{p}, \mathbf{r})}{\partial t} \delta \Delta^*(\mathbf{p}, \mathbf{r}) - \delta \Delta(\mathbf{p}, \mathbf{r}) \frac{\partial \Delta^*(\mathbf{p}, \mathbf{r})}{\partial t} \right). \tag{19}$$

Applying the same procedure as before, one obtains Eq. (16) for any (smooth) structure of the vortex core and for arbitrary anisotropic pairing state.[a]

The term on the right-hand side of Eq. (11) is obtained from the kinetic energy term in S_0 in Eq. (8). In the presence of an external superflow $\mathbf{v}_{s0}$ the relevant term is

$$\mathbf{v}_{s0} \cdot \int d^3 r \, n_s \mathbf{v}_s = \mathbf{v}_{s0} \cdot \mathbf{P}. \tag{20}$$

The linear momentum $\mathbf{P}$ related to the vortex coordinate is

$$\mathbf{P} = \pi \hbar N n_s L \hat{z} \times \mathbf{r}_L. \tag{21}$$

The variation of $\mathbf{v}_{s0} \cdot \mathbf{P}$ over $\mathbf{r}_L$ gives the second term in Eq. (11).

Equation (11) is not Galilean invariant. Galilean invariance is restored by introducing the velocity of the normal component $\mathbf{v}_n$, which coincides with the velocity of crystal lattice in the case of superconductors or with the heat bath of the normal excitations in the case of superfluids. This equation can be represented as the balance of three forces acting on the vortex:[10]

$$\pi \hbar N \hat{z} \times [n(\mathbf{v}_s - \mathbf{v}_L) + C_0(\mathbf{v}_L - \mathbf{v}_n) + (n - n_s)(\mathbf{v}_n - \mathbf{v}_s)] = 0. \tag{22}$$

These are, respectively, the Magnus, spectral-flow, and Iordanskii forces in the terminology of Ref. 10.

A force balance of the form in Eq. (11) was also obtained in Ref. 11, again in the limit $\omega_0 \tau \ll 1$; the first discussion of the term on the left-hand side of Eq. (11) as originating from the topological action was probably given in Ref. 12 (see the paragraph containing (10) in Ref. 12).

4. DISCUSSION

The effective topological actions discussed in Refs. 1 and 2 are equivalent to each other in the particular case when the phase of the condensate is defined globally, and thus in the absence of vortices. In this case the two topological actions differ by a total time derivative and thus lead to the same hydrodynamic equations for the conjugate variables — the particle density n and the condensate phase ϕ. However these actions cannot be used when zeroes are present in the order parameter. In the presence of zeroes the topological action in Eqs. (2) and (3) (or in Eq. (19) for the more general case of anisotropic pairing) is to be used; this settles the controversy between the aforementioned actions[1,2] in favor of that in Ref. 2.

Equations (2) and (3) also describe the vortex dynamics in a special limiting case. This dynamics agrees with the general phenomenological approach using the Poisson brackets scheme.[13] In this approach the phenomenological parameter C_0 is introduced as the dynamical invariant of the system, which does not violate the general properties of the hydrodynamical Poisson brackets. The BCS effective action for the neutral BCS system in Eqs. (2) and (3) gives the precise value of this phenomenological parameter, $C_0 = p_F^3 / 3\pi^2$, in the regime in which the action is applicable to the vortex dynamics. The conditions of applicability are $\omega_0 \tau \ll 1$ and $R_{\text{core}} \gg \xi_0$, where R_{core} is the core radius. They correspond to a vortex with a smooth core.

In the opposite limit $\omega_0 \tau = \infty$ the effective action for the vortex dynamics in the BCS system can also be derived from first principles by examining the Berry phase (see the recent paper[14]). In this case the discrete spectrum of the electrons in the core is of prime importance. The properties of the exact wave functions of the electron in the potential produced by the vortex lead to a zero value of the canonical momentum density at the origin, $S(0) = 0$, in Ref. 14. This gives a value of zero for the parameter C_0 in Eq. (22), in complete agreement with the result of Ref. 10, obtained in the limit $\omega_0 \tau = \infty$. The finite lifetime τ destroys the coherence of the wave functions and finally restores the maximal value of C_0 in the limit $\omega_0 \tau \ll 1$.

[a]I am indebted to N. B. Kopnin[9] for this remark.

[1] I. J. R. Aitchison, P. Ao, D. J. Thouless, and X. -M. Zhu, Phys. Rev. B **51**, 6531 (1995).
[2] A. van Otterlo, D. S. Golubev, A. D. Zaikin, and G. Blatter, Cond-mat/9703124.
[3] N. B. Kopnin, Phys. Rev. B **54**, 9475 (1996).
[4] V. B. Geshkenbein, L. B. Ioffe, and A. I. Larkin, Phys. Rev. B **55**, 3173 (1997).
[5] S. Stintzing and W. Zwerger, Cond-mat/9703129.
[6] M. Marini, F. Pistolesi, and G. C. Strinati, Cond-mat/9703160.
[7] G. E. Volovik, *Exotic Properties of Superfluid* ^{3}*He*, World Scientific, Singapore–New Jersey–London–Hong Kong, 1992.

[8] N. B. Kopnin and A. V. Lopatin, to be published in Phys. Rev. B.

[9] N. B. Kopnin, private communications.

[10] N. B. Kopnin, G. E. Volovik, and Ü. Parts, Europhys. Lett. **32**, 651 (1995).

[11] A. van Otterlo, M. V. Feigelman, V. B. Geshkenbein, and G. Blatter, Phys. Rev. Lett. **75**, 3736 (1995).

[12] G. E. Volovik, JETP Lett. **44**, 185 (1986).

[13] G. E. Volovik, JETP Lett. **64**, 845 (1996).

[14] J. Dziarmaga, Phys. Rev. B **53**, 6572 (1996).

Electronic structure of linear chains of fullerenes

V. A. Levashov, A. A. Remova, and V. R. Belosludov[a]

Institute of Inorganic Chemistry, Siberian Branch of the Russian Academy of Sciences, 630090 Novosibirsk, Russia

The band structure of linear chains of fullerene molecules is calculated as a function of the intermolecular π-electron overlap integral T, which increases under increasing external pressure. Chains consisting of neutral (C_{60}) and charged (C_{60}^{-}) molecules are studied. It is shown that there is a sharp transition from a metal (or narrow-gap semiconductor) to an insulator (with band gap ~ 1 eV) with increasing T. The proposed model makes it possible to describe the formation of solid-carbon structures, containing chains of covalently bound fullerene molecules, with different pressure-dependent semiconductor properties. © *1997 American Institute of Physics.* [S0021-3640(97)01608-3]

PACS numbers: 61.48.+c, 71.20.Tx

Linear chains of fullerenes were recently discovered in A_1C_{60} compounds (A = K, Rb, Cs, Na_2Cs, Na_2Rb).[1–6] Phase transitions with a change of lattice symmetry are observed in these structures. In the orthorhombic phase the distance between the centers of the molecules in the direction of the crystallographic vector **a** equals only 9.1–9.3 Å. It is conjectured that the fullerene molecules form in this direction a polyanion chain with covalently bound C_{60}^{-} molecules. It is believed that the polymer bond in polyanion A_1C_{60} chains forms if the midpoint of the two closest parallel double bonds belonging to neighboring molecules falls on the intermolecular axis; the π electron orbitals of the two closest pairs of carbon atoms form an intermolecular overlap. The observation of identically oriented linearly polymerized neutral C_{60} molecules in the solid phase was recently reported. Such chains are formed in amorphous fullerite structures at high pressures and temperatures.[7–10] The details of the mechanism of formation of the polymer chains have not been adequately studied.

It is well known that the rigid-band model describes poorly the electronic structure of compounds of the type A_xC_{60} ($x = 1, 2, 3, 4$), where A is an alkali-metal atom. One reason for this could be the electron–phonon interaction. The band structure of fullerides reflects primarily the molecular structure of the highly symmetric C_{60}. Since the threefold degenerate t_{1u} level forms the conduction band of A_xC_{60} compounds, the Jahn–Teller effect should play a fundamental role here.[11]

The calculations were performed in a model proposed by Su, Schrieffer, and Heeger (SSH),[12] in which hops of the π electrons between neighboring carbon atoms are studied and the local electron–phonon interaction is treated in an adiabatic approximation. This approach was used in Ref. 13 to calculate the spectrum of an isolated fullerene molecule, and it was also shown that the formation of ''long'' and ''short'' bonds between the

carbon atoms on the surface of the C_{60} molecule could be due to the electron–phonon interaction. It is conjectured that the σ electrons do not directly affect the optical and chemical properties, but they do provide a bond between the carbon atoms on the surface of C_{60}, determining the energy of elastic deformation of the bonds.

In a previous work we extended this model to the case of fulleride crystals.[11] Besides intramolecular electronic transitions, intermolecular transitions between the nearest atoms to the neighboring molecules were also introduced. The main objective of present work was to study the behavior of the valence (h_u) and conduction (t_{1u}) bands as a function of the intermolecular overlap integral for neutral linearly polymerized C_{60} molecules in the amorphous phase and for polyanionic chains A_1C_{60} in the orthorhombic phase.

The interaction between the chains is assumed to be weak, and charge transfer from the alkali-metal atoms to the molecules is assumed to be complete. Furthermore, we neglect the electron–electron correlations. The interaction of the electrons with the intermolecular vibrations is weak compared with the intramolecular interactions, since the mass of the molecule is much greater than the mass of the carbon atom. The SSH Hamiltonian is given in the form[11–13]

$$H = H_{\text{ph}} + H_{\text{el,el–ph}}, \tag{1}$$

$$H_{\text{el,el–ph}} = -\sum_m \sum_{\langle l,l'\rangle s} (t - \alpha \rho_{ll'}^m) c_{l,s}^{m+} c_{l',s}^m - T \sum_{\langle mn,m'n'\rangle s} c_{n,s}^{m+} c_{n',s}^{m'} + \text{h.c.}, \tag{2}$$

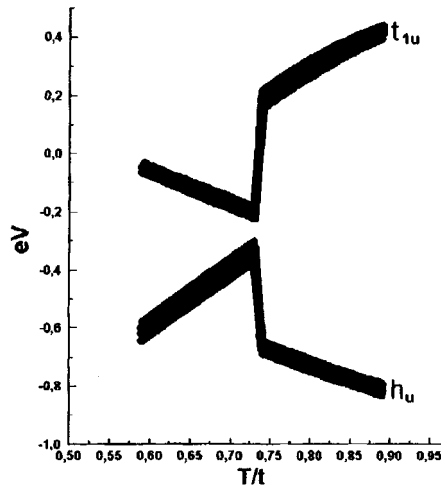$$H_{\text{ph}} = \frac{\kappa}{2} \sum_m \sum_{\langle l,l'\rangle} (\rho_{ll'}^m)^2. \tag{3}$$

FIG. 1. Energy characteristics as a function of T for C_{60}. T and t — inter- and intramolecular overlap integrals of π electrons. The t_{1u} band in eV — conduction band, h_u — valence band.
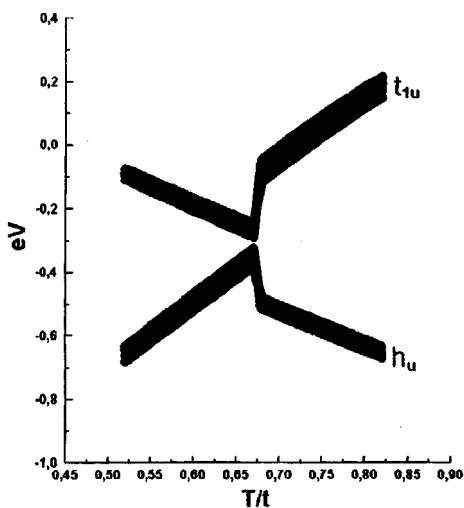
FIG. 2. Same as Fig. 1, for charged C_{60}^- molecules.

Here the operator $c_{l,s}^{m+}$ creates an electron with spin s at the lth carbon atom belonging to the mth molecule, and T and t are intermolecular and intramolecular ''hopping'' integrals, determined by the overlap of the π-electron clouds of the nearest carbon atoms. The term proportional to α reflects the dependence of the intramolecular overlap on the change in bond length $\rho_{ll'}^m$ between the nearest carbon atoms l and l' in the mth molecule. As a result of translational invariance, $\rho_{l,l'}^m = \rho_{l,l'}$. The calculations were performed for the following values of the parameters: $t = 2.1$ eV, $\alpha = 6.0$ eV/Å, $\kappa = 52.5$ eV/Å^2 (Ref. 14); T was varied from $0.5t$ to $0.9t$.

The computational results for the Jahn–Teller distortions and the electron density distribution on the surface of molecules in a chain as a function of the intermolecular overlap integral T were presented in Ref. 14. It was shown that there exists a critical value T^* for which a redistribution of the electron density on the C_{60} surface occurs: $T^*/t \cong 0.74$ for neutral chains and $T^*/t \cong 0.68$ for charged chains.

The energy characteristics of the valence and conduction bands as a function of T for neutral and polyanionic chains are displayed in Fig. 1 and 2, respectively. For both the neutral and polyanionic chains the position of the valence and conduction bands is a nonmonotonic function of T, and their widths, remaining small ($\cong 0.5$ for both C_{60} and C_{60}^-), change very little. The bands closest to those under study do not overlap with them and are separated from them by an energy interval of the order of 1 eV near T^*. The threefold degeneracy of the t_{1u} level is completely lifted. In the limit $T \to T^*$ the band gap $\Delta \cong 0.5$ eV for C_{60}. For C_{60}^- the valence h_u and conduction t_{1u} bands merge. As the molecules come closer to one another (T increases), the band gap changes abruptly at the point T^* ($\Delta \cong 0.80$ eV for neutral chains and $\Delta \cong 0.35$ eV for charged chains). If T continues to increase in the above-indicated range, then the band gap will also increase. The decrease in Δ as $T \to T^*$ is a consequence of the one-dimensional character of the investigated periodic structures, when many degrees of freedom are present at one site of

a one-dimensional lattice, while the abrupt change in the band gap at $T=T^*$ is due to the Jahn–Teller effect. Having attributed the increase in the parameter T to the increase in pressure, it is natural to conclude that a transition of from a narrow-gap semiconductor to an insulator occurs in solid C_{60} at some pressure. The rapid increase in the band gap at pressures above some critical value indicates the possibility that strong covalent bonds are formed between the C_{60} molecules in a chain. Therefore the model makes it possible to describe the high-pressure formation of solid-hydrogen structures containing chains of covalently bound fullerene molecules and exhibiting different semiconductor properties. These properties can be varied by changing the pressure.

[a]e-mail: bel@casper.che.nsk.su

[1] P. W. Stephens, G. Bortel, G. Faigel et al., Nature **370**, 636 (1994).
[2] L. Granasy, S. Pekker, and L. Forro, Phys. Rev. B **53**, 5059 (1996).
[3] C. Michael, D. Koller, A. Rosenberg et al., Phys. Rev. B **51**, 3210 (1995).
[4] O. Chauvet, G. Oszlanyi, L. Forro et al., Phys. Rev. Lett. **72**, 2721 (1994).
[5] Q. Zhu, Phys. Rev. B **52**, R723 (1995).
[6] V. A. Aksenov, Yu. A. Osip'yan, and V. S. Shakhmatov, JETP Lett. **64**, 120 (1996).
[7] V. V. Brazhkin, A. G. Lyapin, and S. V. Popova, JETP Lett. **64**, 802 (1996).
[8] H. Hirai and K. Kongo, Phys. Rev. B **51**, 15555 (1995).
[9] V. A. Davydov, L. S. Kashevarova, A. V. Rakhmanina et al., JETP Lett. **63**, 818 (1996).
[10] V. D. Blank, B. A. Kulnitskiy, and Ye. V. Tatyanin, Phys. Lett. A **204**, 151 (1995).
[11] A. Remova, V. P. Shpakov, U-H. Paek et al., Phys. Rev. B **52**, 13715 (1995).
[12] W. P. Su, J. R. Schrieffer, and A. J. Heeger, Phys. Rev. B **22**, 2099 (1980).
[13] K. Harigaya, Phys. Rev. B **45**, 13676 (1992).
[14] V. A. Levashov, A. A. Remova, and V. R. Belosludov, JETP Lett. **64**, 567 (1996).

Translated by M. E. Alferieff

Thermal conductivity of crystalline fullerite C$_{60}$ in the simple cubic phase

V. B. Efimov, L. P. Mezhov-Deglin, and R. K. Nikolaev

Institute of Solid-State Physics, Russian Academy of Sciences, 142432 Chernogolovka, Moscow District, Russia

The behavior of the thermal conductivity $k(T)$ of bulk faceted fullerite C$_{60}$ crystals is investigated at temperatures $T = 8$–220 K. The samples are prepared by the gas-transport method from pure C$_{60}$, containing less than 0.01% impurities. It is found that as the temperature decreases, the thermal conductivity of the crystal increases, reaches a maximum at $T = 15$–20 K, and drops by a factor of ~ 2, proportional to the change in the specific heat, on cooling to 8 K. The effective phonon mean free path λ_p, estimated from the thermal conductivity and known from the published values of the specific heat of fullerite, is comparable to the lattice constant of the crystal $\lambda_p \sim d = 1.4$ nm at temperatures $T > 200$ K and reaches values $\lambda_p \sim 50d$ at $T < 15$ K, i.e., the maximum phonon ranges are limited by scattering on defects in the volume of the sample in the simple cubic phase. In the range $T = 25$–75 K the observed temperature dependence $k(T)$ can be described by the expression $k(T) \sim \exp(\Theta/bT)$, characteristic for the behavior of the thermal conductivity of perfect nonconducting crystals at temperatures below the Debye temperature Θ ($\Theta = 80$ K in fullerite), where umklapp phonon–phonon scattering processes predominate in the volume of the sample. © *1997 American Institute of Physics.*
[S0021-3640(97)01708-8]

PACS numbers: 61.48.+c, 72.80.Rj

It is well known[1] that at normal temperatures and pressures C$_{60}$ molecules form crystals with a highly symmetric face-centered cubic structure (fcc) in which the molecules located at the vertices of a cube rotate freely. Below the "orientational melting" point $T_m \sim 260$ K crystalline fullerite passes into a simple cubic (sc) phase consisting of four cubic sublattices distinguished by the relative orientation of the C$_{60}$ molecules (the unit cell contains four molecules). Experimental observations have shown that the strong scatter in the results obtained in investigations of the thermodynamic properties of C$_{60}$ is due to both the difference in the degrees of purity and perfection as well as the effect of thermal cycling on the properties of the samples: the fcc–sc phase transition can result in the formation of defects in the volume of the sample under the action of thermoelastic stresses generated during thermal cycling (see Refs. 2 and 3 and the references cited therein). Orientational defects (a local disorientation of the neighboring molecules in the crystal lattice), produced as a result of the thermal vibrations of the molecules, could be

an additional source of quasiparticle scattering in a crystal in the sc phase.[4] For this reason, the properties of samples of greater perfection and purity must be investigated experimentally over a wide range of temperatures below room temperature, where the intramolecular interactions can be neglected, in order to draw reliable conclusions about the characteristic behavior of the transport coefficients and about the role of different excitation relaxation mechanisms in the fullerite lattice.

This letter reports and discusses the results of investigations of the thermal conductivity of bulk (volume ~ 3 mm^3) faceted fullerite C_{60} crystals prepared by the gas-transport method from material of high purity, containing less than 0.01% impurities in the initial powder. The measurements were performed at temperatures $T = 8$–220 K, i.e., in the existence region of the sc phase. These are the first investigations of the thermal conductivity of C_{60} crystals below 30 K. Lowering the minimum temperature of the measurements by a factor of ~ 4 made it possible to observe the appearance of a maximum in the curve $k(T)$ in the region $T = 20$–15 K and the subsequent drop in the thermal conductivity at temperatures below 15 K. Comparing with the results of previous investigations of the thermal conductivity of crystals prepared from material containing $\sim 0.5\%$ impurities[4] showed that the many-fold increase in the purity and, apparently, the degree of perfection of the experimental samples substantially changed the temperature dependence of the thermal resistance $k^{-1}(T)$ at temperatures below the Debye temperature $\Theta = 80$ K: from linear in Ref. 4 to nearly exponential in the region $T = 75 - 25$ K in our sample. However, it was found that even in such a crystal the effective phonon mean free path λ_p at temperatures below the point of the maximum of the thermal conductivity is much shorter than the linear dimensions of the sample, $\lambda_p \lesssim 10^{-4}$ mm, i.e., the maximum values of the thermal conductivity in the experimental crystal are limited by scattering on defects in the volume of the sample.

SAMPLE PREPARATION AND MEASUREMENT PROCEDURE

Fullerite single crystals were grown from the gas phase by the method described in Ref. 7, for example. Powder containing 99.99% C_{60} was used as the initial material. To remove volatile impurities, the powder was held for several hours at a temperature of 250 °C in a dynamic oil-free vacuum, after which vacuum sublimation was performed three times. This yielded small C_{60} crystals, which were placed into a quartz ampul, 10 mm in diameter and 150 mm long, which was evacuated to a pressure of $1 \cdot 10^{-6}$ torr and sealed. The crystals were grown in a horizontal furnace with two temperature gradients under the following conditions: The sublimation temperature was equal to 550 °C and the crystallization temperature was equal to 530 °C. The growth time of the crystals with linear dimensions of up to 3 mm was equal to 8–10 h. This made it possible to prepare faceted fcc single crystals with a volume of ~ 3 mm^3.

The thermal conductivity was measured by the stationary heat-flux method. The temperature difference along the sample was measured with a Chromel–Constantan thermocouple. The wires of the thermocouple were 10 μm in diameter and the contacts were separated by a distance of the order of 1 mm. The thermocouples and the heater were glued to the sample with IBM lacquer, which possesses a high thermal conductivity and is easily removed with a solvent consisting of 50% methanol + 50% toluene.
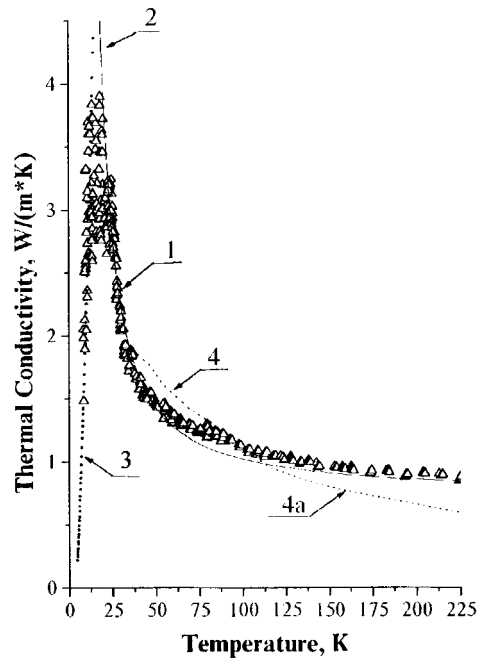
FIG. 1. Thermal conductivity of a fullerite crystal. Dots *1* — results of our measurements. Solid curve *2* — exponential dependence $k(T)$. The computed curve *3* describes the dependence $k(T) \sim C(T)$. Curve *4* — thermal conductivity of the crystal investigated in Ref. 4.

The average rate of cooling (heating) of a sample was ~ 0.1–0.05 K/min. The typical values of the temperature difference along the sample with the heater switched on did not exceed 2 K at 100 K and were less than 1 K at temperatures $T < 20$ K.

MEASUREMENT RESULTS AND DISCUSSION

1. Experimental data. The measurements of the thermal conductivity of the crystals were performed mainly on two samples. The behavior of the thermal conductivity of the best experimental crystal is shown in Fig. 1. The points *1* correspond to measurements obtained both during cooling from room to liquid-helium temperature and during the subsequent heating of the sample from liquid-helium temperatures. It was found that, in contrast to the observations in Refs. 2 and 3, thermal cycling in the range from liquid-helium to liquid-nitrogen temperatures does not cause a systematic decrease in the maximum values of thermal conductivity k_{max} as a result of the accumulation of defects in the sample. We attribute the large cycle-to-cycle scatter in the values of the different sets of experimental points near k_{max} mainly to the inadequate insensitivity of the thermocouple at temperatures $T < 30$ K. The temperature dependence $k(T)$ of the second sample investigated in the temperature range from room to liquid-nitrogen temperatures is close to that shown in Fig. 1.

The solid curve *2*, drawn through the experimental points in the interval 25–75 K, and the dotted curve *3* correspond to the dependences $k(T) = A \exp(\Theta/bT)$ and

$k(T) = D \cdot C(T)$. Here $\Theta = 80$ K is the Debye temperature of fullerite[5,6] and $b = 2.5$ is a numerical parameter. The values of the numerical parameters A, b, and D were found by fitting the computed curves *2* and *3* to the experimental points. In constructing the curve *3*, which corresponds to the behavior of the thermal conductivity $k(T)$ of the crystal at a constant phonon mean free path $\lambda_p = $ const, we employed the results of recent measurements by Pal'nichenko of the specific heat $C(T)$ of a C_{60} crystal from the same batch as our samples. The new data agree with the temperature dependences $C(T)$ in the less pure samples.[5,6] We note that the parameter $b = 2.5$ agrees well with the Peierls theory estimates of the probability of umklapp phonon–phonon scattering processes in an ideal crystal at temperatures $T < \Theta$.[8,9]

The effective phonon mean free path $\lambda_p(T)$ in the experimental crystal can be estimated from the measured thermal conductivity $k(T)$, using the values of $C(T)$ and the average sound velocity $v \sim 3.5 \cdot 10^3$ m/s, which are known from different experiments,[2,3,5,6]

$$\lambda_p = 3k(T)/C(T)v. \tag{1}$$

It was found that the values so obtained for λ_p at $T > 200$ K are close to the lattice constant of the crystal $d = 1.4$ nm and increase to $\lambda_p \approx 50d$ at temperatures below the maximum of the thermal conductivity of the sample $T < 15$ K. The difference in the numerical estimates of λ_p in the present work and in Ref. 4 ($\lambda_p \sim 3d$ and $T \lesssim 260$ K) is due to the difference in the choice of the values of C and v. However, the differences of the approaches to estimating λ_p do not change the main point: *First, these estimates confirm the importance of using the phonon (Debye) model for describing mechanisms of heat transfer in the sc phase of C_{60} crystals, and, second, they show that the maximum phonon ranges in the experimental crystal are several orders of magnitude shorter than the dimensions of the crystal.*

2. Discussion. To clarify the nature of such strong phonon scattering in the volume of a pure fullerene crystal, we must compare our observations with the results of previous measurements. One of the most important results obtained in Ref. 4 was the discovery that below 90 K the thermal conductivity of a sample depends on the rate of cooling or on the observation (annealing) time at constant temperature. Under prolonged annealing at constant temperature in the range 85–90 K the value of k increased by several percent. The characteristic relaxation time of the annealing processes increased from ~ 1.7 h at 87.5 K up to ~ 4.5 h at 85 K. These observations could be explained by assuming the existence of orientational defects in the sc-phase crystal; the equilibrium density of such defects $N_{d0} = 1/\{1 + \exp(U_2/T)\}$ drops exponentially at $T \ll T_m$. According to the estimates made in Ref. 4, the energy of formation of an orientational defect $U_2 \sim 130$ K is much lower than the height of the potential barrier $U_1 \sim 3000$ K separating differently oriented molecules at neighboring sites of the crystal lattice in the sc phase. The time over which the equilibrium density N_{d0} of defects is reached is determined by the hopping time of molecules from one orientational state into another $\tau_{tr} \sim j^{-1} \exp(U_1/T)$, where $j \sim 10^{13}$ Hz is the characteristic vibrational frequency of the molecules in the lattice. Since the quantity τ_{tr} increases rapidly with decreasing temperature and reaches $\tau_{tr} \sim 1.6 \cdot 10^4$ s at 85 K, for any reasonable rate of cooling ~ 0.1–0.001 K/s below 85 K a

quite large number of orientational defects "freezes" in the crystal; this corresponds to a transition of the crystal into an "orientational glass" state.

The effective phonon mean free path in our sample below 15 K is $\lambda_p \sim 50d$. Following the results of Ref. 4, we shall assume that the maximum phonon ranges are limited by scattering on "frozen" orientational defects, i.e.,

$$\lambda_p = \lambda_{pd} = d^3/\sigma N_d(0), \tag{2}$$

where σ is the cross section for the scattering of thermal phonons by orientational defects and $N_d(0)$ is the density of such defects. To a first approximation it can be assumed that the cross section for phonon scattering by orientational defects $\sigma \sim d^2$ and is virtually temperature-independent. Hence it is easy to estimate that the relative density of frozen defects in a sample grown from pure C_{60} reaches $N_d(0) \sim 0.02$.

At temperatures below the maximum of the thermal conductivity $T > 15$ K, together with scattering by defects, the phonon–phonon scattering becomes important, so that the effective phonon mean free path is determined by the expression $\lambda_p^{-1} = \lambda_{pp}^{-1} + \lambda_{pd}^{-1}$. Accordingly, the thermal conductivity of the crystal can be written as

$$k(T) = \frac{1}{3} C(T) v \lambda_p(T) \sim C(T)/\{\sigma N_d/d^3 + \lambda_{pp}^{-1}\}. \tag{3}$$

Here $N_d(T,t)$ is the relative density of orientational defects, which in the general case depends on the cooling rate and the annealing time t at constant temperature. As one can see from Eq. (3), in discussing the contribution of different scattering mechanisms it is more convenient to switch to the thermal resistance k^{-1}:

$$k^{-1} = k_{pd}^{-1} + k_{pp}^{-1} = 3\{\sigma N_d/d^3 + \lambda_{pp}^{-1}\}/\{C(T) v\}. \tag{3a}$$

The temperature dependence of the thermal resistance is shown in Fig. 2. The notation is the same as in Fig. 1. The curve *3* describes the contribution of the thermal resistance due to phonon scattering by defects at temperature $T < 30$ K. The solid curve *2* corresponds to the temperature dependence $k_{pp}^{-1}(T) \sim \exp(-80/2.5T)$. The dashed line shows the continuation of this curve beyond the computational interval 25–75 K. The straight line *4* describes the behavior of the thermal resistance of the crystal as obtained in Ref. 4, which we calculated according to formula (3a) assuming that the specific heat of fullerite above 30 K is temperature-independent, the density of frozen orientational defects $N_d = N_d(0)$, and the effective phonon mean free path with phonon–phonon scattering is $\lambda_{pp} \sim T^{-1}$. The latter condition, strictly speaking, holds only for $T > \Theta$, according to Refs. 8 and 9. In this approximation $k^{-1} = k_{pd}^{-1} + k_{pp}^{-1} = \{N_d(0) + BT\}/A$, where A and B are numerical constants. The value of k_{pd}^{-1} in the sample can be estimated from the intersection of the straight line *4* and the ordinate.[4] Using the known experimental values of the specific heat at $T = 30$ K and the average velocity of sound and assuming that the cross section for scattering of phonons by frozen orientational defects at $T = 30$ K equals $\sigma = d^2$, we find that the density of frozen defects in a crystal containing 0.5% impurities, according to our estmates, is $N_d(0) \sim 0.07$, which is more than three times greater than the density of defects in our sample (it is important that here both estimates of $N_d(0)$ were obtained from the experimental data by the same method).
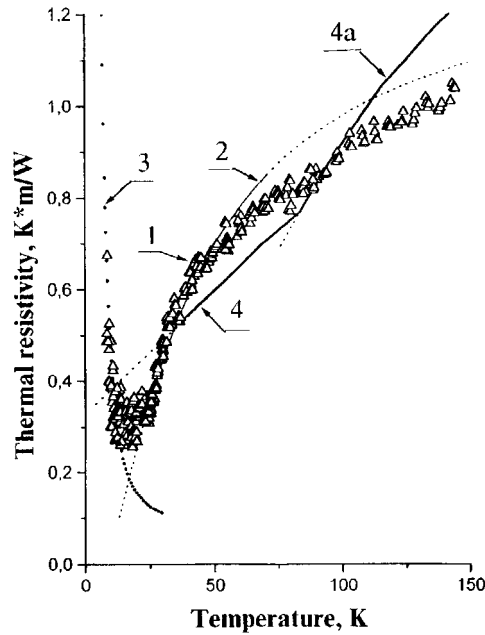
FIG. 2. Thermal resistance k^{-1} versus temperature. The designations are the same as in Fig. 1. The curve *4*a was taken from Ref. 4 and corresponds to the contribution of phonon scattering by equilibrium defects.

The density N_d of the orientational defects in the volume of the crystal approaches the equilibrium value $N_{d0}(T)$ at $T > 88$ K. The dotted curve *4*a in Fig. 2 corresponds to the computed curve[4] $k^{-1} \sim N_{d0}(T)$ at high temperatures. As one can see from Fig. 2, if in the entire temperature range the density of the orientational defects in our sample is three times lower than in Ref. 4, the thermal resistance of the purer sample at temperatures $T > 30$ K is determined mainly by phonon–phonon scattering $k_{pp}^{-1} \geqslant 3k_{pd}^{-1}$. Moreover, the temperature dependence $k^{-1}(T)$ in the interval $T = 25-75$ K is closer to exponential (curve *2*) than to linear. At temperatures at the order of or higher than the Debye temperature, $T > 80$ K, the exponential dependence should, of course, approach the power law $k_{pp}^{-1} \sim T^n$, where $n = 1-2$ (Refs. 8 and 9).

Thus the observed temperature dependence $k(T)$ in a bulk crystal consisting of pure C_{60} can be qualitatively described on the basis of the Debye–Peierls phonon model.[8,9] However, a careful analysis of the experimental temperature dependence of the thermal conductivity of our sample (points in Figs. 1 and 2) shows that as the temperature increases, a slight kink is observed in the curve $k(T)$ in the region $T \sim 90-100$ K. This is not surprising, since at these temperatures the temperature dependence $k_{pd}(T)$ should change as a result of "thawing" of the orientational defects and the corresponding change in the temperature dependence $N_d(T)$. In the approximations adopted above, the contribution of the phonon scattering by orientational defects does not exceed 30% in this temperature range, but this is enough to change the slope of the curve $k^{-1}(T)$ in the purer sample.

Unfortunately, accurate quantitative calculations of the expected temperature dependence $\lambda_{pp}(T)$ and, correspondingly, $k_{pp}(T)$ are impossible at present, since the form of the dispersion curves $\omega(K)$ for phonons of different modes in fullerite is unknown. To compare the theoretical predictions with the measurements of the thermal conductivity and specific heat of pure crystals, it is also necessary to determine the ratio of the contribution of the Debye component to the specific heat of fullerite (corresponding to traveling phonons) and, for example, the Einstein component (incoherent vibrations of the molecules) at temperatures above several kelvin[5,6] and the contribution of orientational defects to the specific heat of the crystal in the sc phase.

The effective phonon ranges in the crystal, estimated from the specific heat, are limited to values $\lambda_p \lesssim 10^{-4}$ mm. It can be conjectured on the basis of the results obtained in Ref. 4 that phonon scattering by orientational defects plays the main role here. It is also possible that defects appear as a result of the fcc–sc phase transition, which is accompanied by a $\sim 1\%$ jump in the molar volume, as the sample is mounted rigidly on the cold finger. In the latter case it is difficult to count on a further increase in the maximum thermal conductivity of the fullerite crystals without a radical change in the measurement methods.

[1] A. P. Ramirez, Condens. Matter News **3**, 6, 9 (1994).

[2] G. Pitsi, J. Caerels, and J. Thoen, Phys. Rev. B **55**, 915 (1997).

[3] J. E. Fischer, A. R. McGhie, J. K. Estrada *et al.*, Phys. Rev. B **53**, 11418 (1996).

[4] R. C. Yu, N. Tea, M. B. Salamon *et al.*, Phys. Rev. Lett. **68**, 2050 (1992).

[5] J. R. Olson, K. A. Topp, and R. O. Pohl, Science **259**, 1145 (1993).

[6] W. P. Beyermann, M. F. Hungley, J. D. Thompson *et al.*, Phys. Rev. Lett. **68**, 2046 (1992).

[7] M. Tachibana, M. Michiyama, H. Sakuma *et al.*, J. Cryst. Growth **166**, 883 (1996).

[8] J. M. Ziman, *Electrons and Phonons*, Clarendon, Oxford, 1963.

[9] R. Berman, *Thermal Conduction in Solids*, Clarendon Press, Oxford, 1976 [Russian translation, Mir, Moscow, 1979].

Translated by M. E. Alferieff

Supersymmetric spin glass

S. Gukov[a)]

L. D. Landau Institute for Theoretical Physics, 117334 Moscow, Russia; Institute of Theoretical and Experimental Physics; 117259, Moscow, Russia

The manifestly supersymmetric four-dimensional Wess–Zumino model with quenched disorder is considered at the one-loop level. The infrared fixed points of a beta function form the moduli space $\mathcal{M} = RP^2$, where two types of phases are found: with and without replica symmetry. While the former phase possesses only a trivial fixed point, this point become unstable in the latter phase, which may be interpreted as a spin glass phase. © *1997 American Institute of Physics.*
[S0021-3640(97)01808-2]

PACS numbers: 12.60.Jv, 75.10.Nr

1. INTRODUCTION

There are a great many field-theoretical models describing a system in quenched random fields or with random coupling constants (Refs. 1–3, etc.). In solid state physics such models naturally arise from the corresponding pure systems whenever impurities are introduced. It is interesting to extend randomness to other well-studied field theories, just as, for example, disorder was implemented into minimal conformal models in Ref. 3. It was shown in Ref. 4 and subsequent papers that stochastic equations, like field theories in the presence of random external sources, often prove to possess some hidden supersymmetry. Kurchan[5] endorsed this result for spin glass dynamics. Because supersymmetry can handle perturbative corrections, such random theories are especially interesting. Such an approach will be taken in this paper.

On the other hand in field theories with manifest space–time supersymmetry the superpotential is a holomorphic function not only of the fields but also of the coupling constants.[6] Therefore the couplings and fields enter the potential on an equal footing, so that it seems very natural to introduce a random (Gaussian) distribution of some couplings in the Lagrangian. But the power of supersymmetry is so strong that the superpotential gets no quantum corrections,[6,7] i.e., provided that the coupling has no dynamical D-terms, integrating over it solves the problem.

In Sec. 2 we formulate a four-dimensional supersymmetric Wess–Zumino theory in a random field. In Sec. 3 the infrared fixed points of one-loop β-functions are found in the context of the replica method. Analysis of these fixed points suggests the existence of two phases on the moduli space $\mathcal{M} = RP^2$. Numerical evaluation of the most general expressions is eventuated in the phase diagram, which is illustrated by two simple examples in Sec. 4. Section 5 is devoted to discussions and conclusions.

2. WESS–ZUMINO MODEL PERTURBED BY RANDOMNESS

It follows from the above arguments it follows that the SUSY analog of a theory with disorder must contain dynamical terms for the random field. In the present paper we consider a four-dimensional Wess–Zumino model that is the supersymmetric counterpart of the φ^4-model (the two theories are defined in the same critical dimension, and the scalar potential after integrating the auxiliary field in the former model is actually φ^4). Since, according to Ref. 7, Wess–Zumino theory is defined only as a low-energy field theory, we will study the Wilsonian effective action obtained by integrating over fast modes with momenta $\Lambda' < P < \Lambda$. We thereby define a chiral superfield $\Phi = \varphi + \theta\psi + \theta^2 F$ and a random superfield H. In this notation the original action is[b]

$$S = \int d^4x d^2\theta d^2\overline{\theta}\left(g\Phi^+\Phi - \Phi^+H - H^+\Phi + \frac{1}{u}H^+H\right) + \frac{1}{3!}\int d^4x d^2\theta(\lambda_1'\Phi H^2$$

$$+ \lambda_2'\Phi^2 H + \lambda_3'\Phi^3 + \lambda_4'H^3) + \text{h.c.} \tag{1}$$

This action admits the following treatment. It may be obtained (for a given set of parameters) from the usual Wess–Zumino action by the replacement $\Phi \rightarrow \Phi + H$, as one usually does in a summation over local extrema.[2]

One of the most powerful methods of dealing with random fields is the replica trick,[1] which we will use here to solve this ''toy'' model. It reduces to introducing n copies (replicas) of our system, integrating out the H field, and then solving n-replica problem and taking $n = 0$ at the end of the calculations. After replication the action (1) takes the form

$$S = \int d^4x d^2\theta d^2\overline{\theta}\left[\sum_{a=1}^{n}(g\Phi_a^+\Phi_a - \Phi_a^+H - H^+\Phi_a) + \frac{1}{u}H^+H\right]$$

$$+ \frac{1}{3!}\int d^4x d^2\theta\left[\sum_{a=1}^{n}(\lambda_1'\Phi_a H^2 + \lambda_2'\Phi_a^2 H + \lambda_3'\Phi_a^3) + \lambda_4'H^3\right] + \text{h.c.} \tag{2}$$

As will be shown later, the model depends only on the relative values of the lambdas, so that one can put them small enough to determine the H field from the saddle-point equation on the D-term only:

$$H = u\sum_{a=1}^{n}\Phi_a \quad \text{and} \quad H^+ = u\sum_{a=1}^{n}\Phi_a^+. \tag{3}$$

Substituting it back into (2) yields:

$$S = \sum_{a,b=1}^{n}\int d^4x d^2\theta d^2\overline{\theta}g_{ab}\Phi_a^+\Phi_b + \frac{1}{3!}\int d^4x d^2\theta\left(\sum_{a,b,c=1}^{n}\lambda_1\Phi_a\Phi_b\Phi_c\right)$$

$$+ \sum_{a,b=1}^{n}\lambda_2\Phi_a^2\Phi_b + \sum_{a=1}^{n}\lambda_3\Phi_a^3\right) + \text{h.c.} \tag{4}$$

where $g_{aa} = g + 3u$, $g_{a \neq b} = 3u$, and the three types of vertices $\lambda_1 = \lambda_1' u^2 + \lambda_4' u^3$, $\lambda_2 = \lambda_2' u$, and $\lambda_3 = \lambda_3'$ mix replica indices in different ways. It is the action (4) that we are going to study.

3. FIXED POINTS OF β FUNCTIONS

The renormalization group (RG) equations for g_{ab} easily follow from the one-loop diagram for the pure Wess–Zumino theory:[8]

$$\frac{dg_{ab}}{d \ln \Lambda} = \frac{1}{288\pi^2} \Bigg\{ 9\lambda_3^2 g_{ab}^2 + 2\lambda_2^2 \sum_{c,d=1}^{n} [(g_{ac}+g_{bc})g_{cd}+g_{ac}g_{bd}] + 3\lambda_2\lambda_3 \Bigg[\sum_{c=1}^{n} (g_{ac}^2$$

$$+ g_{bc}^2) + 2g_{ab}\sum_{c=1}^{n} (g_{ac}+g_{bc}) \Bigg] + 9\lambda_1\lambda_3 \sum_{c,d=1}^{n} (g_{ac}g_{ad}+g_{bc}g_{bd}) \Bigg\}. \qquad (5)$$

Taking into account the possible replica symmetry breaking, we take the Parisi ansatz for g_{ab}:[1] the off-diagonal part of g_{ab} is parametrized by an internal function $g(x)$ defined on a unit interval $x \in [0,1]$, and the diagonal part is $g_{aa} = \tilde{g}$. The replica-symmetric case is obtained by putting $g(x) = g = \mathrm{const}$. The algebra of Parisi matrices $\mathbf{a} = (\tilde{a}, a(x))$ is defined by the multiplication rule:[1]

$$\mathbf{c} = \mathbf{ab}: \quad \tilde{c} = \tilde{a}\tilde{b} - \int_0^1 dx\, a(x)b(x),$$

$$c(x) = b(x)\Bigg[\tilde{a} - \int_0^1 dx\, a(y) \Bigg] + a(x)\Bigg[\tilde{b} - \int_0^1 dx\, b(y) \Bigg]$$

$$- \int_0^x dy\,(a(x)-a(y))(b(x)-b(y)). \qquad (6)$$

By means of this rule we get sums over replica indices that appear in (5) in the $n \to 0$ limit:

$$\sum_{b=1}^{n} g_{ac} \to \tilde{g} - \bar{g} \qquad \sum_{c,d=1}^{n} g_{ac}g_{cd} \to (\tilde{g}-\bar{g})^2 \qquad \sum_{b=1}^{n} g_{ac}^2 \to \tilde{g}^2 - \overline{g^2} \qquad (7)$$

where

$$\bar{g} = \int_0^1 dx\, g(x) \quad \text{and} \quad \overline{g^2} = \int_0^1 dx\, g^2(x). \qquad (8)$$

As usual in spin glass theory, one deals with the problem of finding the infrared (IR) fixed points[c] of Eq. (5), which determine the dynamics of the system:

$$\frac{3}{2}\lambda_3^2 \tilde{g}^2 + (\lambda_2^2 + 3\lambda_1\lambda_3)(\tilde{g}-\bar{g})^2 + \lambda_2\lambda_3[2\tilde{g}(\tilde{g}-\bar{g}) + \tilde{g}^2 - \overline{g^2}] = 0 \qquad (9)$$

$$\frac{3}{2}\lambda_3^2 g^2(x) + (\lambda_2^2 + 3\lambda_1\lambda_3)(\tilde{g}-\bar{g})^2 + \lambda_2\lambda_3[2g(x)(\tilde{g}-\bar{g}) + \tilde{g}^2 - \overline{g^2}] = 0. \qquad (10)$$
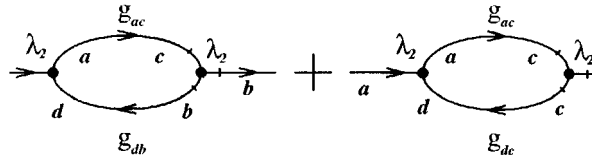
FIG. 1. Surviving (in the $n \to 0$ limit) λ_2^2-contributions.

For example, the λ_2^2 term is produced by the two nonvanishing (with number of replicas) diagrams shown in Fig. 1.

These equations have two remarkable properties: they are homogeneous in λ and g, i.e., they depend only on their squares. This type of dependence on λ tells us that the zeroes of the beta functions (9)–(10) do not depend on the values of the couplings themselves, but only on their mutual ratios, so that the moduli space of the theory is RP^2 instead of $R^3 = \{\lambda_1, \lambda_2, \lambda_3\}$. Therefore, without loss of generality, we may put the couplings very small, while keeping their ratios fixed. In this limit the results that we are going to obtain are exact. Moreover, in what follows we will assume $\lambda_3 \neq 0$, so that we can choose it to be $\lambda_3 = 1$ and denote $\lambda_2 = \lambda$ and $\lambda_1 = \mu$ (affined map).[d] The special case $\lambda_3 = 0$ will be studied in the first example of Sec. 4.

Quadratic dependence on g in (10) means that for each set of general characteristics, such as $\overline{g}$, $\overline{g}^2$ and $\widetilde{g}$, there are only two possible values $g_{1,2}$ (if any) which the function $g(x)$ can take on at a IR-fixed point. Moreover, the same must be true for $\widetilde{g}$, because formally it also satisfies a similar equation (9). We are free to chose $\widetilde{g} = g_1$, for instance. Let us denote the measure of points on a unit interval of x where $g(x) = g_1$ as $1 - x_0$ and the measure of points where $g(x) = g_2$ as x_0. For example, it may be a stepwise distribution:

$$g(x) = \begin{cases} g_1, & x_0 < x < 1, \\ g_2, & 0 < x < x_0. \end{cases} \tag{11}$$

Thus we have two equations (9), (10) in three unknowns: $g_{1,2}$ and x_0, with $\overline{g}$ and $\overline{g}^2$ depending on them. If g_1 and g_2 are not simultaneously equal to zero[e] then we actually have only two unknowns: x_0 and the ratio $p = g_2/g_1$. In this notation Eqs. (9) and (10) may be rewritten as

$$\begin{cases} 1 + \left(\frac{2}{3}\lambda^2 + 2\mu\right) x_0^2 (1-p)^2 + \frac{2}{3} x_0 \lambda [2(1-p) + (1-p^2)] = 0, \\ p^2 + \left(\frac{2}{3}\lambda^2 + 2\mu\right) x_0^2 (1-p)^2 + \frac{2}{3} x_0 \lambda [2p(1-p) + (1-p^2)] = 0, \end{cases} \tag{12}$$

which determine both p and x_0 and, consequently, the phase of the system.

Curiously enough, for a given solution p and x_0 we get a whole set of RG-fixed points $\{\widetilde{g}, g(x)\}$, differing by an arbitrary factor. Of course, this degeneracy will be lifted by higher loop corrections, so that particular value of the fixed point will be determined
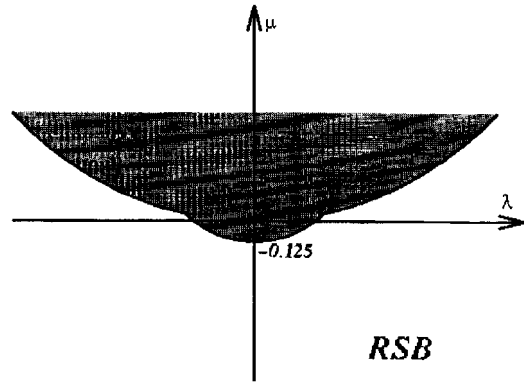
FIG. 2. The phase diagram (not drawn to scale).

by the full perturbative expansion. In the one-loop approximation, the explicit data for $(\tilde{g}, g(x))$ at a fixed point may be determined by the initial conditions g and u.

If for some set of couplings there is no solution to (12) except the trivial one $\tilde{g} = g(x) = 0$, we will refer to this point on the phase space $\{\lambda, \mu\} \in \mathcal{M} = RP^2$ as a replica-symmetric point and will denote the corresponding phase as ''RS.'' Otherwise, replica symmetry is broken with x_0 being the solution of (12), and the corresponding phase ''RSB'' looks like a spin glass system.

Since (12) must be solved by the same p, by equating the solutions to each equation we get a relation between x_0 and $\{\lambda, \mu\} \in \mathcal{M}$. Instead of writing the resulting complicated formula (partly because it can not be solved for x_0), we display it for $x_0 = 1$:

$$\frac{\lambda^2 + 3\mu + \lambda \pm \sqrt{\frac{5}{2}\lambda^2 - \frac{9}{2}\mu + \frac{3}{2}\lambda}}{\lambda^2 + 3\mu - \lambda} = \frac{\lambda^2 + 3\mu - \lambda \pm \sqrt{\frac{5}{2}\lambda^2 - \frac{9}{2}\mu - \frac{3}{2}\lambda}}{\frac{3}{2} + \lambda^2 + 3\mu - 3\lambda}, \qquad (13)$$

where the signs in the two sides are taken independently. Replacing $\lambda \to x_0 \lambda$ and $\mu \to x_0^2 \mu$, we get Eq. (13) for arbitrary x_0. This expression describes (part of) a curve in $\mathcal{M}$ that separates the RS and RSB phases as shown in Fig. 2. The shaded region indicates a replica-symmetric phase and the unshaded region corresponds to replica symmetry breaking, where there is a non-trivial solution to (13), and the trivial point $\tilde{g} = g(x) = 0$ becomes unstable, as will be discussed at length in the second example of the next Section.

4. TWO SIMPLE EXAMPLES

a) $\lambda_3 = 0$. In this case the beta functions (5) become

$$\frac{d\tilde{g}}{d \ln \Lambda} = \frac{1}{48\pi^2} \lambda_2^2 (\tilde{g} - \bar{g})^2, \quad \frac{dg(x)}{d \ln \Lambda} = \frac{1}{48\pi^2} \lambda_2^2 (\tilde{g} - \bar{g})^2.$$

These equations may be easily integrated, with the result:

$$\widetilde{g}_\Lambda = \widetilde{g}_{0,\Lambda'} + \frac{A}{48\pi^2}\lambda_2^2 \ln\frac{\Lambda}{\Lambda'}, \quad g_\Lambda(x) = g_{0,\Lambda'}(x) + \frac{A}{48\pi^2}\lambda_2^2 \ln\frac{\Lambda}{\Lambda'},$$

where the constant $A = (\widetilde{g} - \bar{g})^2$ is determined by the initial conditions and remains unchanged during renormalization group flow. Since for any λ_2 the only fixed point is $\widetilde{g} = g(x) = 0$, this phase is always replica-symmetric and is not as interesting as the others.

b) $\lambda_2 = 0 \leftrightarrow \lambda = 0$. Equations (9) and (10) take the form:

$$\begin{cases} \widetilde{g}^2 + 2\mu(\widetilde{g} - \bar{g})^2 = 0 \\ g^2(x) + 2\mu(\widetilde{g} - \bar{g})^2 = 0 \end{cases} \tag{14}$$

for which $g_{1,2} = \pm g$ for some $g \neq 0$ in the SG phase. In parametrization (11)

$$\bar{g} = (g_1 - g_2)x_0 = 2gx_0 \quad \text{and} \quad \bar{g}^2 = (g_1^2 - g_2^2)x_0 = 2g^2 x_0. \tag{15}$$

Substituting it into (14) yields a nontrivial solution:

$$-8\mu x_0^2 = 1 \quad \text{or} \quad x_0 = \frac{1}{\sqrt{-8\mu}} \tag{16}$$

which exists only for $\mu < -1/8$. It is the range of μ where the RSB phase can be found. Let us emphasize that it is precisely at these points in $\mathcal{M}$ that the trivial fixed point $\widetilde{g} = g(x) = 0$ becomes unstable, for example, against perturbations in $\widetilde{g}$. To see this, consider $\widetilde{g} = \epsilon$:

$$\frac{d\epsilon}{d\ln\Lambda} = \alpha\epsilon^2, \tag{17}$$

where $\alpha < 0$ if (16) is true (i.e., an arbitrarily small ϵ increases in value during the flow to low energies). This simple case illustrates the behavior of the general system (12). On the phase diagram it corresponds to the μ axis, where both the RS and RSB phases exist.

5. SUMMARY

Starting from the (space–time) supersymmetric Wess–Zumino model in a random and quenched background (1), we have found that the renormalization group equations (5) at a fixed point are quadratic homogenous equations in the couplings and in g. The former property allowed us to take the couplings very small and to reduce the moduli space to $\mathcal{M} = RP^2$. There are two types of points (phases) in this moduli space, those with and without broken replica symmetry.

Though we have found all IR-fixed points of the one-loop β function, the stability of the nontrivial fixed points and of the analytic RG flow to them remain unexplored. Finally, it is interesting to generalize this analysis to more complex supersymmetric theories and to find realistic models whose critical behavior correspond to such theories.

A. Morozov and I. Polyubin for their stimulating suggestions and comments. Also I am grateful to V. Dotsenko, from whom I first learned what a spin glass is and with whom many of the ideas presented here have been discussed.

[a] e-mail: gukov@landau.ac.ru
[b] For the sake of simplicity the mass terms are omitted.
[c] The points where the β functions vanish.
[d] If $\lambda_3 \neq 1$ then the correct parameters are $\lambda = \lambda_2 / \lambda_3$ and $\mu = \lambda_1 / \lambda_3$.
[e] Otherwise we get a trivial replica-symmetric fixed point.

[1] M. Mezard, G. Parisi and M. A. Virasoro, *Spin Glass Theory and Beyond*, World Scientific (Singapore 1987).
[2] V. S. Dotsenko, *Introduction to the Theory of Spin-Glasses and Neural Networks*, World Scientific (Singapore 1994).
[3] Vl. Dotsenko, M. Picco and P. Pujol, ''Two critical models with disorder,'' PAR-LPTHE-95-63, hep-th/9512087.
[4] G. Parisi and N. Sourlas, ''Random magnetic fields, supersymmetry, and negative dimensions,'' Phys. Rev. Lett. **43** (1979), 744.
[5] J. Kurchan, *Supersymmetry in Spin Glass Dynamics*, 1993.
[6] N. Seiberg, ''The power of holomorphy: exact results in 4D SUSY field theories,'' PASCOS 1994, 357–369, hep-th/9408013.
[7] K. Intriligator and N. Seiberg, ''Lectures on supersymmetric gauge theories and electric-magnetic duality,'' Nucl. Phys. Proc. Suppl. **45BC**: 1–28 (1996), hep-th/9509066.
[8] J. Wess and B. Zumino, ''A Lagrangian model invariant under supergauge transformations,'' Phys. Lett. **49B** (1974), 52.

Published in English in the original Russian journal. Edited by Steve Torstveit.